UNIVERSITY OF CAPE TOWN

A new compact neutron spectrometer

Angus COMRIE

A thesis submitted in fulfillment of the requirements

for the degree of Doctor of Philosophy

in the

Department of Physics

November 22, 2016

UNIVERSITY OF CAPE TOWN

Abstract

Science Faculty

Department of Physics

Doctor of Philosophy

A new compact neutron spectrometer

by Angus COMRIE

A new compact neutron spectrometer has been designed, developed and characterized. The detector is based on EJ299-33 plastic scintillator coupled to silicon photomultipliers, and a digital implementation of pulse shape discrimination is used to separate events associated with neutrons from those associated with gamma-rays. The spectrometer is suitable over the neutron energy range 1 – 100 MeV, and the development illustrated with measurements made using an Am-Be radioisotopic source, a D-T sealed tube neutron generator and quasi-monoenergetic neutron beams produced using the iThemba LABS cyclotron. A segmented variation of the spectrometer is capable of providing directional information through the comparison of count rates between scintillator cells.

Acknowledgements

First and foremost, I would like to thank my supervisor, Andy Buffler, for his patience, guidance and direction throughout my degree. I could not have asked for a more supportive and understanding supervisor.

I am grateful for the assistance and guidance of my co-supervisor, Ricky Smit, as well as my colleague, Dieter Geduld, particularly during data collection at iThemba LABS.

A number of collaborators and institutes have provided financial backing, without which none of this would have been possible. Particular thanks go to Heinrich Wörtche and the INCAS^3 institute, the National Research Foundation (NRF), as well as the Technology and Innovation Agency (TIA).

Special thanks go to the staff of UCT physics workshop, for their tireless assistance in practical construction matters, and to the staff at iThemba LABS for assistance during data collection.

Thank you to all those who supported me during the many ups and downs of my degree, most notably my parents, Craig and Brigid; my sisters Caitlin and Laura; and last but not least, my close friends and long-suffering officemates.

Contents

List of Figures

List of Tables

List of Abbreviations

PSD	**P**ulse **S**hape **D**iscrimination
PMT	**P**hoto**M**ultiplier **T**ube
SiPM	**Si**licon **P**hoto**M**ultiplier
MPCC	**M**ulti-**P**hoton **P**ixel **C**ounter
gAPD	**G**eiger-mode **A**valanche **P**hoto-**D**iode
ADC	**A**nalogue to **D**igital **C**onverter
MCX	**M**icro **C**oa**x**ial
FPGA	**F**ield-**P**rogrammable **G**ate **A**rray
DSP	**D**igital **S**ignal **P**rocessor
DAQ	**D**ata **A**c**Q**uisition
FoM	**F**igure **o**f **M**erit
FWHM	**F**ull **W**idth **H**alf **M**aximum
PPO	2,5-diphenyloxazole
PVT	**P**oly**V**inyl**T**oluene
MSPS	**M**ega **S**amples **P**er **S**econd
GSPS	**G**iga **S**amples **P**er **S**econd
PGA	**P**ulse **G**radient **A**nalysis
PDE	**P**hoton **D**etection **E**fficiency
DCC	**D**igital **C**harge **C**omparison
GA	**G**enetic **A**lgorithm
CFD	**C**onstant **F**raction **D**iscriminator
D-T	**D**euterium-**T**ritium
Am-Be	**A**mericium-**B**eryllium
ToF	**T**ime **o**f **F**light

Chapter 1

Introduction

Interest in the development of compact neutron spectrometers has grown in recent years, mainly for deployment in aircraft [1], for minerals exploration [2], personal and workplace dosimetry [3] and in security, particularly the detection of special nuclear materials [4], [5].

Collisions between galactic cosmic rays and air molecules in the Earth's atmosphere lead the production of secondary radiation cascades. Figure 1.1 shows the relative dose equivalent fraction for a number of particle species. While only a small fraction of the relative dose is due to neutrons at ground level, at altitudes of about 10 km, 40% of the relative dose is due to secondary neutrons [6]. This fraction increases to almost 50% at altitudes above 25 km. At these altitudes, the neutron fluence rate and effective dose rate are between two and three orders of magnitude higher than those measured at ground level [7]. Neutron fluence rates vary significantly with altitude and solar activity as well as latitude [8], as the Earth's geomagnetic field deflects some fraction of charged particles into space. As such, careful monitoring of neutron fluence rates across a number of commonly used flight paths is required in order to determine dose rates on commercial airliners.

Figure 1.2 shows neutron energy spectra, measured at various altitudes between sea level and 20 km (atmospheric depths of 1030 g cm^{-2} and 56 g cm^{-2} respectively). The spectra displays peaks at energies of approximately 10 MeV and 100 MeV. While existing measurements of this spectrum have been taken both on the ground [9] and across a wide number of flight paths [1], [7], further investigations are required at higher altitudes. Existing detectors often make use of liquid organic scintillators and bulky, fragile vacuum photomultiplier tubes, severely limiting their application, due

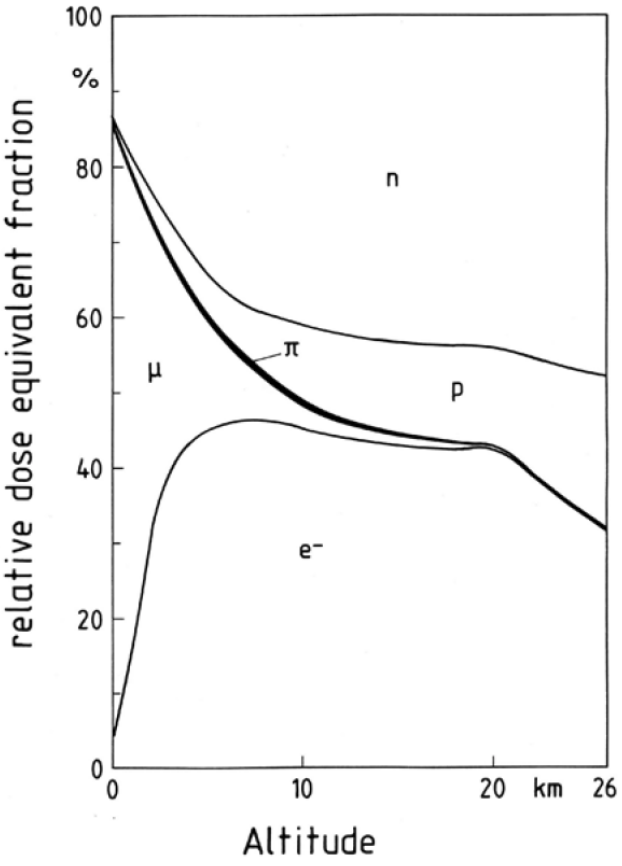

FIGURE 1.1: Relative dose equivalent fraction as a function of flight altitude for muons, electrons, protons, pions and neutrons. Reproduced from [6].

to volume constraints or operating conditions. There is therefore a need for further development of compact and rugged neutron spectrometers, capable of measuring energies up to approximately 100 MeV.

Since neutrons are seldom present without gamma-rays, any useful detector is required to be able to discriminate between the two radiation types. The light output of certain organic scintillators display both fast and slow decay components, related to the specific energy loss of the recoiling charged particle by the Birks relation [10]. Pulse shape discrimination (PSD), established in the 1950s [11] and developed through the 1960s [12], allows the identification of different types of charged particles in these scintillator detectors by means of the characteristics of the scintillation decay. Liquid organic scintillators such as the nearly-equivalent NE213, BC501A and EJ301 persist as popular detector-types for this application.

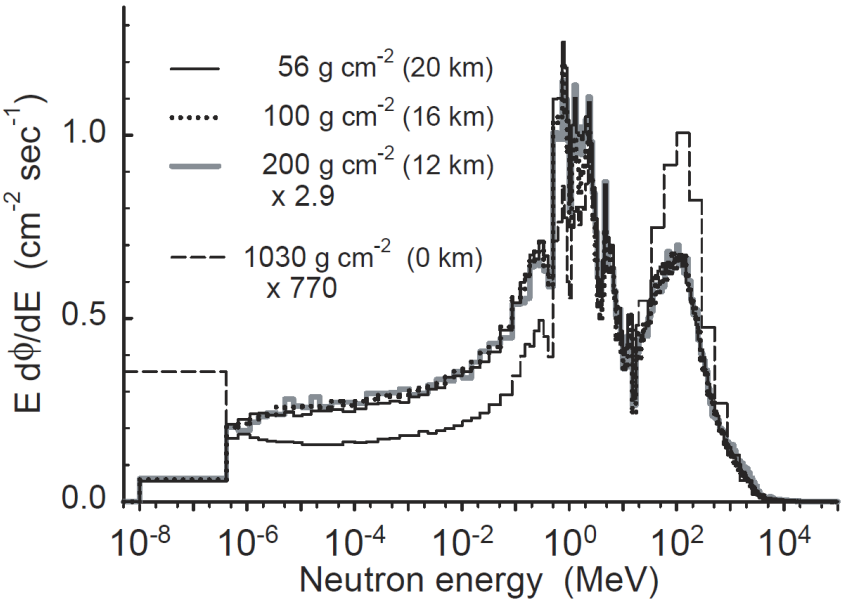

FIGURE 1.2: Neutron energy spectra, measured at various altitudes. Reproduced from [7].

A number of recent technological developments have aided the deployment of organic scintillators with PSD in non-laboratory environment.

The development of plastic scintillators that exhibit pulse shape discrimination capability [13], such as the commercially available EJ299-33 scintillator [14], removes the toxic and fire hazards associated with conventional liquid scintillators such as EJ301. Plastic scintillators posses additional practical benefits: they do not require an optical window when coupled to a photo-detector, and can easily be machined into a variety of geometric shapes, a critical factor for certain applications requiring a segmented detector.

The development of alternatives to the conventional vacuum photomultiplier tube (PMT), specifically the silicon photomultiplier (SiPM) (referred to as a multi-pixel photon counter (MPCC) or Geiger-mode avalanche photo-diode (gAPD) by some manufacturers) allow for the construction of low-cost, compact and rugged devices that are deploy-able in a range of environments.

The emergence of digital data acquisitions systems based on high speed analogue-to-digital converters (ADCs) allows for the implementation and dynamic optimisation of a number of PSD algorithms in software form, or on dedicated electronics, in the form of field-programmable gate arrays (FPGAs) or digital signal processors (DSPs).

The aim of this work is the realization of a proof-of-principle compact neutron spectrometer, constructed using PSD-capable plastic scintillator coupled to silicon photomultipliers, capable of determining incident neutron energies across a wide energy range, while providing information on the direction of incoming neutrons, through comparative measurements of segmented scintillators.

To this end, the development of a digital data acquisition system, implementing a number of commonly used pulse processing techniques, is described, and its performance characterised using neutrons of energies up to 100 MeV. As neutron interactions with carbon nuclei in organic scintillator provide a significant portion of the overall response of the detector to neutrons above 20 MeV [15], a secondary aim of this work was to carefully characterise the response of detectors based on the relatively new EJ299-33 plastic scintillator across a wide energy range. Neutron beams provided by the iThemba LABS cyclotron were used to characterise an EJ299-33 detector and a response matrix was used to demonstrate its spectroscopic capability through energy spectrum unfolding.

The remainder of the thesis is structured as follows: Chapter 2 gives a background to the concepts discussed in the following chapters, including the detection and discrimination of neutrons using organic scintillator detectors, operating principles of silicon photomultipliers and digital pulse processing technique; Chapter 3 describes the design and implementation of the digital data acquisition system; Chapter 4 describes the characterization of an EJ299-33 plastic scintillator detector and Chapter 5 discusses the development of a compact neutron spectrometer using EJ299-33 scintillator and SiPMs.

The following peer-reviewed papers were published as a result of the research described in Chapters 3, 4 & 5:

- A.C. Comrie, A. Buffler, F.D. Smit, H.J. Wörtche "Digital neutron/gamma discrimination with an organic scintillator at energies between 1 MeV and 100 MeV", *Nuclear Instruments and Methods in Physics Research Section A* [16]
- A.C. Comrie, A. Buffler, F.D. Smit, H.J. Wörtche "Tests of pulse shape discrimination with EJ299-33 plastic scintillator for use in portable spectroscopy", *Technology and Instrumentation in Particle Physics (PoS)* [17]
- A. Buffler, A.C. Comrie, F.D. Smit, H.J. Wörtche "Neutron Spectrometry with EJ299-33 Plastic Scintillator for E_n = 1 to 100 MeV", *IEEE Transactions on Nuclear Science* [18]
- A. Buffler, A.C. Comrie, F.D. Smit, H.J. Wörtche "A new compact neutron/gamma-ray scintillation detector", *International Journal of Modern Physics: Conference Series* [19]

The following open-source code repositories contain projects developed solely by the author of this thesis, facilitating research described in Chapters 3, 4 & 5:

- Digital data acquisition (DAQ) software package, written in C++, utilising the Qt5 framework: `https://bitbucket.org/veggiesaurus/qtdaq`
- Monte-Carlo sim of four scintillators coupled to SiPMs: `https://bitbucket.org/veggiesaurus/optsimquadscint`

Chapter 2

Background

2.1 Organic scintillators

The indirect detection of particles through scintillation is a widely used method in spectroscopy. In order for a material to behave as an efficient scintillator, a number of requirements must be met. Firstly, emission and absorption spectra should have minimal overlap. This allows emitted light to travel through the material and be collected by a photon sensor, such as a photomultiplier tube. Secondly, it should efficiently convert the kinetic energy of incident particles into photons, either directly (in the case of charged particle detection), or indirectly (via Compton scattering of gamma-rays or scattering of neutrons). Finally, the measured light response should be proportional to the energy deposited by the particle [20].

Inorganic scintillators are commonly used for gamma-ray spectroscopy, due to their high-Z composition. Organic scintillators are favoured in fast neutron detection, due to their fast response times, hydrogenous makeup and pulse shape discrimination capabilities [21]. Organic scintillators typically fall into three categories: single crystals (such as anthracene or stilbene), liquids, and plastics. Scintillators can exist as a unitary system (single crystals), binary systems or ternary systems. Binary systems consist of an efficient scintillator solute dissolved in a solvent such as toluene, xylene or polystyrene, while ternary systems contain an additional secondary solute, often responsible for shifting the emission spectrum to match a specific application [12].

2.1.1 Mechanism

Many organic scintillators consist of aromatic compounds, possessing a π-electron structure. Figure 2.1 shows typical electron levels of a scintillating organic molecule. Electrons can occupy a number of singlet energy states (S_0, S_1, etc.) or triplet states (T_1, T_2, etc.). In addition, each of these states consist of a vibrational band of sub-states (S_{00}, S_{01}, etc.). Transitions between singlet and triplet states are forbidden by multiplicity selection rules, resulting in a phosphorescent emission of higher-wavelength photons with timescales of the order of milliseconds [20]. Excitation to higher electronic and vibrational states occurs through the transfer of energy from charged particles, but most excitations decay swiftly to the S_{10} state through non-radiative means. Electrons in the S_{10} state decay through photon emission to one of the vibrational sub-states of the electronic ground state, resulting in a shift between absorption and emission spectra [12]. Interactions between triplet excitons can result in triplet-triplet annihilation:

$$T_1 + T_1 \rightarrow S_1 + S_0 + \text{phonons} \tag{2.1}$$

Triplet annihilation will therefore give rise to a delayed or "slow" scintillation component with the same emission spectrum as that of the prompt scintillation.

2.1.2 Gamma-ray interactions

Gamma-rays interact with organic scintillator materials primarily through Compton scattering off electrons, with the cross-section for interaction proportional to atomic number Z. While the photo-electric effect and pair production (for gamma-rays above 1.022 MeV) also play a minor role, the cross-sections for these interactions are $\sim Z^5$ and $\sim Z^2$ respectively, and high-Z materials are strongly preferred for gamma-ray spectroscopy. Kinematic constraints require that Compton-scattered electrons carry off a maximum energy of $E_{\max}$, defined as

$$E_{\max} = h\nu \left(\frac{2\gamma}{1+2\gamma} \right), \tag{2.2}$$

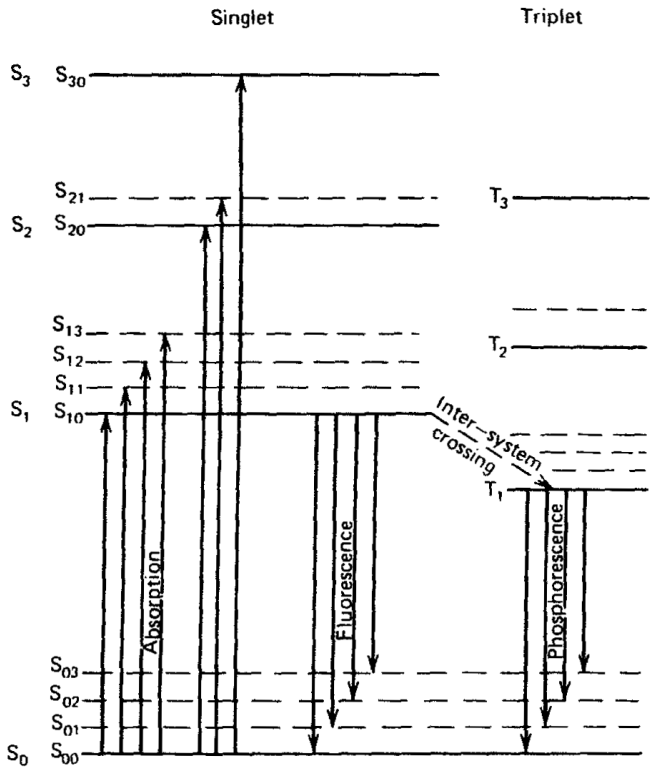

FIGURE 2.1: Energy levels in an efficient organic scintillator. Reproduced from [22].

where ν is the incident photon wavelength, and $\gamma = \frac{h\nu}{m_e c^2}$ [23]. This can be written in terms of the incident photon energy E as

$$E_{\max} = E\left(1 - \frac{1}{1 + \frac{2E}{m_e c^2}}\right). \tag{2.3}$$

This energy, known as the Compton energy, corresponds to a full back-scatter of the incident gamma-ray. Gamma-rays scattered at smaller angles will transfer less energy to the electron. As such, gamma-ray interactions in organic scintillators produce a distribution of deposited energies, rather than a photo-peak corresponding to the full energy of the incident gamma-rays.

2.1.3 Neutron interactions

Below energies of 20 MeV, neutrons interact with organic scintillators primarily via elastic scattering off nuclei, most notably hydrogen and carbon. The energy of the

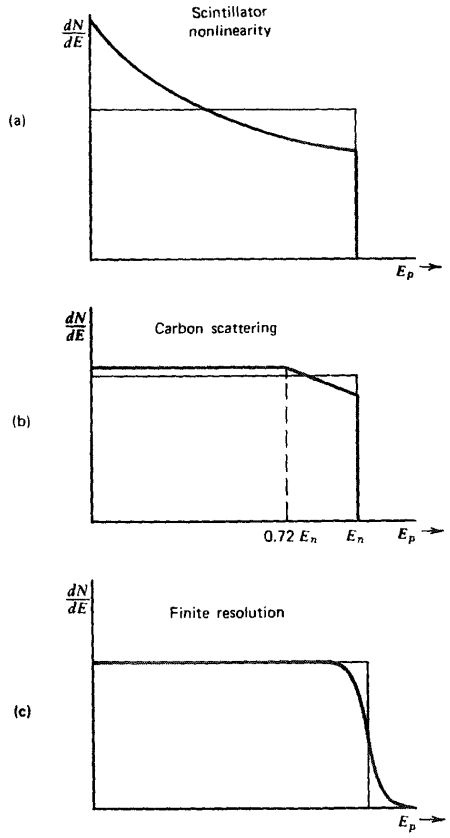

FIGURE 2.2: Effects causing distortions of proton recoil energy spectrum. Reproduced from [20].

recoiling nucleus E_R is given by

$$E_R = E_N \frac{4A}{(1+A)^2} \cos^2 \theta, \tag{2.4}$$

where E_N is the energy of the incident neutron, A is the mass number, and θ is the scattering angle. While neutrons scattering off ^{12}C can transfer at most 28% of their energy in a single collision [20], scatters off ^{1}H can transfer all of their kinetic energy, as their masses are nearly identical. The proton recoil energy distribution is a step function, dropping to zero at E_N. However, a number of factors distort measured light output distributions. Typically, scintillators have a non-linear light output response to protons at lower energies, leading to a raised tail in the spectrum, as shown in Figure 2.2 (a). Neutrons can also scatter off ^{12}C nuclei before scattering off protons, resulting in the increase in response at 72% of the incident neutron energy shown in Figure 2.2(b). Finally, the finite light output resolution of the scintillator gives rise to a smearing of

the edge, as can be seen in Figure 2.2(c).

Above about 10 MeV, inelastic neutron interactions play an important role, leading to a more complex response function. In general, the light output response $R(L)$ of a detector to neutrons with an energy distribution $P(E)$ is given by

$$R(L) = \int P(E)M(E,L)dE, \tag{2.5}$$

where $M(E,L)$ is a response matrix function, unique to each detector, that determines the light output response of the detector to a specific energy E. As many applications involve neutrons with a complex energy distribution, the determination of incident neutron energies requires the unfolding of Equation 2.5 after calibrated measurements to carefully determine $M(E,L)$. A number of unfolding approaches are detailed by Matzke [24].

2.1.4 Pulse shape discrimination

As described in Section 2.1.1, scintillation produced by organic scintillators consists of both a fast component, as well as a slow component, due to triplet-triplet annihilation. As triplet-triplet interactions require close proximity of triplets to one another, the relative intensity of the slow scintillation component will depend on the density of triplets produced [12]. The densities of excitations produced by a charged particle depends strongly on the specific energy loss dE/dx. As such, the light output response to different particles of the same energy can differ significantly. The densities of excitations produced through triplet-triplet interactions are less sensitive to specific energy loss, and thus the relative intensities of the slow and fast scintillation components will depend on the particle species [12]. This important property, found in certain organic scintillators, allows for pulse shape discrimination (PSD) to isolate events arising from a particle species of interest.

By comparing the relative intensities of these scintillation components on an event-by-event basis, events originating from gamma-rays can be excluded. A number of analogue techniques exist [25], [26] to define a pulse shape parameter S that quantitatively describes an aspect of the pulse shape. Statistical fluctuations in pulse shape lead

to Gaussian distributions of S for a particular particle species. In the common case of events arising from neutron and gamma-ray interaction, the distribution of S will take the form of a double Gaussian. In order to quantify the efficacy of PSD, a figure of merit (FoM) can be defined in terms of the mean μ and full width at half maximum (FWHM) of the two distributions:

$$\text{FoM} = \frac{|\mu_\gamma - \mu_n|}{FWHM_\gamma + FWHM_n}, \tag{2.6}$$

where μ_γ, $FWHM_\gamma$, μ_n and $FWHM_n$ are the means and FWHMs of events arising from gamma-ray and neutron interactions respectively. A larger FoM indicates a clearer separation between the distributions of S, and thus more effective discrimination between pulse classes, resulting in fewer misclassifications of pulses.

2.1.5 EJ299-33 plastic scintillator

Typical PSD requires the presence of two-decay component fluorescence, consisting of prompt florescence, as well as a delayed component. As described in Section 2.1.1, the delayed component is the result of triplet-triplet annihilation, resulting in a singlet excited state, which then decays to produce a delayed fluorescence with the same spectral distribution as prompt fluorescence [12]. The presence of delayed fluorescence requires high mobility of triplets within the medium.

The high mobility of triplets in certain organic crystals, such as stilbene [27], as well as liquid scintillators [28], such as EJ301, makes them ideal scintillators for PSD. Conversely, the limited mobility of triplets in most plastic scintillators significantly reduces the probability of triplet-triplet annihilation and the subsequent delayed fluorescence, resulting in poor PSD [29].

A strategy to overcome the limited mobility of triplets in plastic scintillators is to increase the primary scinitllation solute concentration, increasing the density of triplet states and thereby increasing the probability of triplet-triplet annihilation. This strategy was employed by Brooks et al. in the 1960s [25], in their creation of "Plastic 77", which contained 35 g/litre of p-terphenyl. Plastic 77, briefly commercialised as NE150 [22], displayed comparable PSD to that of liquid scintillators, but had significant practical

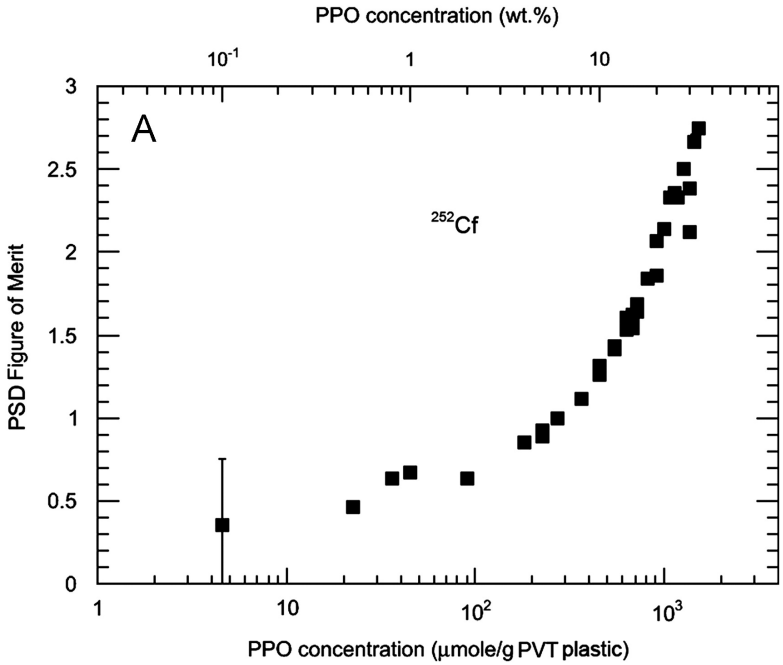

FIGURE 2.3: Figure of merit versus PPO concentration in samples of PVT-based plastic scintillator. Reproduced from [13].

drawbacks, due to whitening and edge deforming of the scintillator over time. Decades later, Zaitseva et al. [30] demonstrated that increasing the concentration of fluorescent dye in organic crystal scintillators can create a network for energy migration and triplet annihilation, resulting in the creation of mixed organic crystal scinitllators with PSD capability.

A similar process is described by Zaitseva et al. [13], in which the scintillating dye 2,5-diphenyloxazole (PPO) was disolved in polyvinytoluene (PVT) at a concentration of up to 30 wt%, producing samples of plastic scintillator that showed efficient PSD down to low light output. Figure 2.3 shows PSD figure of merit for the light output range $L = 480 \pm 75$ keV$_{\text{ee}}$ using a ^{252}Cf neutron/gamma-ray source. The figure shows that increasing the PPO concentration towards its solubility limit ($\sim 30\%$ wt) improves PSD capability by over 200% when compared to PPO concentrations typically found in liquid scintillators. The concentration of PPO required to produce effective PSD in the plastic samples is approximately three orders of magnitude higher than the required concentration for xylene-based liquid scintillators, due to the limited mobility of triplets in the plastic scintillator. The work also found that adding 0.2% wt of a secondary waveshifting dye (9,10-diphenylanthracene or DPA) improved light output

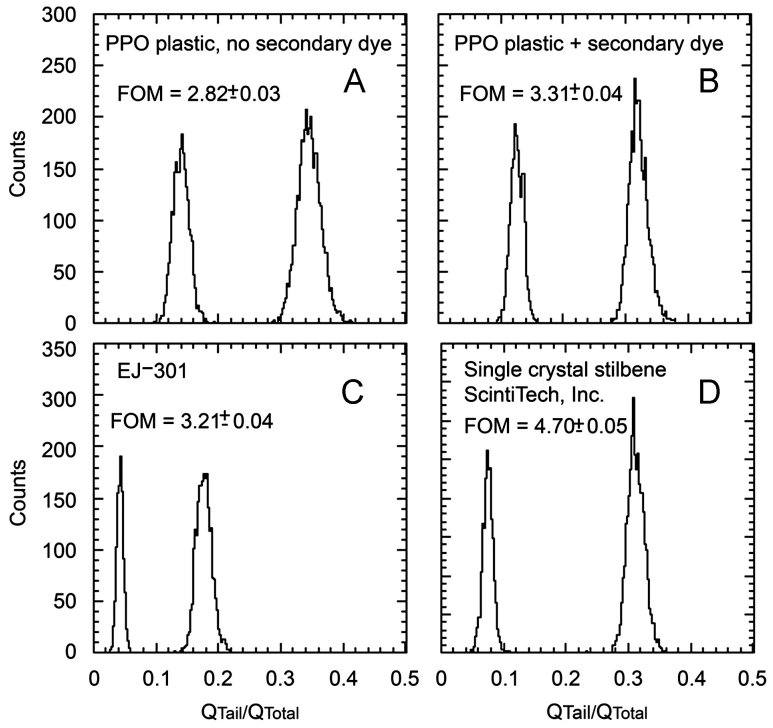

FIGURE 2.4: Counts versus pulse shape parameter for (a) PVT-based plastic with 30% wt PPO, (b) PVT-based plastic with 30% wt PPO and 0.2% wt DPA, (c) commercial EJ-301 liquid scintillator, and (d) stilbene single crystal scintillator. Reproduced from [13].

by over 50%. As shown in Figure 2.4, PVT-based scintillators loaded with 30% wt PPO and 0.2% wt DPA were found to produce improved PSD performance when compared to the comercial liquid scintillator EJ301 [13]. This plastic scintillator composition forms the basis for the commercial EJ299-33 scintillator utilised in this work. Similar experiments have been caried out with a polystyrene base [31].

Despite the high quality PSD described by Zaitseva et al. [13], attempts to reproduce the results using the same composition [33], as well as a number of tests of the commercial EJ299-33 scintillator [34], [35] have consistently shown PSD performance of the scintillator to be significantly poorer than that of standard liquid scintillator. Iwanowska-Hanke et al. [36] found that FoM decreased more significantly with increasing scintillator size in EJ299-33 than in standard liquid scintillators, possibly due to inhomogeneity of the plastic scintillator, or increased light attenuation. A revision of EJ299-33, (EJ299-33A) is available from Eljen [37], and improves chemical consistency in larger scintilaltors. However, tests of the revised scintillator [38] do not seem to show significant improvements to PSD performance.

TABLE 2.1: Fit parameters for fit of light output to energy in in the quadratic form of Equation 2.7 for various particle species. Adapted from [32].

Particle	c_0	c_1	$c_2 \times 10^3$
p	-0.15 ± 0.1	0.25 ± 0.03	9.6 ± 1
d	-0.27 ± 0.2	0.26 ± 0.02	3.9 ± 0.5
t	0.09 ± 0.3	0.21 ± 0.03	2.2 ± 0.5
^{4}He	-0.14 ± 0.1	0.11 ± 0.01	2.2 ± 0.1
^{6}Li	0.15 ± 0.5	0.023 ± 0.02	1.4 ± 0.1
^{7}Li	-0.38 ± 0.4	0.045 ± 0.01	0.9 ± 0.05
^{7}Be	-0.08 ± 0.2	0.041 ± 0.01	0.5 ± 0.04
^{9}Be	0.17 ± 0.2	0.036 ± 0.01	0.37 ± 0.05
^{10}B	-0.13 ± 0.1	0.028 ± 0.004	0.12 ± 0.02
^{11}B	-0.02 ± 0.1	0.014 ± 0.003	0.12 ± 0.05
^{12}C	-0.08 ± 0.5	0.010 ± 0.01	0.06 ± 0.04

The response of EJ299-33 to various element isotopes, ranging from protons to ^{12}C ions, is detailed by Nyibule et al. [32]. Figure 2.5 shows light output L versus incident energy E for various isotopes, along with a quadratic fit of the form

$$L(E) = c_0 + c_1 E + c_2 E^2. \tag{2.7}$$

Table 2.1 shows the fit parameters obtained by Nyibule et al. [32] for the various isotopes. A number of other works [39]–[41] have also measured light output for protons, either directly or through elastic neutron scattering, fitting the data to exponential functions. Figure 2.6 compares light output versus deposited energy for protons, extrapolated from fits given in Refs [39]–[41].

Light output resolution is particularly critical for spectroscopic measurements using neutron spectrum unfolding. EJ299-33 has been observed to have poorer light output resolution to that of conventional liquid scintillators for both gamma-ray [42] and neutron pulses [39]. Figure 2.7 shows resolution $\frac{\Delta L}{L}$ as a function of light output L for measurements with 7.6 cm × 7.6 cm cylindrical EJ299-33 and EJ309 scintillators, along with a fit of the form:

$$\frac{\Delta L}{L} = \sqrt{\alpha^2 + \frac{\beta^2}{L} + \left(\frac{\gamma}{L}\right)^2}, \tag{2.8}$$

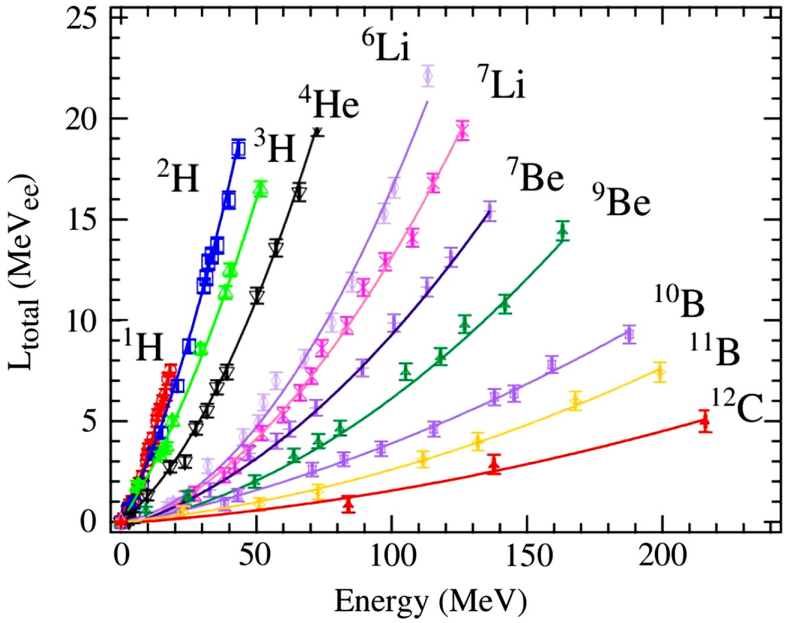

FIGURE 2.5: Light output L_{total} versus energy E for isotopes listed in Table 2.1. Reproduced from [32].

where α, β and γ are fit parameters. EJ299-33 was found to have significantly poorer light output resolution across the light output range tested.

Several works [34], [36], [42], [43] have detailed the pulse shapes produced by neutrons and gamma-rays in EJ-299-33. Figure 2.8 shows average pulse shapes produced by neutrons and gamma-rays in EJ301 and EJ299-33 scintillators [42]. A much smaller difference between neutron and gamma-ray events is observed for EJ299, giving rise to the poorer PSD performance. A number of works have modeled the pulse shapes as multi-component exponential decay functions, with [43] and without [36] the convolution of a Gaussian function representing the response of the photomultiplier.

Table 2.2 shows decay constants and intensities of the decay components, according to an exponential decay of the form:

$$I(t) = I_1 \exp\left(\frac{-t}{\tau_1}\right) + I_2 \exp\left(\frac{-t}{\tau_2}\right) + I_3 \exp\left(\frac{-t}{\tau_3}\right), \tag{2.9}$$

where τ_1, τ_2 and τ_3 are the decay constants for the "fast", "medium" and "slow" exponential decays respectively, and I_1, I_2 and I_3 are their relative intensities. The table has been adapted from Szczesniak et al. [44] and Iwanowska-Hanke et al. [36].

The fitted data confirms that inferior PSD performance of EJ299-33 arises from the similarity between pulse shapes produced by neutrons and gamma-rays. In the case of

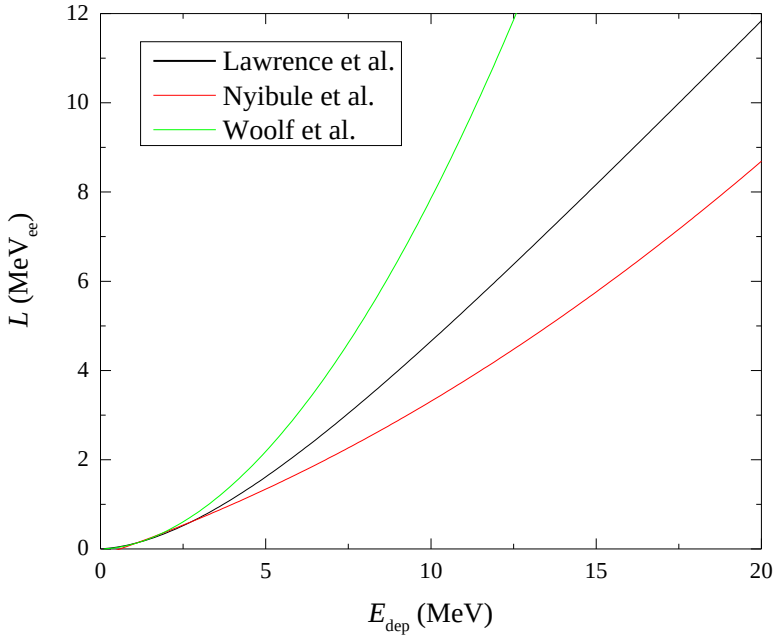

FIGURE 2.6: Fitted relationships between light output L and deposited energy E_{dep} for protons. Adapted from Refs [39]–[41].

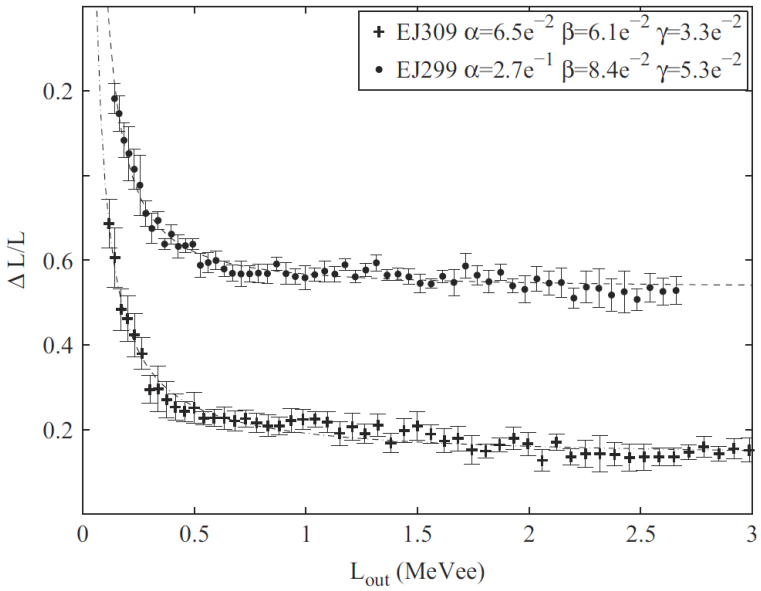

FIGURE 2.7: Light output resolution $\frac{\Delta L}{L}$ versus light output L for EJ299-33 and EJ309 scintillators. Reproduced from [39].

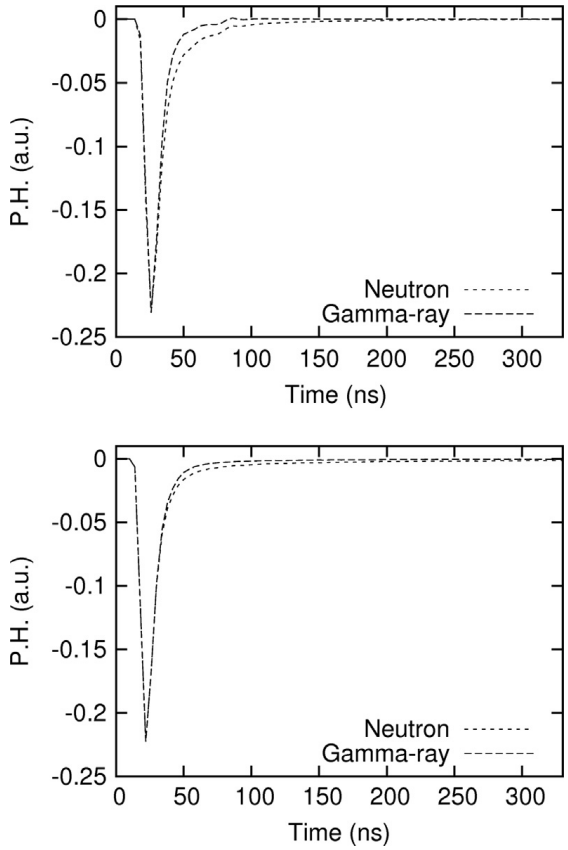

FIGURE 2.8: Average pulse shapes produced by neutrons and gamma-ray in (top) EJ301 and (bottom) EJ299-33 scintillators. Reproduced from [42].

EJ301, I_1 is a factor of 1.75 times larger for gamma-ray events, while it is only a factor of 1.35 times larger for EJ299-33.

As the same underlying mechanism for the appearance of medium and long decay (triplet-triplet annihilation) is present in both gamma-ray and neutron induced scintillation, one should expect the decay constants to match. By using only gamma-ray events to determine the decay constants, and then determining the relative intensities for both neutrons and gamma-rays with fixed decay constants, one can determine a more physically accurate model of pulse shapes. In addition, there is significant dependence of pulse shape on light output for neutron-induced events. As such, a more detailed investigation into the pulse shapes produced by EJ299-33 over a wide light output range is warranted.

Timing resolution is critical for time-of-flight based spectrometry methods. Timing resolution of EJ299-33 was determined by Cester et al. [42], using coincident gamma-rays from a ^{22}Na source, measured using an EJ299-33 based detector and an reference

TABLE 2.2: Decay constants τ and relative component intensities I for pulses produced by gamma-rays and neutrons in EJ301 and EJ299-33 scintillators. Data for EJ301 and EJ299-33 from Refs. [44] and [36] respectively.

Scintillator	Particle	τ_1 (ns)	I_1 (%)	τ_2 (ns)	I_2 (%)	τ_3(ns)	I_3 (%)
EJ301	gamma-rays	4.1 ± 0.4	89	32 ± 3	7	160 ± 20	3
	neutrons	5.2 ± 0.5	51	32 ± 3	23	130 ± 10	17
EJ299-33	gamma-rays	4.6 ± 0.3	73	19 ± 2	16	130 ± 10	12
	neutrons	5.0 ± 0.2	54	22 ± 3	21	180 ± 15	25

EJ-228 fast plastic scintillator detector. A timing resolution of 0.44 ± 0.01 ns was measured, compared to 0.42 ± 0.01 for the EJ228-based detector. EJ299-33 is therefore an ideal candidate for time-of-flight measurements, as it displays a similar rise time to that of EJ228 and EJ301.

2.2 Digital PSD

2.2.1 Background

The availability of fast waveform digitizers, with analogue-to-digital convertors (ADCs) with sampling rates from tens of million samples per second (MSPS) to over a billion samples per second (GSPS), allows for a simple method of pulse shape discrimination, either through digitization of a raw signal pulse from a photomultiplier [45], [46] or through digitization of an integrated charge pulse [47]. Digitization of the signal pulse allows for flexibility as to how PSD is performed. Commonly used analogue techniques, such as charge comparison and zero-crossing techniques have easily implemented digital equivalent algorithms [48], [49]. However, many other algorithms without analogue equivalents have been investigated, such as weighted [47], [50] or logarithmic [51] integration techniques, techniques relying on calculatings of pulse gradients [52], fitting of pulses to model curves [45] or using machine learning techniques [53], [54]. A brief description of some commonly used algorithms is provided in Section 2.2.2, while the implementation of PSD algorithms used in this thesis are described in more detail in Section 3.3. While the PSD algorithms used in the present work are performed off-line, after recording raw pulses, many digital PSD algorithms

can be performed in real-time, through the use of a dedicated FPGA or digital signal processor (DSP).

2.2.2 Commonly used algorithms

Integration-based digital PSD algorithms define a pulse shape parameter as:

$$S = \int_0^T P(t)V(t)dt, \tag{2.10}$$

where T is the integration limit, $V(t)$ is the digitised signal and $P(t)$ is a weighting function defined between $t = 0$ and $t = T$. The commonly used charge-comparison algorithm defines $P(t)$ as a step function, either including or excluding the prompt portion of the pulse up to some predetermined time T_1. A theoretically optimum weighting is given by

$$P(t) = \frac{P_\gamma(t) - P_N(t)}{P_\gamma(t) + P_N(t)}, \tag{2.11}$$

where $P_\gamma(t)$ and $P_N(t)$ are average pulses produced by gamma-ray and neutron interactions respectively [55]. The simple charge-comparison algorithm can produce comparable results to a weighted integration, provided the integration time T_1 is carefully optimised [50].

The zero-crossing algorithm can be implemented digitally via a digital pulse shaping network ($C_1R_1 - (R_2C_2)^2$) [49], or by direct evaluation of the integrated pulse rise time [50]. Nakhostin et al. [49] and Soderstrom et al. [50] show that a digitally implemented zero-crossing technique can outperform a charge-comparison technique across a wide energy range.

Pulse gradient analysis (PGA) defines the pulse shape parameter S as a simplified estimation of the gradient of the pulse between its peak and a fixed time after the peak [52]:

$$S = \frac{V(t_1) - V(t_0)}{t_1 - t_0}, \tag{2.12}$$

where t_0 is the time of the pulse peak, and t_1 is the offset time. While the most basic implementation of this approach relies only on two sample points, improved

results can be obtained through the use of a moving-average smoothing filter [56]. While the initial work on PGA [52] showed a slight improvement in PSD performance over charge comparison algorithms , subsequent comparisons of a number of PSD algorithms have found PGA to produce similar [57] or inferior [56] results.

Simplified digital charge comparison is a wavelet-inspired approach [51], resulting in an integration of the form

$$S = \log \int_{T_0}^{T_1} (V(t))^2, \tag{2.13}$$

where T_0 and T_1 are predefined integration bounds. It has been shown to produce superior results when compared to both PGA [51] and charge-comparison algorithms [57].

2.2.3 Effect of sampling frequency and bit depth

Increasing ADC sampling frequency and bit-depth has been shown to improve PSD performance for a number of digital PSD algorithms [42], [50], [51]. Figure 2.9 shows figure of merit for light output in the 480 $\pm$ 75 keV_{ee} region as a function of bit depth, for 250 MSPS and 500 MSPS digitizers, as calculated using a digital charge-comparison algorithm [42]. The figure indicates that an increase of sampling rate up to 500 MSPS can significantly improve PSD performance. No significant improvements to FoM are observed by increasing bit depth from 12-bit to 14-bit, suggesting that a 500 MSPS digitizer operating at 12-bit is sufficient for charge-comparison PSD.

2.3 Silicon photomultipliers

Silicon Photomultipliers (SiPMs), also referred to as multi-pixel photon counters (MPCCs) comprise of an array of avalanche photo-diodes (pixels or micro-cells) operating in Geiger mode. While each pixel acts purely as a binary photon detector, the combination of several hundreds or thousands of pixels allows for a wide range of light intensities to be measured [58].

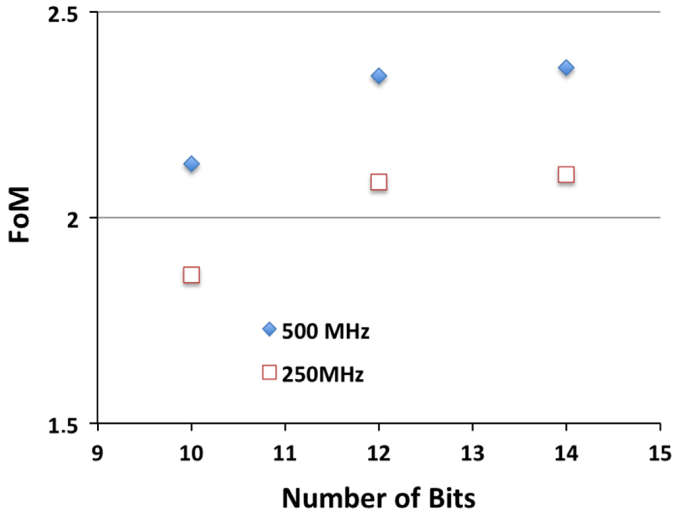

FIGURE 2.9: Figure of merit for the 480 $\pm$ 75 keV_{ee} region as a function of bit depth, for 250 MSPS and 500 MSPS digitizers. Reproduced from [42].

2.3.1 Mechanism

Photons incident on a photo-diode can create an electron-hole pair via the absorption of energy by an electron in the valence band. If a sufficiently high reverse bias (above what is known as the breakdown voltage V_{br}) is applied to the the device, the electric field generated within the depletion region can result in the creation of secondary electron-hole pairs [59]. As these secondary pairs also travel through the electric field, this can lead to an avalanche of pair production. In this fashion, single photons or thermal noise can generate a current that can be measured directly [60].

A quenching resistor, placed in series with the diode limits the diode current and decreases the bias below the breakdown voltage, preventing further avalanche production. The diode then recharges over the course of the diode's characteristic recovery time, typically of the order of tens or hundreds of nanoseconds. Figure 2.10 shows the circuit diagram for an individual pixel, comprising of a photo-diode and quenching resistor, as well as that of the pixel array.

2.3.2 Operating Characteristics

Typical breakdown voltages of SiPMs are in the region of 30 V, well below the high operating voltages required for conventional PMTs. Devices are typically operated between 2 V and 5 V above the breakdown voltage. Individual pixel gain G is given as

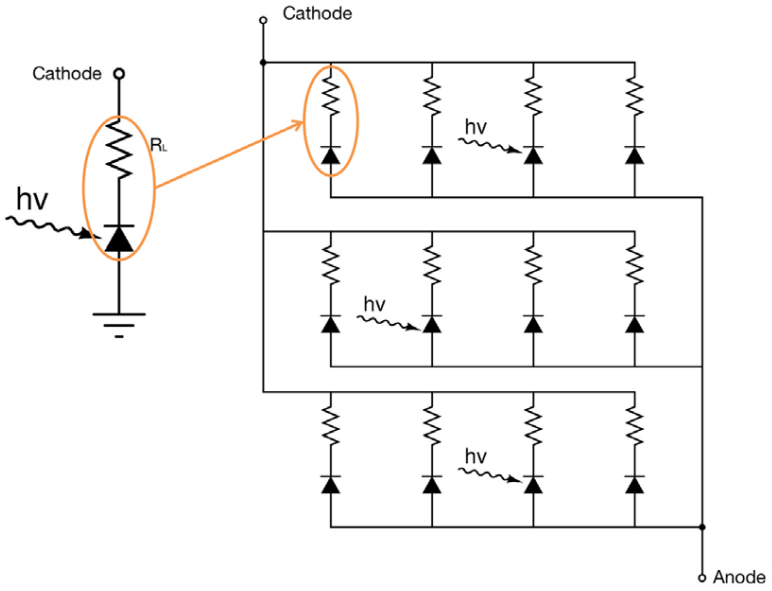

FIGURE 2.10: Circuit diagram for an individual pixel (left) and a pixel array in a silicon photomultiplier. Reproduced from [59].

$$G = \frac{C(V - V_{\mathrm{br}})}{e}, \tag{2.14}$$

where C is the effective pixel capacitance, e is the electron charge and V is the operating voltage. Gain is therefore proportional to the difference between operating voltage and V_{br}, also known as the over-voltage V_{over}. Breakdown voltage is temperature-dependent, with typical shifts of 20 mV/K [61].

For events resulting in the detection of multiple simultaneous photons across a number of pixels, the output current will be proportional to the product of the individual pixel gain G, as well as the photon detection efficiency (PDE). PDE is a product of three independent factors: the wavelength-dependent quantum efficiency of the photodiode η, the voltage-dependent probability of avalanche production ϵ, as well as the geometric fill factor of the device itself F [59]:

$$PDE(\lambda, V) = \eta(\lambda) \times \epsilon(V) \times F. \tag{2.15}$$

The wavelength dependence of a SiPM's PDE is dependent on the pixel size, as well as the diode structure. Blue-sensitive SiPMs can have a PDE of over 40% in the 400-450 nm wavelength range [62].

Thermally generated carriers produce pulses identical to those produced by individual photons. As such, these "dark pulses" are a primary source of noise in SiPMs, rather than electronic noise [58]. The dark count rate for SiPMs is typcally in the kHz or MHz range [63]. Measurements of integrated current produced by these dark counts are known as "dark current", and are generally of the order of a few μA. Dark count rates are typically linear with over-voltage [59], and reducing the operating temperature will reduce the number of thermally generated carriers, reducing dark count rates [60].

During avalanche breakdown, photons with energies above the band gap of silicon can be emitted (typically at temperature-independent rates of 10^{-5} per carrier [64]). These photons can travel across pixel boundaries and create separate avalanche breakdowns in neighbouring pixels. This process is known as optical crosstalk. Carriers can also be trapped and released after a delay of up to a few microseconds [65], resulting in after-pulsing.

Measurements of dark count rates before and after exposure to proton radiation have shown significant increases in dark counts after radiation exposure [66], due to the generation of defects in the silicon lattice.

Pixel recovery time depends on pixel size [61] and operating voltage [65]. During this time, any photons incident on the same pixel will not generate an avalanche while the effective voltage is below the breakdown voltage. As such, there is an upper limit to the number of simultaneously generated avalanches, even for very high photon counts. This leads to a saturation effect, where the number of pixels fired N_{fired} is a function of the number of incident photons N_{photons}, photon detection efficiency, as well as the total number of pixels N_{pixels} [59]:

$$N_{\text{fired}} = N_{\text{pixels}} \left(1 - \exp\left(\frac{N_{\text{photons}} \times PDE(\lambda)}{N_{\text{pixels}}}\right)\right) \tag{2.16}$$

Saturation can be decreased by increasing N_{pixels}.

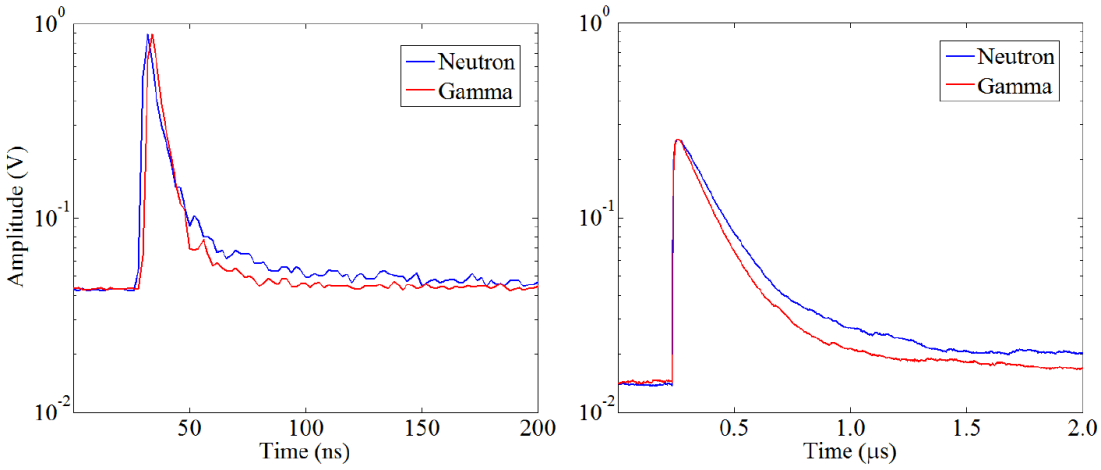

FIGURE 2.11: Pulse shapes produced by 1 MeV_{ee} neutrons and gamma-rays in stilbene, coupled to (left) a conventional PMT and (right) a SensL MicroFB SiPM. Reproduced from [67].

2.3.3 Pulse shape discrimination with SiPMs

A number of groups have investigated pulse shape discrimination using SiPMs, using single-crystal stilbene [54], [67], [68], plastic scintillator [69]–[71] and CLYC inorganic scintillator [72].

Figure 2.11 shows typical pulse shapes produced by 1 MeV_{ee} neutrons and gamma-rays in stilbene, coupled to a conventional PMT and a SensL MicroFB-60035 SiPM [67]. Due to the recovery time of the SiPM microcells, the signal takes an order of magnitude longer to return to the baseline. As such, conventional pulse shape algorithms must be carefully adapted or optimised in order to produce efficient discrimination. While most works have simply chosen to adapt the widely used charge comparison method of PSD, using significantly wider time intervals [68], it appears that a modification of the optimal filter algorithm described in Section 2.2.2 is capable of producing significantly improved results [54]. An alternative algorithm, Frequency Gradient Analysis (FGA) was shown to improve results over conventional charge comparison methods when using SiPM-based detectors [71].

Comparisons between PSD performance of stilbene when coupled to conventional PMTs, SensL MicroFB and MicroFC SiPMs are given by Ruch et al. [68]. Figures of merit of 1.93, 1.37 and 2.13 were calculated for the PMT-, MicroFB- and MicroFC-based detectors respectively, with the significant improvements of the MicroFC-based detector arising from reduced dark current [61].

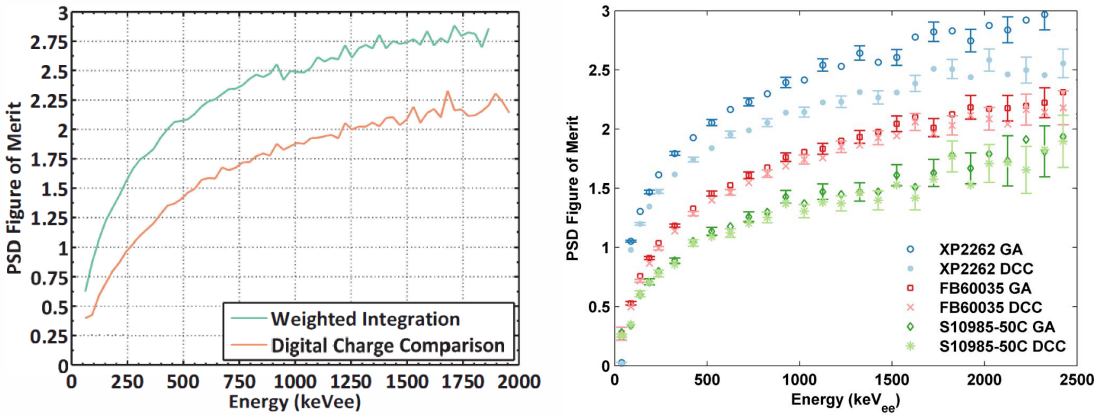

FIGURE 2.12: (a) Figure of merit versus light output for SiPM-based stilbene detector, for the conventional charge comparison algorithm and an optimised weighted integration algorithm. Reproduced from [54]. (b) Figure of merit versus light output for PMT- and SiPM-based EJ299-33 detectors, for the conventional charge comparison algorithm (DCC) and an optimised weighted integration algorithm (GA). Reproduced from [69].

Preston et al. [54] investigated the use of a genetic algorithm to determine the optimal filter to apply for SiPM-based detectors. Figure 2.12(a) shows FoM versus light output, for neutrons produced by a D-T neutron generator incident on a stilbene crystal coupled to a Hamamatsu SiPM array. The weighted integration algorithm, with weights determined by a genetic algorithm, displays significantly improved PSD performance over the conventional charge comparison algorithm. However, a more recent investigation [69] showed a far more subtle improvement to FoM when using a weighted integration algorithm, when using both stilbene and EJ299-33 scintillators. Figure 2.12(b) compares FoM for both charge comparison and weighted integration methods for EJ299-33 scintillators coupled to a conventional PMT (XP2262), as well as 6×6 mm^2 SensL MicroFB-60035 and Hamamatsu S10985-050C SiPMs, reproduced from [69]. The improvements observed in Ref. [54] are not observed, and the weighted algorithm appears to benefit the PMT-based detector more significantly. This suggests that a carefully optimised charge comparison algorithm can consistently perform as well as the more complex weighted integration algorithm on SiPM-based devices. In addition, results from Refs. [68] and and [69] show that PSD performance of SiPM- and PMT-based detectors are comparable, with PSD performance strongly dependent on the choice of SiPM. SensL MicroFC SiPMs are shown to produce the highest quality PSD, and have been chosen for measurements described in this thesis.

Chapter 3

Development and characterization of a digital DAQ

One of the primary goals of the research described in this thesis was the custom development and implementation of a digital data acquisition system, capable of supporting signals originating from both conventional PMT- and SiPM-based detectors. This chapter describes the development and characterization of a digital data acquisition system, supporting a variety of detectors and digitizers across a wide energy range. It presents the first use of digital pulse shape discrimination at high energies, using neutrons produced by the iThemba LABS cyclotron facility.

3.1 Description

An open-source digital data acquisition (DAQ) software package, "QtDAQ" [73], was developed in C++ in this work, utilizing the open source Qt5 framework [74]. QtDAQ is designed to handle the readout and analysis of digitised signals from several digitizers, as well as temperature monitoring and detector voltage control through communication with a microcontroller. Digitised signals can be saved to disk in unprocessed form and read back in QtDAQ for off-line analysis.

A number of commonly used pulse processing algorithms are implemented, and each digitised signal is automatically processed to produce an event statistics structure, comprising of individual channel statistics, such as the total integral of the signal, pulse shape parameter, baseline and constant fraction discriminator (CFD) timing, as well as statistics common to all channels, such as trigger information or detector temperature.

TABLE 3.1: List of event statistics parameters

Parameter	**Description**
Baseline	Signal baseline, taken as the mean value of a number of samples at the beginning of the signal.
Long integral (Q_L)	Signal integral,from t_{Start} to t_{Long}, representing,the total light output of the event.
Short integral (Q_S)	Signal integral from t_{Start} to t_{Short}, representing the light output of the event within the short time gate.
PSD Factor (S)	Percentage of the signal integral within the short time gate.
Time of CFD crossing (t_0)	Time at which the CFD of the digitised signal crosses a predefined threshold.
Max value	Maximum value of the signal.
Min value	Minimum value of the signal.
Temperature	Temperature of the detector, as read in from the microcontroller.
Time from first event	Time from the first event of the current measurement set.
Custom 1-5	Custom parameters, manipulated by user-defined JavaScript code.

In addition to predefined parameters, five custom parameters are calculated for each event, which can be used for additional analysis. Table 3.1 lists a description of the parameters contained in the event statistics structure.

QtDAQ is designed for flexibility, presenting a multi-window environment, where any number of plots may be added to a number of tabs. Three basic plot types are implemented:

- **Signal plots:** A plot of the digitised signals captured by the digitizer. The signals from multiple channels can be superimposed for comparison.
- **1D Histograms:** A plot of counts against a parameter selected from Table 3.1.
- **2D Histograms:** A 2D plot of counts against any two parameters selected from Table 3.1, with the counts displayed through a colour scale.

An example of the multi-window environment is shown in Figure 3.1. Cuts can be defined in the following forms:

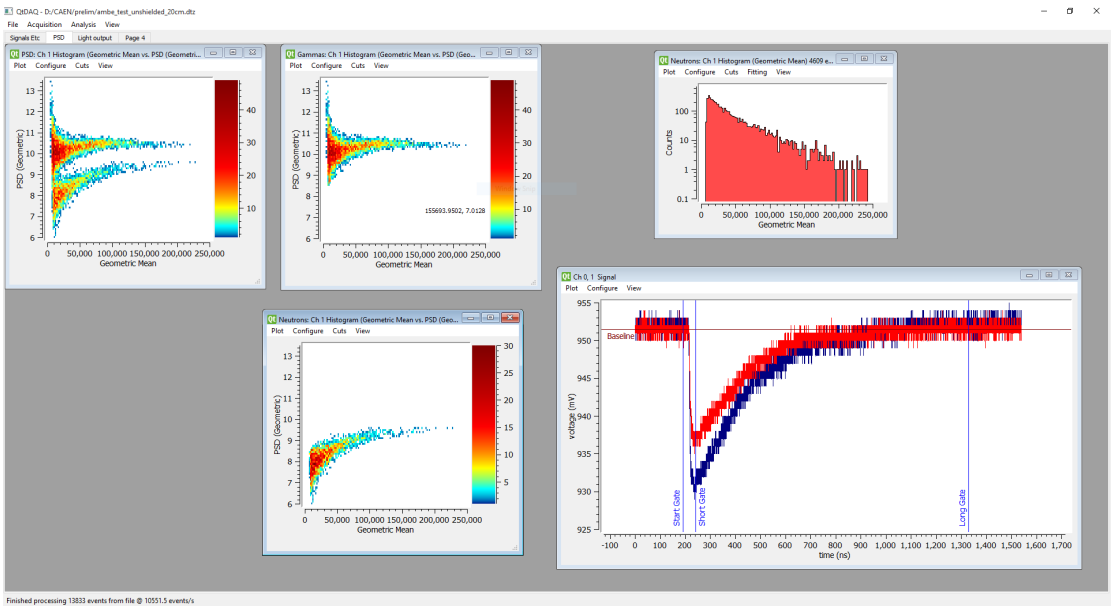

FIGURE 3.1: A multi-window session in QtDAQ.

- **Linear cuts:** For a specified parameter, histograms can include only events lying above or below a specified value.

- **Regional (polygonal) cuts:** For a pair of specified parameters, histograms can include only events lying inside or outside of a polygonal region, defined through a series of points chosen on a 2D histogram.

Plots and cuts can be saved to a template, for easy reuse.

3.1.1 Supported hardware configurations

QtDAQ supports the readout of digitised signals from a number of CAEN digitizers (VX1761, VX1742 and DT5730), utilising the CAENDigitizer software library [75] for high level control and readout. Communication between digitizer and PC takes place across a CONET2 optical connection, with transfer speeds of up to 80 MB/s. The compact USB-connected PSI DRS4 Evaluation board [76] is also supported. QtDAQ is compatible with Windows 7, 8 and 10, as well as modern x86-based Linux distributions.

3.1.2 Multi-threaded readout and processing

In order to maximise the supported event rate, a multi-threaded and double-buffered approach is used. Acquisition, whether from a digitizer or a storage device, is performed in a separate thread, and events are stored in memory in an event buffer. A second thread handles processing of data and execution of user-defined JavaScript code. A third thread handles user interactions and the updating of plots.

When the event buffer reaches its predefined capacity, the buffer is unlocked, and the acquisition thread switches to the secondary buffer. Once the secondary buffer reaches its capacity, it is unlocked and the acquisition thread switches back to the primary buffer. At each buffer swap, the acquisition thread waits until the next buffer has been unlocked by the processing thread. This approach increases the maximum supported event rate over a single threaded approach significantly by utilising multiple CPU cores.

3.1.3 Data compression and event packing

The readout of digitised signals at high event rates requires significant transfer bandwidth and storage capacity. For a typical setup, an uncompressed two-channel digitised signal requires approximately 25 KB per event. At a rate of 4000 events/s, this translates to 100 MB/s. In order to reduce the size of stored events, QtDAQ implements data compression while writing unprocessed events to a storage device. Two compression formats are supported: for superior compression at lower event rates, ZLib [77], [78] is utilised, while LZO [79] is utilised for faster compression at higher event rates.

A common property of digitised signals read out from photomultipliers at a high sampling rate is that neighbouring signal samples seldom differ by a significant amount, due to the pulse shapes produced by the photomultiplier. As an example, when reading out at a 10-bit bit depth, the difference between successive samples can often be expressed by an 8-bit number. QtDAQ exploits this property in order to further reduce storage requirements: by storing the initial sample of a signal at the original bit depth, followed by the differences between successive samples, stored at a reduced bit depth, the storage size of an event can be significantly reduced. As the reliability of

```
var L1 = chStats[1].longGateIntegral;
var S0 = chStats[0].shortGateIntegral;
var S1 = chStats[1].shortGateIntegral;
chStats[1].custom3 = Math.sqrt(L0*L1);
chStats[1].custom4 = 100*Math.sqrt(S0*S1)/chStats[1].custom3;
```

FIGURE 3.2: Code snippet for calculating total light output and pulse shape parameter from two individual channels.

this technique depends strongly on the shape of the digitised signal, it is an optional optimisation in QtDAQ.

3.1.4 JavaScript engine for flexible analysis

In addition to performing pre-defined pulse processing algorithms, the user can define JavaScript code to be run as each digitised signal is processed, with the results of calculations stored in custom parameters. Possible applications of this feature include time-of-flight calculations, event rejection using high-level logic, or the combining of statistics between channels. User-defined JavaScript code is executed at five stages during analysis: Init (Before analysis begins); Pre-event (before each event is analysed); Post-channel (after each channel in an event is analysed); Post-event (after each event is analysed) and Final (after analysis of all events completes). An example of post-event JavaScript code to calculate the total light output and pulse shape parameters for a two-channel detector through a geometric mean of the individual channel parameters is shown in Figure 3.2.

JavaScript code execution in QtDAQ is facilitated through embedding of the Google V8 JavaScript engine [80]. JavaScript was chosen above interpreted languages such as Lua or Python, due to execution speed. Code is recompiled as soon as changes are detected, greatly increasing execution speed.

3.1.5 Voltage control and temperature monitoring

A number of measurements described in this work make use of SiPMs connected to a B&K 9120A bench power supply. Voltage can be adjusted and monitored in QtDAQ through serial communication with the power supply, with support for voltage adjustment through user-defined JavaScript code.

TABLE 3.2: Comparison between CAEN digitizers.

Parameter	**VX1761**	**DT5730**	**Notes**
Form factor	VME	Standalone	
Communication	VME or CONET	CONET or USB	CONET: 80 MB/s USB: 30 MB/s
Channels	2	8	
Sampling rate	4 GSPS	500 MSPS	
Bit-depth	10-bit	14-bit	
Voltage range	1.0 V	0.5 V or 2.0 V	DT5730: Software selectable range

The temperature-dependence of SiPM gain and breakdown voltage is well-documented [58], [61]. If this temperature dependence is carefully characterised, it is possible to adjust the detector voltage based on temperature measurements. Alternatively, temperature-dependent variations in gain can be accounted for during signal processing while keeping the detector voltage fixed. Both approaches are supported by QtDAQ. Temperature monitoring in QtDAQ is performed by serial communication with an Arduino microcontroller, connected to an LM35 temperature sensor [81]. PMTs were powered by a Ortec 556 high voltage power supply.

Additional details on QtDAQ, including example analysis templates and installation procedure, are given in Appendix A.

3.2 Detectors and electronics

3.2.1 Digitizers

Two CAEN digitizers were utilised in the measurements described in this work. The VX1761 is a 2-channel VME form factor digitizer, with a sampling rate of 4 GSPS, and a bit-depth of 10-bit [82]. The DT5730 is an 8-channel standalone desktop digitizer, with a sampling rate of 500 MSPS, and a bit-depth of 14 bits [83]. A comparison between the technical specifications of the two digitizers is given in Table 3.2. Both digitizers utilise fast flash ADCs read out by an FPGA, and have the same basic principle of operation:

- **Analogue signal conditioning:** The positive terminal of the micro-coaxial (MCX) input is connected to an operational amplifier, to ensure that the input voltage

lies within the input range of the ADC. A 16-bit DAC provides a programmable DC offset as a reference voltage. In the case of the DT5730, the input undergoes amplification through a programmable gain amplified before reaching the op-amp. This allows for both 0.5 V and 2.0 V input voltage ranges. A circuit diagram for the analogue input of the DT5730 is shown in Figure 3.3.

- **ADC Readout:** The conditioned signal inputs are constantly sampled by a flash ADC, the output of which is fed into an ADC and Memory Controller (AMC) FPGA. Both the VX1761 and DT5730 contain two AMCs, with each AMC servicing 4 four channels in the case of the DT5730.

- **Event buffer storage:** Samples are stored in one of a number of circular event buffers. The acquisition window has a programmable size and the event buffer is frozen for readout after a programmable delay, once a trigger is issued. As soon as the buffer is frozen, acquisition continues in a new buffer. Both digitizers support up to 1024 event buffers per channel, depending on the number of samples captured per event.

- **Triggering:** Triggers can be issued from an external source (via a NIM or TTL standard signal), manually through software control, or through an automatic trigger determined by individual channel triggers. Channel triggers are issued when samples cross a programmable threshold. These channel triggers are propagated to central trigger logic in the Readout Controller (ROC) FPGA, which then issues a common trigger, depending on coincidence logic of the channel triggers. A trigger time tag, of 16 ns resolution, is stored when a common trigger is issued.

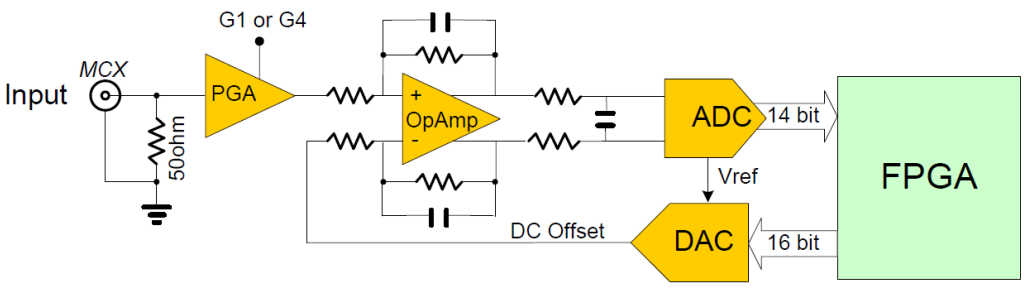

FIGURE 3.3: Analogue input for DT5730. Reproduced from [83].

- **Readout:** The ROC handles communication with other devices, across a number of possible interfaces. The VX1761 can transfer data through a VME interface at up to 200 MB/s, or via a proprietary optical connection (CONET) at up to 80 MB/s. Communication over CONET requires a PC equipped with an optical controller card. The DT5730 can transfer data via CONET or a standard USB 2.0 interface. Event data comprises of an event info structure, containing information on the active channels, trigger source and timing, followed by raw channel data for each active channel. Events can be read out one-by-one, or can be read out in buffered blocks, increasing the maximum event throughput.

The significantly higher sampling rate of the VX1761 make it ideally suited to situations where timing information is critical, such as time-of-flight measurements or measurements with fast PMTs. The higher bit-depth of the DT5730 makes it well suited to measurements of smaller signals, allowing trigger thresholds to be set significantly lower, and for efficient PSD down to lower energies. For SiPM measurements, the sampling rate of the DT5730 is sufficient, due to the long signal decay time arising from the microcell recovery time.

3.2.2 Scintillators

Measurements described in this work were taken using one of three scintillator configurations. For reference measurements and characterization of the Eljen EJ299-33 scintillator, a cylinder of EJ299-33 plastic (51 mm diameter $\times$ 51 mm) was optically coupled to an ETL9214 12-stage photomultiplier tube with EJ-560 silicone rubber of thickness 1 mm. The scintillator was painted with EJ-520 reflective paint. An encapsulated Eljen EJ301 liquid scintillator of the same dimensions and the same base electronics was used for comparative measurements. EJ301 is chemically identical to the widely used NE213 scintillator, and has been shown to have excellent PSD across a wide energy range [84]. PMT voltages were chosen to ensure that signals peaked between 50 mV and 900 mV, in order to utilise as much of the range of the digitiser as possible, while avoiding voltage saturation.

SiPM-based detectors were constructed using EJ299-33, cut into a rectangular cuboid of dimensions $6 \times 6 \times 50$ mm^3 and polished on each side, with the dimensions of

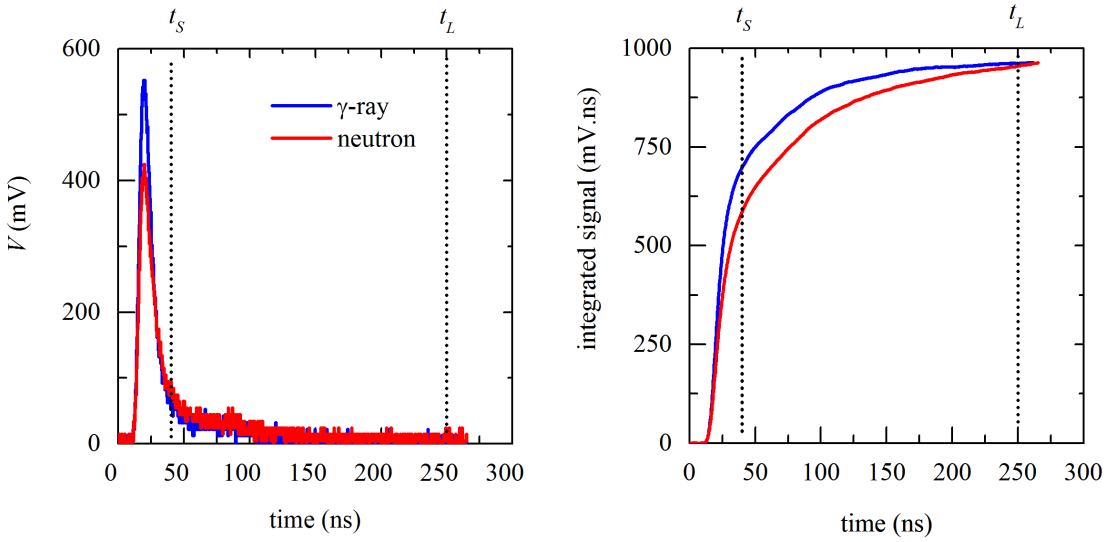

FIGURE 3.4: (a) Digitised pulses and (b) pulse integrals for events arising from neutron and gamma-ray interactions in the EJ301 scintillator. The pulses have the same total integral, and are shown after baseline subtraction. Integration times t_S and t_L are indicated.

the smaller sides matching the active area of the MicroFC-60035 SiPMs. SiPMs were coupled to the scintillator with EJ-560 silicone rubber or Dow Corning 200 silicone grease. The scintillators were wrapped in a highly reflective material to optimise light collection, with an outer wrapping of black vinyl tape to shield the scintillator from ambient light. Two reflective materials were used: 3M Vikuiti Enhanced Specular Reflector (ESR) material and Tyvek 1073B material. ESR is a highly reflective film, providing over 98% specular reflection, while Tyvek is a primarily diffuse reflector.

As the behaviour of EJ301 as been previously well-documented at high energies [84]–[86] using traditional analogue electronics, the characterisation of the digital DAQ described in this chapter was performed exclusively using the EJ301-based detector.

3.3 Digital pulse processing

Figure 3.4 (a) shows typical digitised pulses produced by neutron and gamma-ray interactions with the EJ301 detector. The corresponding cumulative signal integrals are shown in Figure 3.4 (b). The baseline for each event, taken as the mean value of a number of samples preceding the leading edge of each pulse, has been subtracted to avoid the effect of voltage drift in the PMT.

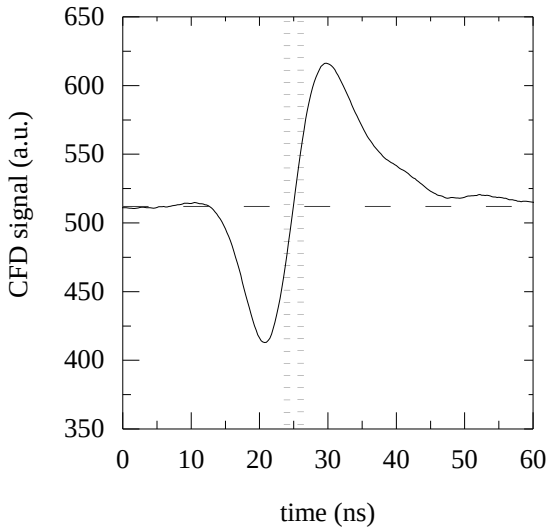

FIGURE 3.5: Typical digitised pulse after application of the digital CFD filter. The dotted lines indicate the region used to determine the time of intersection of the filtered signal with the baseline (dashed line).

In order to perform PSD, pulses must be aligned in a consistent manner. A signal start time t_{Start} must be defined in a way that minimises effects due to variations in pulse noise, baseline, amplitude and shape. A software-implemented digital constant fraction discriminator filter (CFD) filter was applied to each digitised signal. The filtered signal v takes the form of

$$v_i = \sum_{j=1}^{N} f \times V_{i-j} - V_{i-j-D} \, , \tag{3.1}$$

where V is the unfiltered signal, N is the filter length, D is the filter offset and f is the filter fraction [87].

Figure 3.5 shows an example of a digitised pulse after application of the digital CFD filter. A linear fit to the region of the pulse indicated by the dotted lines in Figure 3.5 was used to determine the time of intersection of the filtered signal with the baseline, indicated by the dashed line. The time t_{Start} was then determined as the time of this intersection minus a constant offset t_{Offset}, in order to include the entire pulse in further calculations. Values of t_{Offset} for PMT-based and SiPM-based detectors were 25 ns and 40 ns respectively, with the difference arising from the variation in pulse rise times.

The values of the parameters in Equation 3.1 were chosen to optimise the time resolution of the acquisition system, which was determined by splitting a test signal across

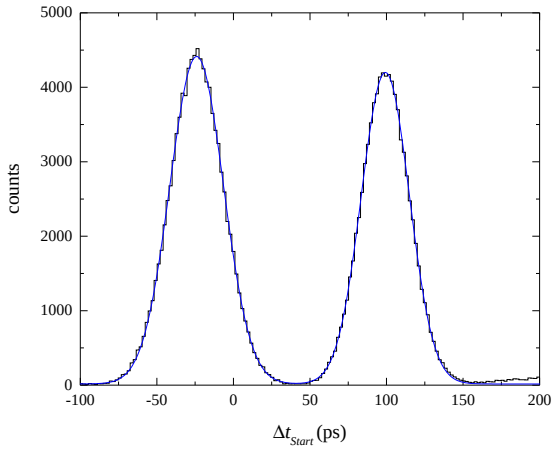

FIGURE 3.6: Counts versus the difference between start times $\Delta t_{\mathrm{Start}}$ for test signals from a PMT, shown with the data fitted to a double Gaussian function.

two digitizer channels and calculating the FWHM of the distribution of differences between signal start times. Figure 3.6 shows counts versus the difference between start times $\Delta t_{\mathrm{Start}}$ for test signals from a PMT. Two cable lengths were used, resulting in two distinct distributions, with FWHMs of 41.1 ± 0.1 ps and 36.9 ± 0.1 ps. Typical FWHMs of 40 ps were calculated for PMT-based detectors read out with both the VX1761 and DT5730 digitizers, well below the sampling interval of 250 ps and 2 ns respectively. FWHMs of 150 ps were calculated for SiPM-based detectors read out with the DT5730 digitizer. The poorer time resolution for SiPM-based detectors is due to the increased rise time of SiPMs compared to that of PMTs.

Charge comparison PSD

For each recorded event, a "signal integral" parameter Q_L was calculated by integrating the digitised signal over a time interval (t_L), starting from t_{Start}. The value of t_L was chosen in order to capture as much of the entire signal as possible, while still avoiding saturation of the available output bandwidth of the digitizer. A second parameter Q_S was calculated by integrating the pulse over a shorter time interval (t_S). A pulse shape parameter S was then defined as

$$S = k\frac{Q_S}{Q_L} + C \tag{3.2}$$

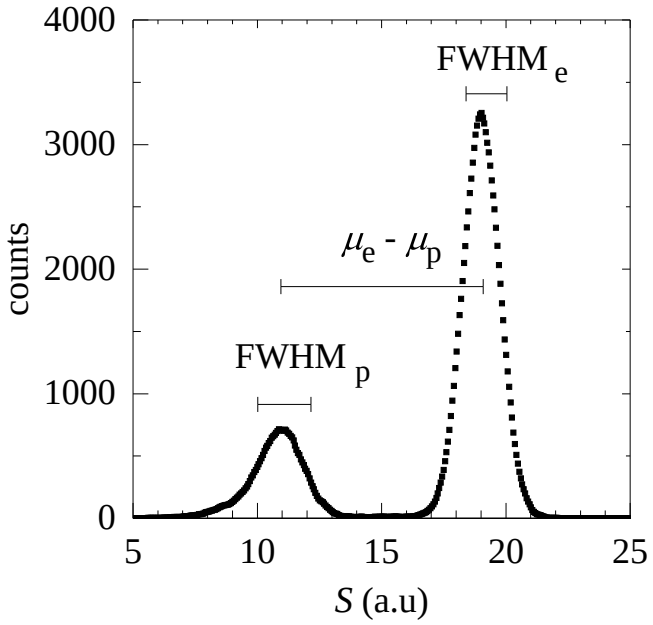

FIGURE 3.7: Counts versus pulse shape parameter S for events of a similar Q_L, measured using the EJ301-based detector.

which is the basis of a charge comparison method of PSD. Constants k and C were chosen in order to appropriately scale and offset S. Signals arising from gamma-ray interactions with the detector have a reduced slow decay component in comparison to those arising from neutron interactions. Therefore, a larger proportion of light output occurs within the shorter time interval in gamma-ray events, leading to higher values of S when compared to neutron events of a similar light output.

In an ideal detector, statistical fluctuations in pulse shape lead to Gaussian distributions of S for gamma-ray and neutron events with equal values of Q_L. An example of the distributions of S arising from measurements using the EJ301-based detector is shown in Figure 3.7. The distribution on the left is due to the interaction of elastically recoiled protons with the scintillator, while the distribution on the right is due to the interaction of Compton-scattered electrons with the scintillator. The pulse shape is dependent on the specific energy loss in the scintillator. Therefore, S changes as a function of light output and cuts made to discriminate between pulse classes based on S must take this dependence into account.

A figure of merit (FoM) is a useful means to provide a quantitative measurement of the separation between the distributions of S for two pulse classes [26]. The FoM for

the distributions shown in Figure 3.7 is 2.2. The PSD algorithm used, along with parameters such as t_S, will affect the separation between distributions of S. Optimisation of the FoM by varying algorithms and parameters can therefore lead to determining the most effective method of PSD for a particular experimental setup.

In addition to the charge comparison approach illustrated above, methods based on zero-crossing timing and the application of a linear filter were also implemented on the same data sets.

Zero-crossing PSD

The zero-crossing algorithm uses a combination of filters to shape integrated pulses into a bipolar signal, and determines the time at which the signal switches polarity. This “zero-crossing" of the bipolar signal will be dependent on the rise time of the integrated pulse, and can therefore be used to classify pulses. This method has been shown to outperform the digital charge comparison algorithm under certain conditions [49].

An alternative implementation of the zero-crossing algorithm, utilised in this work, evaluates the rise time of the cumulative integral of the signal, without a pulse shaping network [50]. The evaluation of the rise time is performed by determining the difference between the times at which the integrated signal crosses low and high thresholds. Thresholds were chosen in order to optimise the FoM, with typical values of 15% and 65% of Q_L for low and high thresholds, respectively.

Linear Filter PSD

The linear filter algorithm is a generalised implementation of the charge comparison method. In this approach, the shape parameter S is defined by

$$S = \frac{\sum P_i V_i}{\sum V_i} \tag{3.3}$$

where V is the digitised signal and P is a weighting vector with the same number of samples as the digitised signal. For the case of charge comparison, P is a step function with a value of unity within the short time interval and zero elsewhere. Theoretical

calculations show that the optimal weights which maximise the FoM under ideal conditions are

$$P_i = \frac{W_{Ni} - W_{\gamma i}}{W_{Ni} + W_{\gamma i}} \tag{3.4}$$

where W_{Ni} and $W_{\gamma i}$ are the digitised samples of the average pulse shapes from neutron and gamma-ray events respectively [55].

The use of a genetic algorithm to determine optimal weights by performing a non-exhaustive search though all possible forms of P has been previously demonstrated [54] and was implemented. Rather than optimising P directly, a shortened weighting vector was optimised and then interpolated to determine P. The reduction of the vector length enables a significantly shorter computation time. It was found that increasing the number of weights above 100 did not improve results noticeably.

3.4 Experimental measurements

Radiation for calibration and detector characterization was provided by three methods: radio-isotopic sources provided gamma-rays of known energies, as well as neutrons with energies up to approximately 10 MeV; a ^{2}H-^{3}He (D-T) neutron generator provided monoenergetic neutrons of 14 MeV energy and proton beams produced at the iThemba LABS cyclotron facility provided quasi-monoenergetic neutron beams of energies up to 140 MeV.

3.4.1 Gamma-ray calibration sources

A number of gamma-ray emitting radio-isotopic sources were utilised for detector calibration. As gamma-rays interact with organic scintillators primarily via Compton scattering, measurements of the Compton edges of gamma-rays with a known energy were used to calibrate light output spectra. The energy of the Compton edge, E_C, corresponding to the energy that a fully backscattered gamma-ray transfers to an electron, is given by

$$E_C = \frac{E}{1 + m_e c^2/2E}, \tag{3.5}$$

TABLE 3.3: Radioactive sources utilised, with gamma-ray energies and Compton edge energies.

Source	γ-ray energy (keV)	E_C (keV)
^{137}Cs	662	478
^{22}Na	511, 1275	341, 1062
^{54}Mn	835	639
^{207}Bi	569, 1063	393, 857

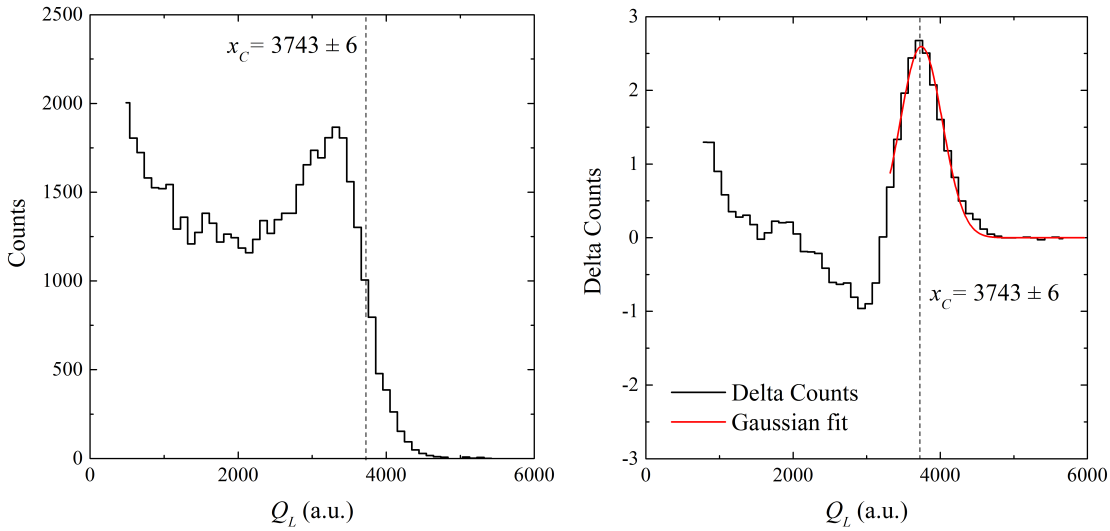

FIGURE 3.8: (a) Counts versus signal integral (Q_L) for ^{137}Cs gamma-rays incident on EJ-301. (b) Derivative spectrum, with Gaussian fit to determine Compton edge and energy resolution. The plot has been vertically inverted for comparison.

where E is the energy of the incident gamma-ray and $m_e c^2$ is the electron rest mass energy. Table 3.3 shows a list of radioactive sources utilised, along with their primary gamma-ray energies and corresponding Compton edge energies.

Figure 3.8(a) shows a plot of counts versus signal integral Q_L for ^{137}Cs gamma-rays incident on a PMT-based EJ-301 detector, after subtraction of a measured background spectrum. In order to determine the position of the Compton edge in a reproducible manner, the spectrum can be smoothed with a moving-average filter, and differentiated. The tail of this derivative spectrum is approximately Gaussian [88], and can be fitted to determine the centroid, corresponding to the position of the Compton edge. Figure 3.8(b) shows the derivative spectrum, along with a Gaussian fit of the tail. In addition to determining the position of the Compton edge, the Gaussian fit can provide a consistent manner of estimating the energy resolution of the detector. While

this method is considerably simpler than Monte-Carlo based alternatives [89]–[91], comparisons between energy resolutions estimated in this manner require that width of the smoothing filter, as well as the region used in the fitting processes, are defined in a consistent manner.

As the light output produced by a charged particle in a scintillator depends both on the incident energy and particle type [92], [93], a light output parameter L was defined in MeV electron equivalent units ($\mathrm{MeV_{ee}}$), relating the light output to the number of photons produced by an electron of a given energy. As the linearity of liquid and plastic scintillators' response to electrons is well established [94], a linear fit of gamma-ray energy to the position of the Compton edge was considered sufficient to determine the relationship between L and Q_L for detectors based on PMTs.

3.4.2 Americium-Beryllium (Am-Be) neutron source

A 2 GBq ^{241}Am-^{9}Be (Am-Be) radio-isotopic source was used as reference neutron source, producing neutrons with a complex energy spectrum, with a maximum of approximately 10 MeV. Neutrons are produced by the $^{9}\mathrm{Be} + \alpha \rightarrow n +^{12}$ C reaction (Q-value of 5.70 MeV) [95], with alpha particles provided by the decay of ^{241}Am. In addition to neutrons, 4.44 MeV gamma-rays are produced by the Am-Be source through the decay of the excited state of ^{12}C. The ISO reference neutron energy spectrum for Am-Be sources [96] is shown in Figure 3.9. In this energy range, neutrons interact with Hydrogen-rich organic scintillators primarily via elastic n-p scattering.

Figure 3.10 shows the distribution of events as a function of light output parameter L and pulse shape parameter S, for neutrons and gamma-rays from the Am-Be source incident on the EJ301-based detector. The loci associated with recoiling electrons from Compton scattering events (gamma-rays) and protons recoiling from n-p elastic scattering (neutrons) are well separated over the full range of L. The "soft" slanted threshold at low L is the result of dependence of the VX1761 digitiser trigger on pulse height, rather than pulse integral. This leads to a lower threshold in L for gamma-ray events, since these pulses have a shorter decay time.

The dotted line shows a cut used to separate events associated with neutrons from those associated with gamma-rays. The projections of the neutron and gamma-ray

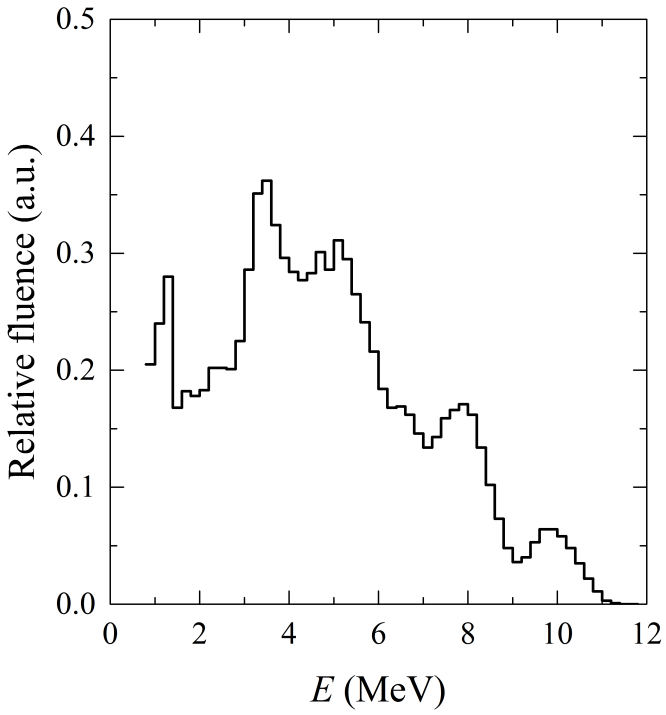

FIGURE 3.9: Am-Be source reference neutron energy spectrum. Adapted from [96].

selections onto the L-axis are shown in Figures 3.11 (a) and (b) respectively. The complex neutron energy spectrum gives rise to a smooth light-output spectrum, which can be unfolded using a carefully calibrated set of response functions to recover the incident neutron energy spectrum. The Compton edge of the 4.44 MeV gamma-rays is visible at 4.20 MeV_{ee} in (b), and can be used as a calibration point in larger detectors. The double escape peak, arising from the escape of both annihilation photons after e+e- pair production in the scintillator, is visible at 3.42 MeV_{ee} . The feature visible at approximately 2 MeV_{ee} is due to the Compton scattering of 2.23 MeV gamma-rays arising from $^{1}\mathrm{H}(\mathrm{n},\gamma)\mathrm{d}$ interactions in materials surrounding the detector.

3.4.3 Deuterium-Tritium (D-T) neutron generator

Sealed tube neutron generators based on the $^{2}\mathrm{H} -^{3}\mathrm{He}$ (D-T) and $^{2}\mathrm{H} -^{2}\mathrm{H}$ (D-D) reactions are widely used in laboratories and in the field for a number of applications, such as the detection of contraband [4], [97] and buried explosives [98], [99], cargo inspection [100], [101] and in-vivo neutron activation analysis [102], [103]. They provide a controllable, compact and portable source of neutrons of a specific energy (14.1 MeV

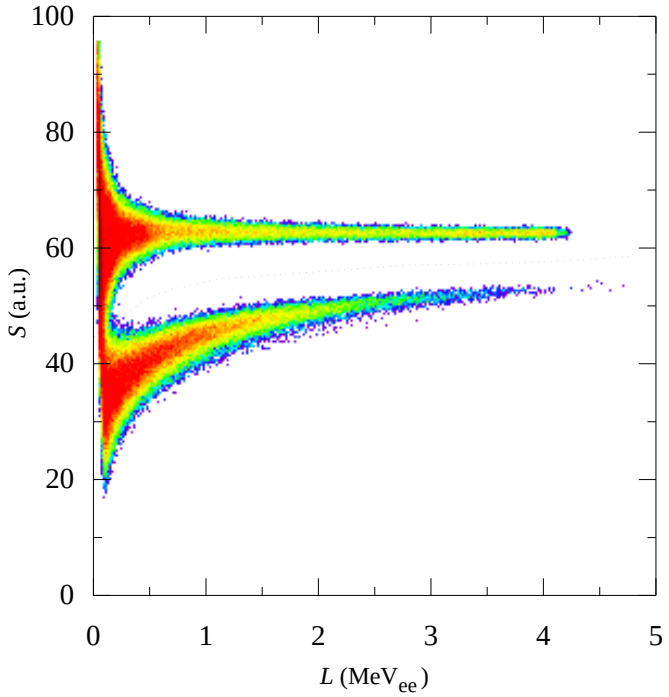

FIGURE 3.10: Counts as a function of light output parameter L and pulse shape parameter S for the EJ301-based detector when exposed to neutrons and gamma-rays from the Am-Be source. Loci associated with Compton scattered electrons (e) and recoiling protons (p) are indicated. The dotted line indicates the cut used to separate neutron and gamma-ray events.

and 2.5 MeV for D-T and D-D generators respectively).

D-T neutron generators operate by accelerating deuterons into a target loaded with tritium, resulting in a fusion reaction:

$$^{2}\mathrm{H} + {}^{3}\mathrm{H} \rightarrow {}^{4}\mathrm{He} + \mathrm{n}, \tag{3.6}$$

with a Q-value of 17.6 MeV. Neutrons produced by this reaction have an energy of approximately 14.1 MeV, and are emitted isotropically. Neutron emission can be pulsed by controlling the accelerator voltage.

A Thermo Scientific MP320 D-T neutron generator [104] was utilised for detector characterisation. The MP320 has a maximum accelerator voltage of 95 kV, producing up to 10^8 neutrons/s in a continuous mode, or pulse rates between 250 Hz and 20 kHz. The D-T generator was housed in a $3 \times 3 \times 2$ m^3 cave constructed from polyethylene bricks. Detectors were placed approximately 30 cm from the point of emission. In addition to 14.1 MeV neutrons, gamma-rays are produced by the interactions of emitted

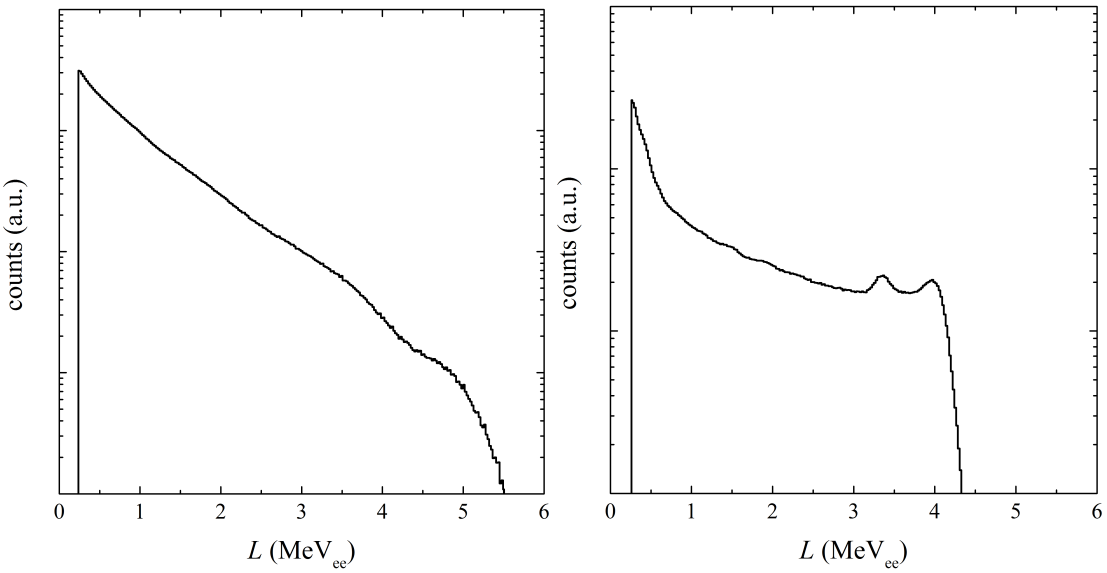

FIGURE 3.11: Light output spectra of (a) neutrons and (b) gamma-rays from the Am-Be source incident on an EJ301-based detector. The Compton edge and single escape peak of the 4.44 MeV gamma-ray can be seen in (b) at 4.20 $\mathrm{MeV_{ee}}$ and 3.42 $\mathrm{MeV_{ee}}$ respectively.

neutrons with the surrounding material.

Figure 3.12 shows the distribution of events as a function of light output parameter L and pulse shape parameter S, for neutrons and (secondary) gamma-rays from the D-T generator incident on the EJ301-based detector. In addition to the well-separated loci of Compton scattered electrons (e) and recoiling protons (p) from n-p scattering, a small locus of alpha-particles (α) is visible at low L, due to inelastic neutron interactions with ^{12}C in the detector.

The dotted line shows a cut used to separate events associated with neutrons from those associated with gamma-rays. The projections of the neutron and gamma-ray selections onto the L-axis are shown in Figures 3.13 (a) and (b) respectively. The position of the proton recoil edge, shown at approximately 9 $\mathrm{MeV_{ee}}$ in Figure 3.13 (a) is significantly lower than the incident neutron energy, due to the reduced light output of scattered protons when compared to electrons. Gamma-ray events are primarily from the detection of 4.43 MeV and 2.23 MeV gamma-rays produced respectively by $^{12}\mathrm{C(n, n')}$ and $^{1}\mathrm{H(n, \gamma)d}$ interactions in the surrounding polyethylene, resulting in the Compton edges of 4.20 $\mathrm{MeV_{ee}}$ and 2.00 $\mathrm{MeV_{ee}}$ visible in Figure 13 (b).

The charge comparison, zero-crossing and linear filter algorithms were compared

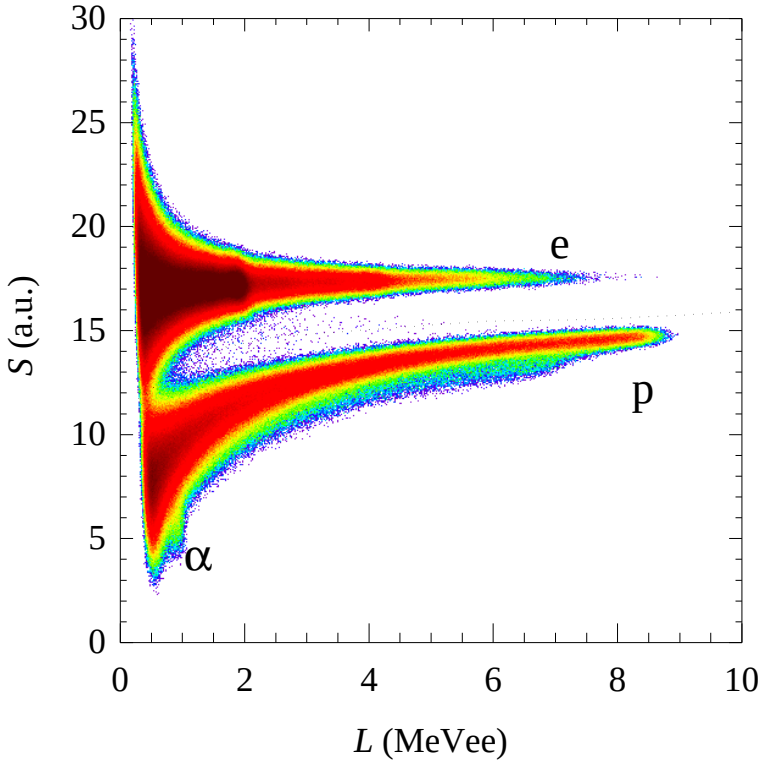

FIGURE 3.12: Counts as a function of light output parameter L and pulse shape parameter S for the EJ301-based detector when exposed to neutrons and gamma-rays from the D-T generator. Loci associated with Compton scattered electrons (e), recoiling protons (p) and alpha-particles (α) are indicated. The dotted line indicates the cut used to separate neutron and gamma-ray events.

by calculating FoMs over a range of L from data shown in Figure 3.12. A number of narrow regions of L were selected, with the data from each selection projected onto the S axis, and fitted to the sum of two Gaussians. The FoM for each selection was then calculated from the corresponding fit parameters. This process was included in QtDAQ as an automated procedure, as the evaluation of FoMs across a range of L was frequently used to optimise detector and DAQ setups.

Figure 3.14 (a) shows FoM as a function of L for each algorithm. In the case of the charge comparison algorithm, it was found that a value of $t_S = 31.5$ ns provided optimal separation at 2 MeV_{ee} , and this value was used across the light output range. The FoMs from all three algorithms follow a similar trend, with FoM improving and converging with increasing L. This is primarily due to the improved signal-to-noise ratio as the number of photoelectrons increases with L. At low L, the linear filter algorithm produces a better FoM over the other two approaches, while this difference

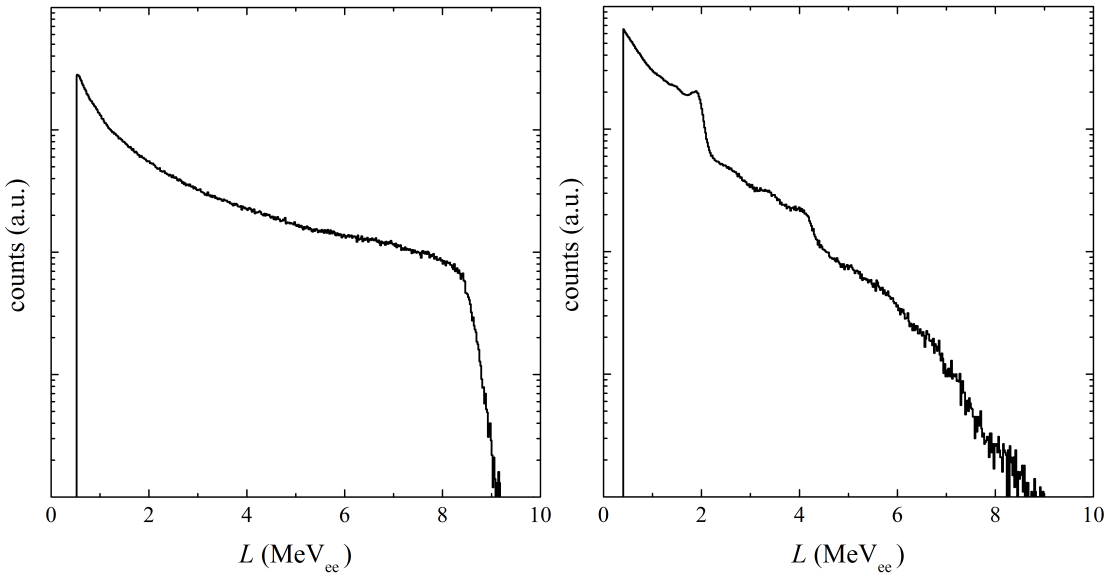

FIGURE 3.13: Light output spectra of (a) neutrons and (b) gamma-rays from the D-T generator incident on an EJ301-based detector. The proton recoil edge can be seen in (b) at approximately 9 $\mathrm{MeV_{ee}}$. The Compton edges of the 2.23 MeV and 4.44 MeV gamma-ray can be seen in (b) at 2.00 $\mathrm{MeV_{ee}}$ and 4.20 $\mathrm{MeV_{ee}}$.

is negligible at higher L.

In order to investigate the effect of integration parameters in the charge comparison algorithm, a MATLAB script was created to repeat the analysis process while varying the short integration duration t_S across a wide range. Figure 3.14 (b) shows FoM for the charge comparison algorithm as a function of t_S for narrow regions of L, centred from $L = 1$ $\mathrm{MeV_{ee}}$ to $L = 6$ $\mathrm{MeV_{ee}}$ in 1 $\mathrm{MeV_{ee}}$ intervals. Figure 3.15 (a) shows the optimal integration duration t_{opt}, as function of L. The dependence of t_{opt} on L is due to variations in the pulse shape as a function of L, as can be seen by the bending of the proton locus in Figure 3.12. Further optimisation of the FoM can be achieved by utilising a varying integration duration $t_S = t_{\mathrm{opt}}(L)$. As shown in Figure 3.15 (b), the effect of this optimisation is small over the light output range used.

3.4.4 iThemba LABS neutron facility

The iThemba Laboratory for Accelerator-Based Sciences (LABS) provides facilities for fundamental and applied research using particle beams. One such facility is the separated sector cyclotron (SSC), which accelerates protons in the energy range between 20 MeV and 200 MeV. The $^{7}\mathrm{Li(p,n)}^{7}\mathrm{Be}$ is employed to produce neutrons beams with a

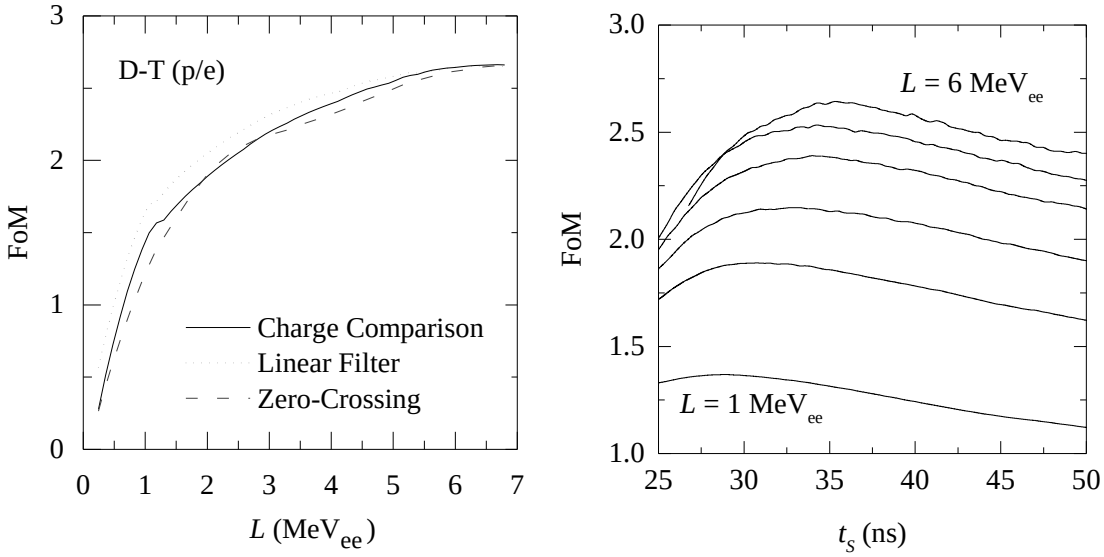

FIGURE 3.14: (a) Figure of merit versus L for events from the D-T generator, showing neutron/gamma-ray separation using various algorithms. (b) Figure of merit versus short integration duration t_S for the charge comparison algorithm, shown for narrow regions of L, centred from $L = 1$ MeV$_{ee}$ to $L = 6$ MeV$_{ee}$ in 1 MeV$_{ee}$ intervals.

strongly forward-peaked quasi-monoenergetic component [86] through the bombardment of a natural lithium target. Figure 3.16 shows a schematic of the iThemba LABS neutron beam facility, with typical detector placement at 0° and 16° with respect to the incoming proton beam direction. A 2 m thick steel 5 × 5 cm^2 collimator shapes the neutron beam. The collimator is lined with borated wax and polyethylene, in order to moderate and capture neutrons.

Breakup reactions in the the lithium target result in a low energy tail to the monoenergetic peak, with a nearly isotropic distribution. Measurements taken at the 16 ° angle can therefore be used to directly measure the isolated breakup reactions, without the presence of the monoenergetic peak. A cleaning magnet deflects protons into a beam stop, equipped with a Faraday cup for beam current measurements. Neutron flight path lengths between 4 m and 11 m are supported. The facility has been widely used for detector development [84], [85], as well as meteorological applications [105], [106].

A beam pulse selector can suppress a chosen fraction of proton bunches, in order to increase the time interval between successive pulses, allowing for time-of-flight (ToF) measurements to be utilised to determine neutron energy. Typical time intervals

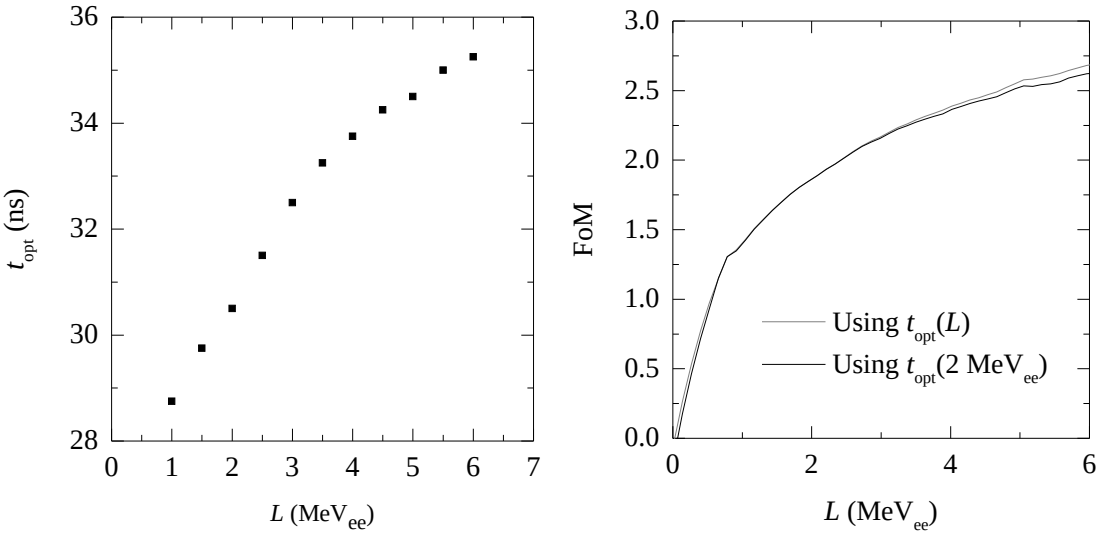

FIGURE 3.15: (a) Optimal integration duration t_{opt}, as function of L. (b) Figure of merit versus L, with and without a varying integration duration.

between pulses of 400 ns are used. Typical beam currents for 100 MeV protons are about 5 mA in unselected mode, dropping to 500 nA with a pulse selector frequency of 2.5 MHz.

Three incident proton energies (42 MeV, 62 MeV and 100 MeV) were used in the measurements described below, with a 3 mm Li target used for 42 MeV protons and an 8 mm Li target used for 62 MeV and 100 MeV protons. An EJ301-based detector was placed a distance of 6.00 m from the target, at an angle of 0°. The charge integration parameter Q_L was calculated by integrating the digitised signal over a 300 ns interval, chosen in order to capture as much of the entire signal as possible, while still avoiding saturation of the available output transfer rate of the VX1761 digitiser. Gamma-ray calibration sources were used for scaling Q_L to light output parameter L. The relationship between Q_L and L was found to be linear over the energy range of the calibration sources, and was assumed to be linear over the energy range of the measurements.

A time-of-flight parameter T can be defined as the difference between t_{Start} of the detector event pulse and t_{Start} of a reference pulse associated with the preceding proton beam bunch, provided by the pulse selector and digitised in a secondary channel.

Figure 3.17 shows the distribution of events as a function of L and T for measurements made using a 62 MeV proton beam irradiating the lithium target. The sharp

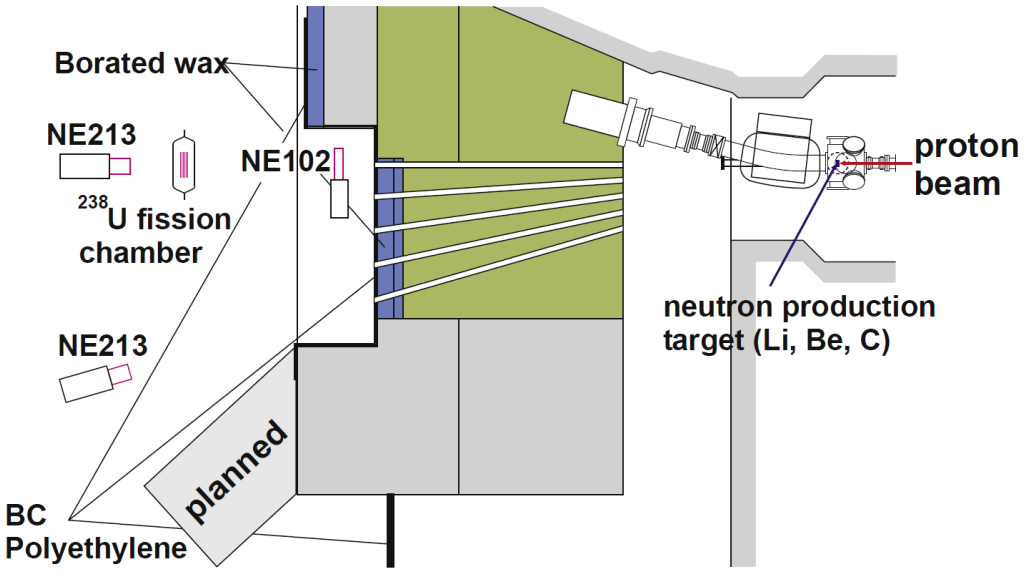

FIGURE 3.16: Sketch of the iThemba LABS neutron beam facility, with detectors placed at 0° and 16°. Figure reproduced from Mosconi et al.[86].

peak at $T = 92$ ns (FWHM < 1.3 ns) is associated with gamma-rays produced in the lithum target, while the uniform time-independent distrubition with $L < 8$ MeV$_{ee}$ is associated with background gamma-rays in the experimental hall. The distribution at $T = 129$ ns is associated with direct reaction transitions mainly to the ground state of ^{7}Be, and to the unresolved first excited state [106]. The continuum at lower enegies is associated primarily with the three-body break up process ^{7}Li(p,n^{3}He)α [106]. The dashed line shows a curve of the form $L \sim 1/T^2$, indicating the correlation between maximum L and incident neutron energy.

Figure 3.18 shows distributions of events as a function of L and S, produced for runs with proton beams of energy (a) 42 MeV, (b) 62 MeV and (c) 100 MeV. Loci attributed to different particles released by n-p elastic scattering or by n-C interactions in the scintillator are identified as follows in Figure 3.18(b): protons (p); deuterons (d); tritons (t) and alpha-particles (α). Due to the dependence of pulse shape on energy loss dE/dx, these loci can be identified in order of increasing dE/dx [12]. Events in the region between loci t and α can be attributed to ^{3}He ions, or to the simultaneous detection of two or more charged particles. A locus (e) is associated with recoiling electrons (due to Compton scattering of gamma-rays), and locus (ep) with charged

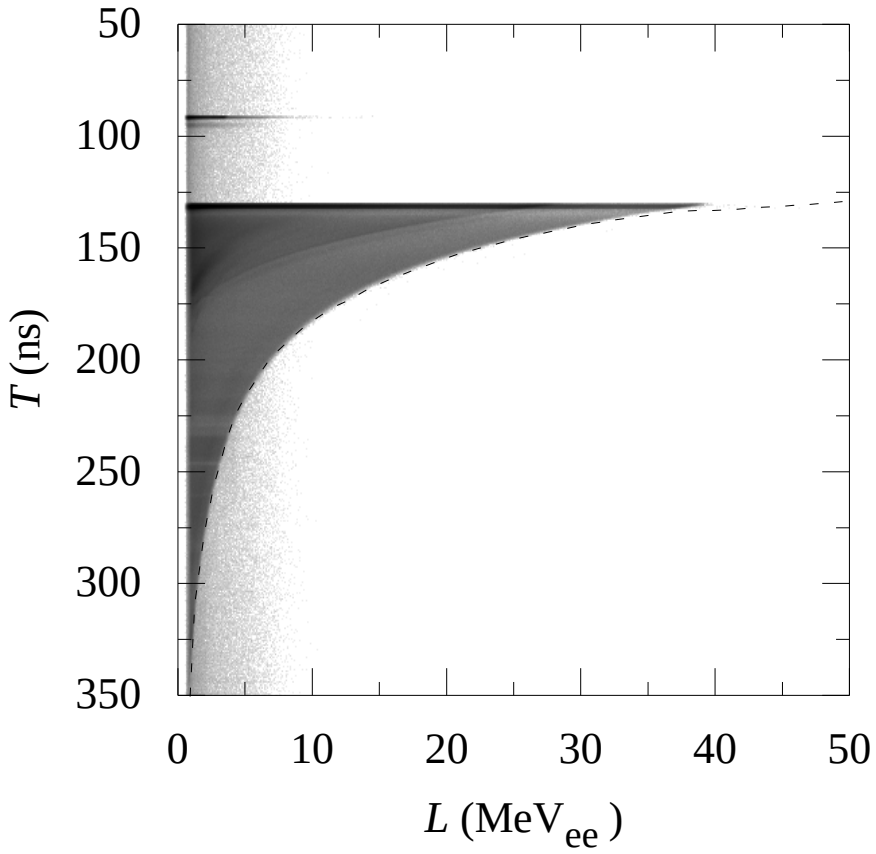

FIGURE 3.17: Counts as a function of L and time-of-flight parameter T for an EJ301-based detector from measurements made using a 62 MeV proton beam irradiating an 8 mm natural lithium target. The detector was placed a distance of 6.00 m from the target. The dashed line shows a curve of the form $L \sim 1/T^2$, indicating the correlation between maximum L and incident neutron energy.

particles (mainly protons) which escape from the 5.1 cm long detector before depositing their full energy in the scintillator.

The ep and e loci merge at lower L, since escaping charged particles do not deposit their Bragg peak, resulting in a significant reduction in the proportion of Q_L to Q_S. The higher proportion of escaping protons is clearly evident at 100 MeV, where the range of a 100 MeV proton in EJ301 is 8.7 cm [107]. The dotted lines indicate the cuts used to exclude events associate with gamma-rays from subsequent plots. The dashed line in Figure 3.18(b) indicates a cut selecting events in the range $L = 19$ MeV_{ee} to $L = 21$ MeV_{ee} . These events are projected onto the S-axis in Figure 3.19. The distributions for protons, deuterons, tritons and escaping protons are easily discernible.

Figure 3.20 shows light output spectra for the three incident proton energies, after

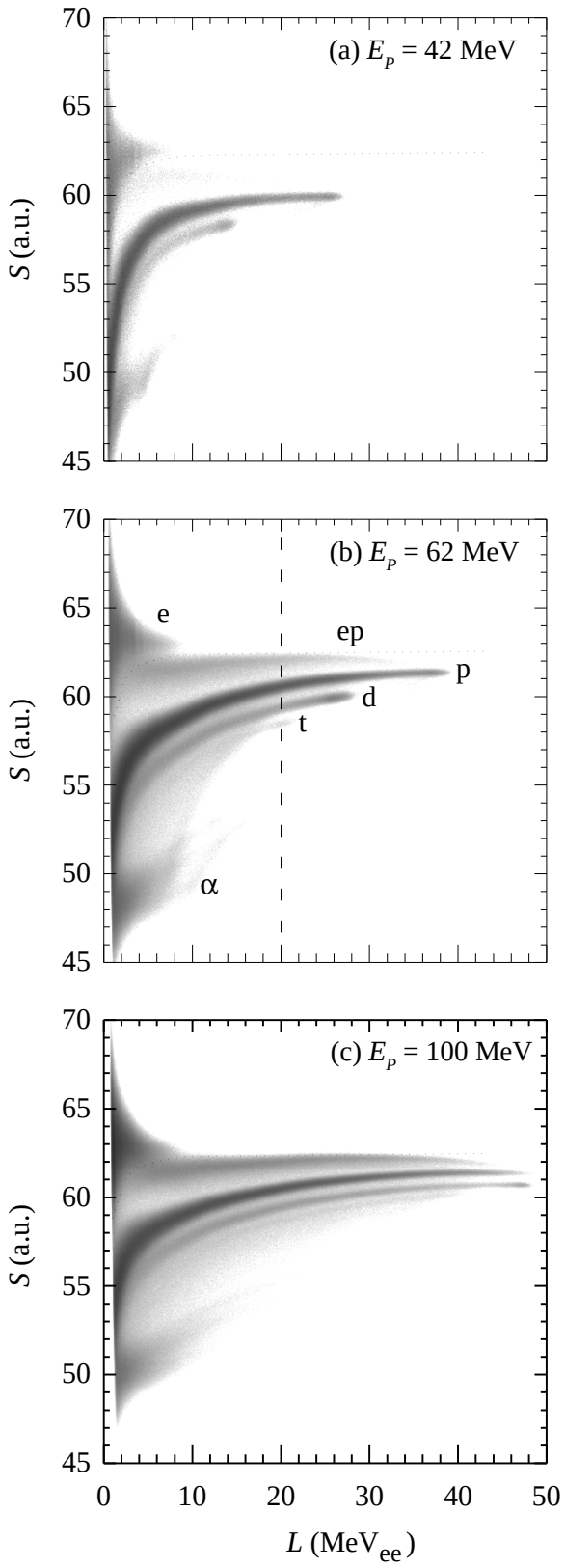

FIGURE 3.18: Counts as a function of light output parameter L and pulse shape parameter S for an EJ301-based detector when exposed to neutrons and gamma-rays produced by the irradiation of a lithium target by proton beams of energy (a) 42 MeV, (b) 62 MeV and (c) 100 MeV. Loci associated with recoiling electrons (e), protons (p), escaping protons (ep), deuterons (d), tritons (t) and alpha-particles (α) are indicated. The dotted lines indicate the cuts used to separate neutron and gamma-ray events, while the dashed lines show the cut used to select events in the range $L = 19$ to $L = 21$ MeV$_{ee}$.

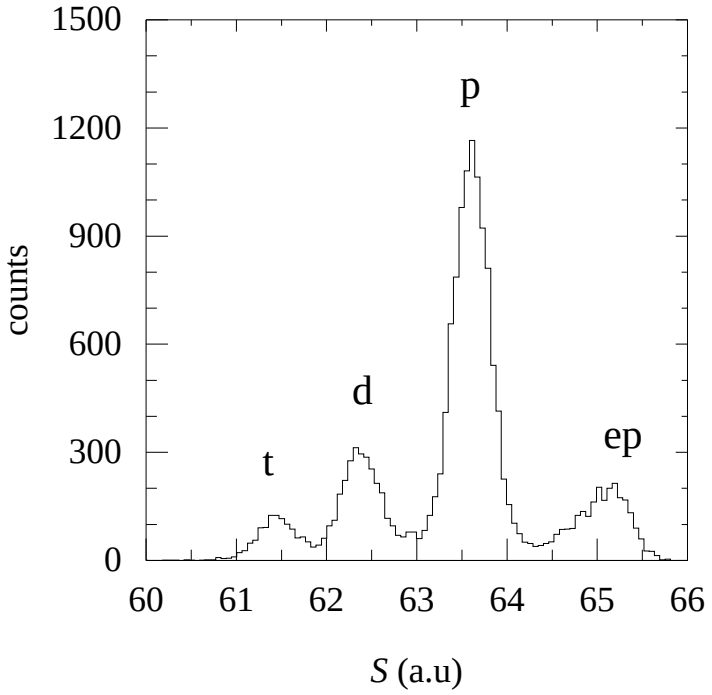

FIGURE 3.19: Counts versus pulse shape parameter S for events in the range of L=19-21 MeV_{ee} from a run with the 62 MeV proton beam. The labels indicate event distributions associated with recoiling protons (p), deuterons (d) and tritons (t) and protons which escape the detector (ep) before depositing their full energy.

gamma-ray events were excluded, together with the spectral components associated with the recoil of protons, deuterons and alpha-particles, selected by PSD according to the loci shown in Figure 3.18.

Flight time for a neutron is given by

$$t_{\mathrm{n}} = \frac{s}{\beta c}, \tag{3.7}$$

where s is the path length and c is the speed of light and $\beta = v/c$ is the speed of the neutron relative to the speed of light. Flight time for gamma-rays is given by $t_\gamma = s/c$. One can write β in terms of the difference between t_{n} and t_γ:

$$\beta = \frac{s}{c\Delta t + s}, \tag{3.8}$$

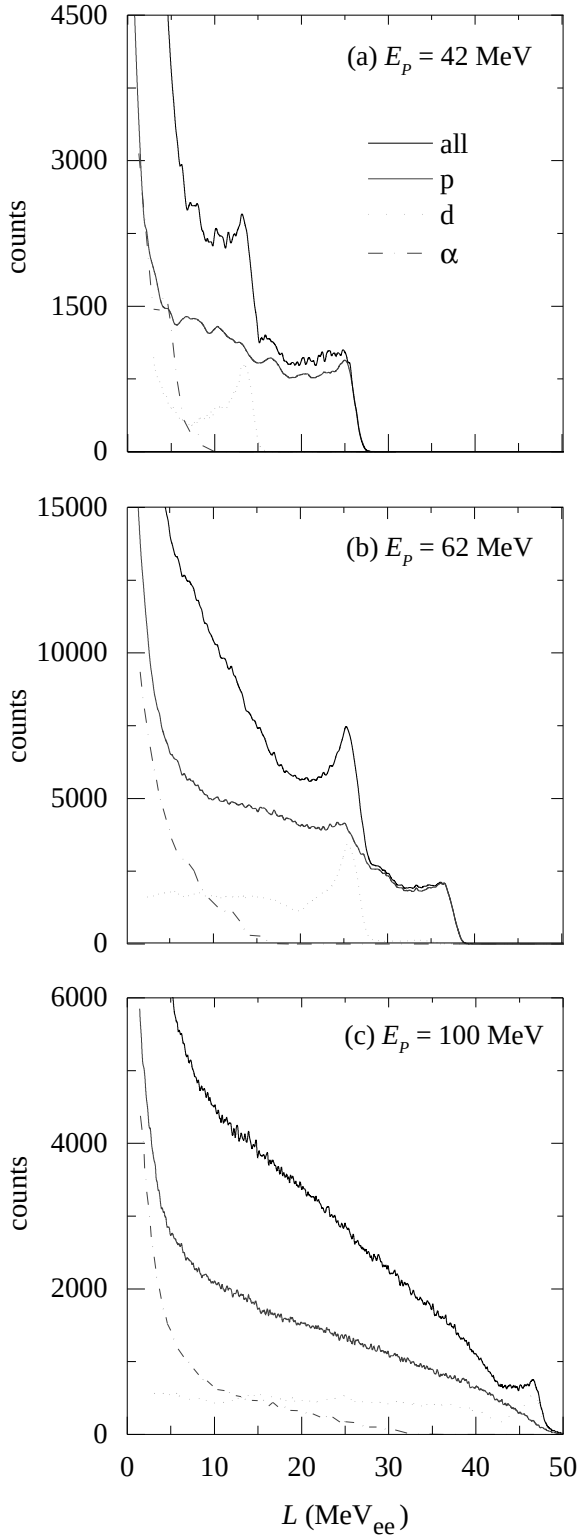

FIGURE 3.20: Light output spectra for events from runs with proton beams of energies (a) 42 MeV, (b) 62 MeV and (c) 100 MeV. The components associated with the recoil of protons, deuterons and alpha-particles were selected by PSD.

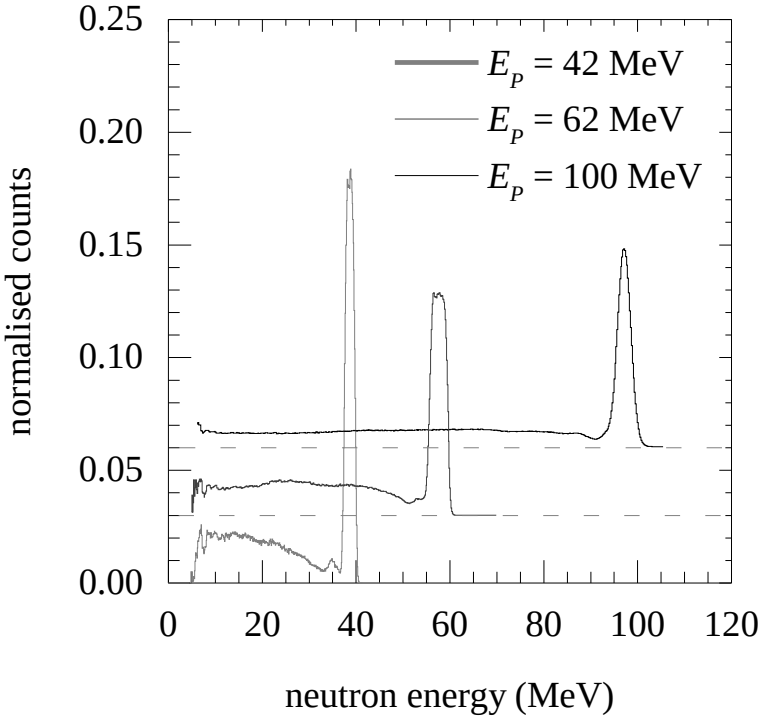

FIGURE 3.21: Neutron energy spectra determined via time of flight for runs with proton beams of energies 42, 62 and 100 MeV irradiating a lithium target. The spectra have been normalised to unity after being corrected for detector efficiency.

where $\Delta t = t_{\mathrm{n}} - t_{\gamma}$. The kinetic energy of an incident neutron is related to β as follows:

$$E_k = m_0 c^2 \left(\frac{1}{\sqrt{1-\beta^2}} - 1 \right), \tag{3.9}$$

where m_0 is the neutron rest mass energy (939.57 MeV). Neutron energy spectra can therefore be determined from time-of-flight measurements, and are showin in Figure 3.21 normalised to unity, after correcting the measurements for the efficiency of the detector. Each channel of the spectra above 10 MeV agrees within 5% of previous measurements at iThemba LABS using traditional analogue electronics [105]. The width of the quasi-monoenergetic neutron peak is dominated by contributions from the energy loss of the proton beam in the lithium target and the intrinsic time resolution of the EJ301 scintillator, rather than the timing resolution of the digital data acquisition system.

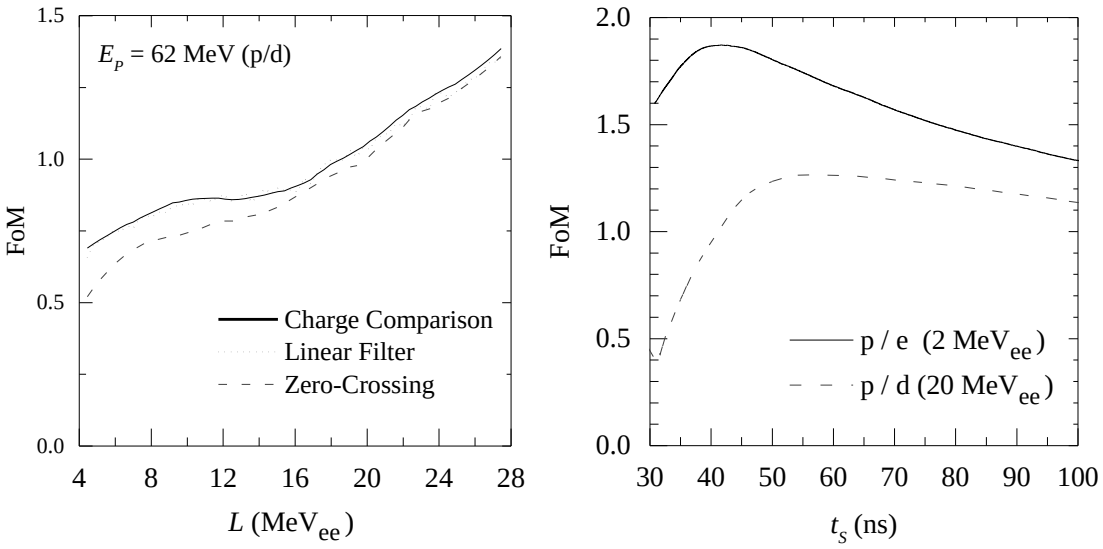

FIGURE 3.22: (a) Figure of merit versus L for events from a run with the 62 MeV$_{ee}$ proton beam, showing recoil proton/deuteron separation using various algorithms. (b) Figure of merit versus short integration duration t_S for events from runs with the D-T generator (neutron/gamma-ray separation in the range L=1.9-2.1 MeV$_{ee}$) and the 62 MeV proton beam (recoil proton/deuteron separation in the range L=19-21 MeV$_{ee}$).

Figure 3.22(a) shows FoM for recoil proton and deuteron loci separation as a function of L for the 62 MeV proton beam, as calculated using the charge comparison, zero-crossing and linear filter algorithms described in Section 3.3. Separation between the proton and deuteron loci improves with increasing L due higher measured photon counts. However, the FoM values for the p-d data are consistently lower than those for p-e data derived from D-T measurements (see Figure 3.14), as governed by the specific light output functions for electrons and much heavier charged particles, which produce less distinctive responses.

Figure 3.22(b) shows FoM as a function of t_S for the charge comparison algorithm, measuring p-e discrimination at L=2 MeV$_{ee}$ and p-d discrimination at L=20 MeV$_{ee}$. For measurements with the D-T generator (and similarly for the Am-Be source) the optimal value of t_S is 40 ns, while for p-d discrimination at higher L, the optimal value of t_S is about 50 ns.

3.5 Discussion

Results shown in this chapter indicate that the digital DAQ is capable of performing efficient PSD across a wide energy range. While the linear filter method produced slightly better results at lower energies, the charge comparison method is favoured in following chapters, due to its simplicity. However, a careful choice of the integration parameters has been for future measurements, depending on the scintillator type and energy range of interest.

Chapter 4

Characterisation of EJ299-33 scintillator

The development of EJ299-33, a plastic scintillator which displays PSD characteristics, has a number of potential applications across a wide energy range. The high level of PPO loading in EJ299-33 [13] introduces differences between the hydrogen and carbon densities of EJ299-33 and those of standard liquid scintillators. While the light output and pulse shape discrimination behaviour of liquid scintillators, such as EJ301, are well understood for incident neutron energies of up to and above 100 MeV [108], [109], existing measurements of light output and PSD of EJ299-33 are limited to below 20 MeV [35], [38], [39]. This chapter focuses on the extension of these characterisations up to 100 MeV, an investigation into the pulse shapes observed in EJ299-33 based detectors, and the implementation of a simulation of an EJ299-33 based detector using Geant4.

In order to characterise the behaviour of EJ299-33 across a wide energy range, measurements were taken using the iThemba LABS neutron facility (See Section 3.4.4), with a proton beam energy of 140 MeV, as well as an Am-Be radio-isotopic source (See Section 3.4.2).

For each recorded event, Q_L was calculated by integrating the digitised signal over a 300 ns time (t_L), starting from t_{Start}. Measurements of the Compton edges of gamma-rays from ^{22}Na, ^{137}Cs and Am-Be radio-isotopic sources were used for scaling Q_L to L in MeV$_{\mathrm{ee}}$. Neutrons from the Am-Be source were excluded from calibration by use of PSD. Compton edge positions were determined by differentiating the light output spectra and performing a Gaussian fit on the result (See Section 3.4.1).

The relationship between Q_L and L was found to be linear over the energy range

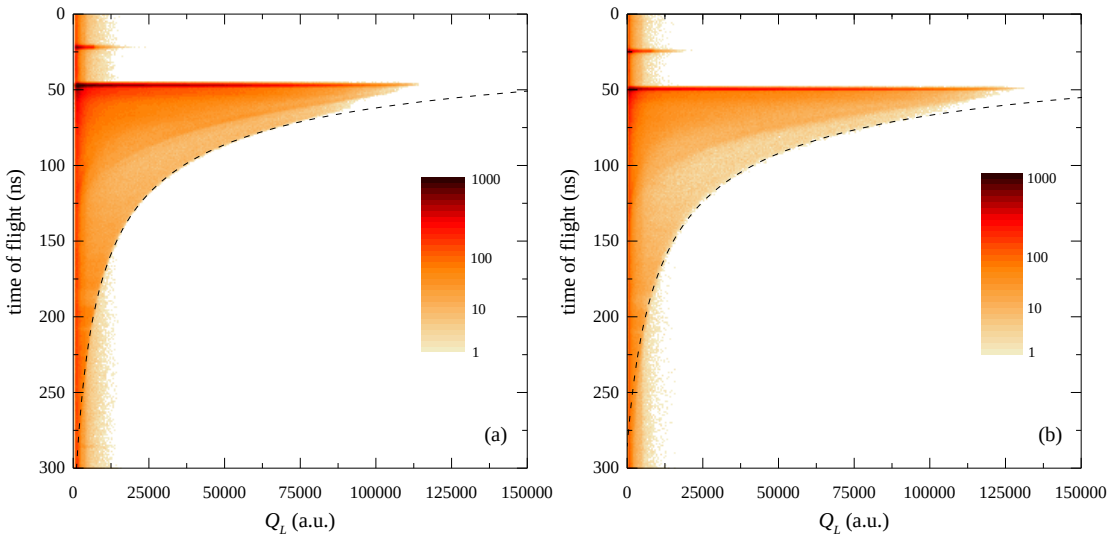

FIGURE 4.1: Counts as a function of Q_L and time-of-flight parameter T for (a) EJ301 and (b) EJ299-33 from measurements made using a 140 MeV proton beam irradiating an 8 mm Li target, at a distance of 6.00 m from the target. The dashed line shows a curve of the form $Q_L \sim 1/T^2$, indicating the correlation between maximum Q_L and neutron energy.

of the calibration sources for both detectors. However, a quadratic deviation from this relationship was observed for $L > 20$ MeV_{ee} , attributed to space charge saturation in the PMT. As the linearity of EJ301 is well established at higher energies [12], [108], [109], a quadratic correction was applied to deal with this deviation. The same correction was applied to both detectors.

4.1 Timing, light output and pulse shape discrimination

4.1.1 Measurements using 140 MeV proton beam

Figure 4.1 shows the distribution of events as a function of Q_L and T for measurements made using (a) EJ301 and (b) EJ299-33. The sharp peaks at $T = 25$ ns (FWHM < 1.3 ns) are associated with gamma-rays produced in the Li target, while the uniform time-independent distributions with $Q_L < 12500$ are associated with background gamma-rays in the experimental hall. The distributions at $T = 50$ ns are associated with direct reaction transitions. The deviation of the data from the dashed curve at higher Q_L is an indication of space charge saturation in the PMT, as well as the large fraction of escaping protons.

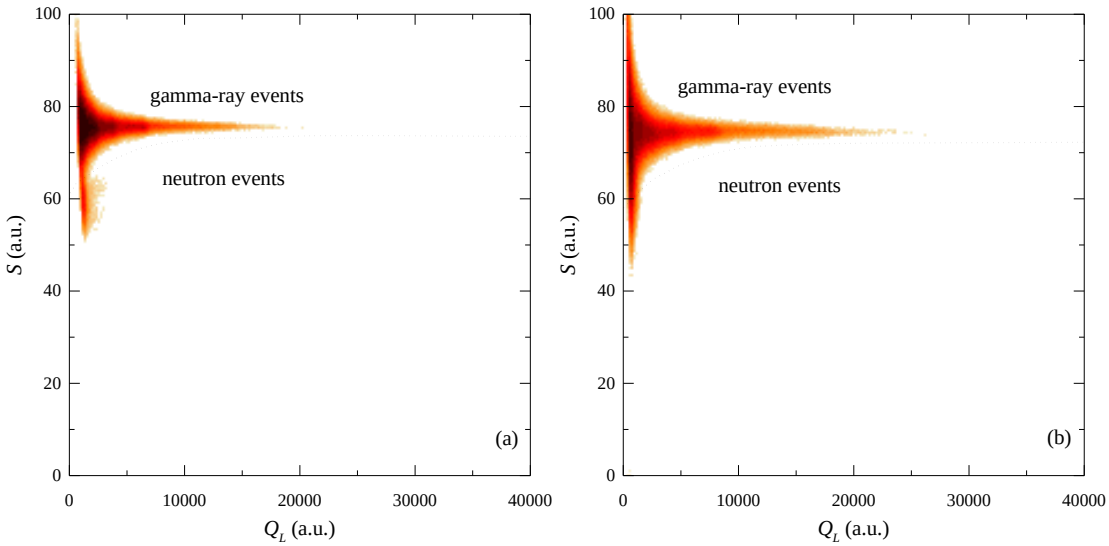

FIGURE 4.2: Counts as a function of Q_L and pulse shape parameter S for (a) EJ301 and (b) EJ299-33 when exposed to gamma-rays produced by the irradiation of a Li target by a proton beam of energy 140 MeV. Neutron events have been excluded by a time-of-flight cut. The dotted curve indicates the cut used to separate neutron and gamma-ray events via PSD in subsequent plots.

Figure 4.2 shows the distribution of events as a function of Q_L and S for measurements made using (a) EJ301 and (b) EJ299-33, selecting events with $T < 40$ ns, in order to primarily show the gamma-ray distribution. The dotted curve indicates the cut used to separate events associated with the interactions of neutrons and gamma-rays in the detector. This cut was chosen by eye so as to exclude the majority of gamma-ray events.

Figure 4.3 shows neutron energy spectra, as determined via time-of-flight, after the exclusion of gamma-ray events using the cut shown in Figure 4.2. The spectra in Figure 4.3 have been normalised to the same total number of counts. Differences in the spectra for energies below 40 MeV are due to the sensitivity of the spectrum to the cut used for pulse shape discrimination for the EJ299-33 and EJ301 detectors. The small variation in peak height at 140 MeV can be attributed to the slightly degraded timing resolution of EJ299-33 [34]. The spectra match to within 1% across the remainder of the energy range, showing very similar relative detection efficiency as a function of energy.

In order to determine the relationship between light output and energy deposited by recoiling protons, events were separated into energy bins of 500 keV width, based on time-of-flight measurements. A light output spectrum for neutron events in each energy bin was produced. The edge of each spectrum then represents the light output

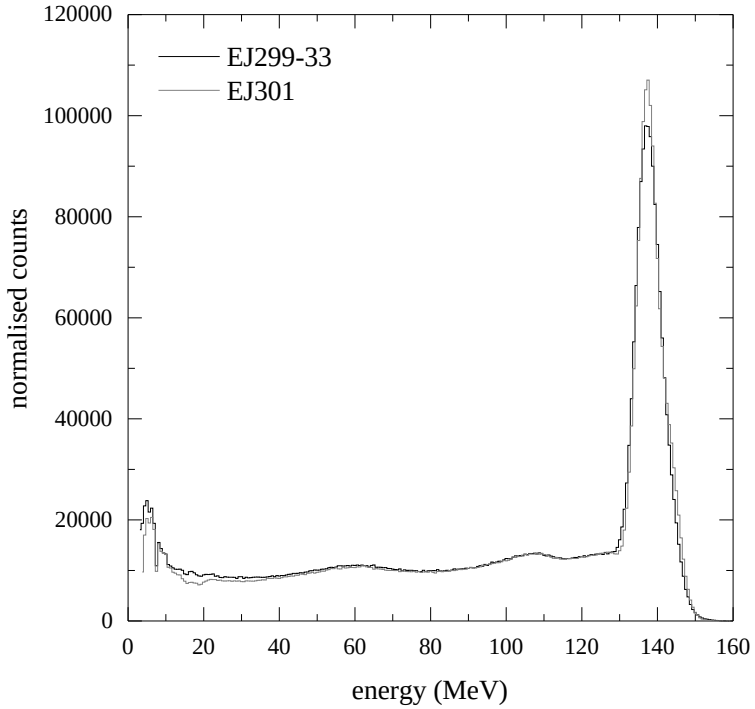

FIGURE 4.3: Neutron energy spectra determined via time-of-flight for a measurements made using a 140 MeV proton beam irradiation an 8 mm Li target. Gamma-ray events have been excluded by the cut shown in Figure 4.2. The spectra have been normalised to the same total number of counts.

of a recoil proton with the same energy as the incident neutron. These edge positions were determined in a consistient manner by differentiating the light output spectra and performing a Gaussian fit on the result. Figure 4.4 shows light output parameter L against proton recoil energy E_P, for EJ301 and EJ299-33. The light output for EJ299-33 is lower than that of EJ301, and agrees to within 5% of previous measurements at lower energies [39].

Figure 4.5 shows the distribution of events as a function of L and S for measurements made using (a) EJ301 and (b) EJ299-33, selecting events across a 6 MeV energy range via time-of-flight, centred at 50 MeV. Loci attributed to particles released by n-p elastic scattering or by n-C interactions in the scintillator are identified as: protons (p); deuterons (d); tritons (t) and alpha particles (α). Locus (e) is associated with recoiling electrons from gamma-ray interactions, and locus (ep) with protons which escape from the detector before depositing their Bragg peak. The (p), (d), (t) and (α) loci in Figure 4.5(a) are clearly resolvable, while the (p), (d) and (t) loci overlap in Figure 4.5(b), due to the limited PSD capability of EJ299-33 [17], [42].

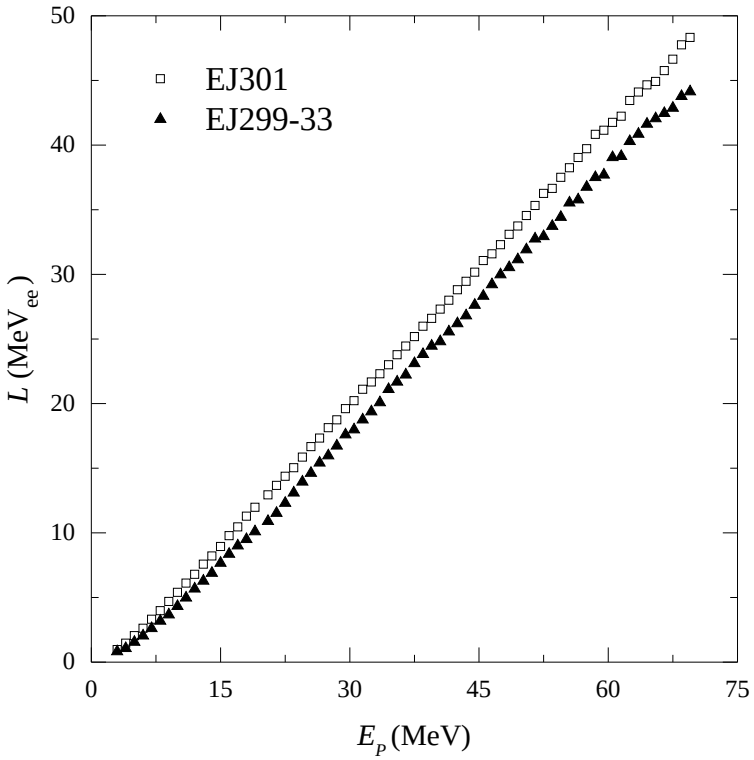

FIGURE 4.4: Light output parameter L against elastic proton recoil energy E_P, determined from time-of-flight for EJ301 and EJ299-33. The error is smaller than the data marker for all measurements.

Figure 4.6 shows light output spectra for neutron energy distributions centred from 10 MeV to 100 MeV. Each distribution consists of a 3 MeV range, selected by time-of-flight cuts. Gamma-ray events have been excluded by the cuts shown in Figure 4.5, and the spectra have been normalised to the same total count. The edges are broadened in the EJ299-33 spectra, due to poorer pulse height resolution.

At 50 MeV, the proton recoil edges for EJ301 and EJ299-33 are visible at approximately 35 MeV$_{ee}$ and 30 MeV$_{ee}$ respectively, while the deuteron edges appear at 22 MeV$_{ee}$ and 20 MeV$_{ee}$ respectively. Above 70 MeV, the proton recoil edge is suppressed, due to the large fraction of protons that escape the detector. The deuteron edge remains discernible up to 100 MeV, due to the significantly shorter range of deuteron in the detector.

4.1.2 Unfolding of light output spectra

The pulse height spectrum unfolding method is widely used as a method for neutron spectrometry, particularly when nanosecond-timing is not available. Unfolding

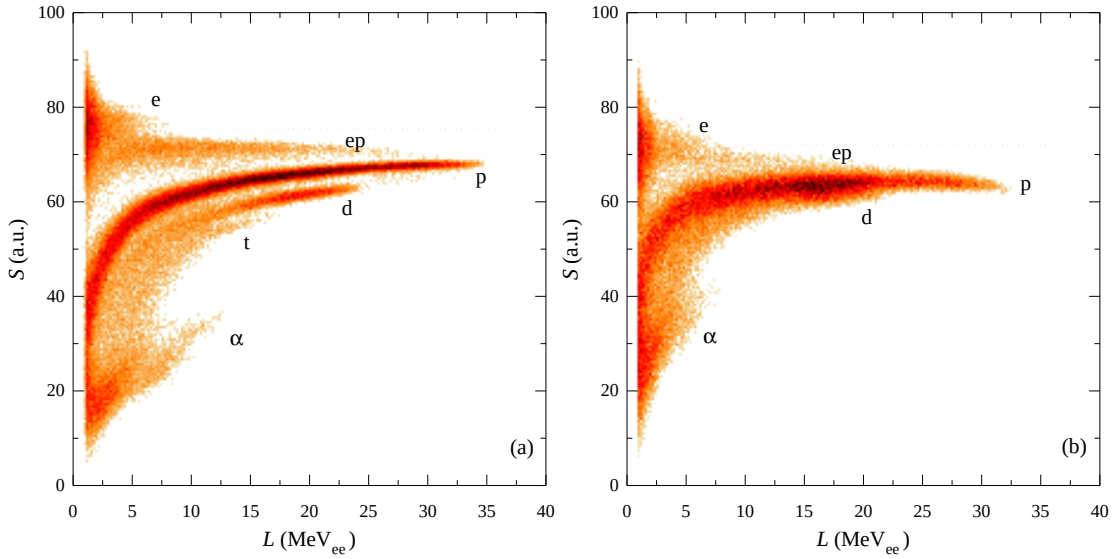

FIGURE 4.5: Counts as a function of light output parameter L and pulse shape parameter S for events in (a) EJ301 and (b) EJ299-33 when exposed to neutrons and gamma-rays produced by the irradiation of a Li target by a proton beam of energy 140 MeV, selecting events with 47.5 $< E <$52.5 MeV by time-of-flight measurements. Loci associated with recoiling electrons (e), protons (p), escaping protons (ep), deuterons (d), tritons (t) and alpha-particles (α) are indicated. The dotted line indicates the cut used to separate neutron and gamma-ray events.

requires a carefully constructed response matrix in order to de-convolute the input light output spectrum. The Monte-Carlo based MIEKE program [110], which is part of the of the HEPRO spectrum unfolding package [21], [111] is used in this section to demonstrate the use of EJ299-33 for neutron spectrometry. MIEKE utilises a Bayesian method, based on the principle of maximum entropy, allowing for a consistent propogation of uncertainties from input light output spectra to outputted energy spectra [112].

In order to assess the capability of EJ299-33 for use as a neutron spectrometer, neutron energy spectrum unfolding was performed using both EJ301 and EJ299-33. The edge of the deuteron locus in Figure 4.5 (a) is sharper than that of the proton locus. As such, improved unfolding could be achieved by considering the deuteron response in isolation [12]. Additionally, the reduced range of deuterons in the scintillator allow for unfolding at higher energies, as fewer deuterons escape the detector. However, the poor separation between proton and deuteron bands in spectra for EJ299-33, as shown in Figure 4.5 (b), makes this infeasible.

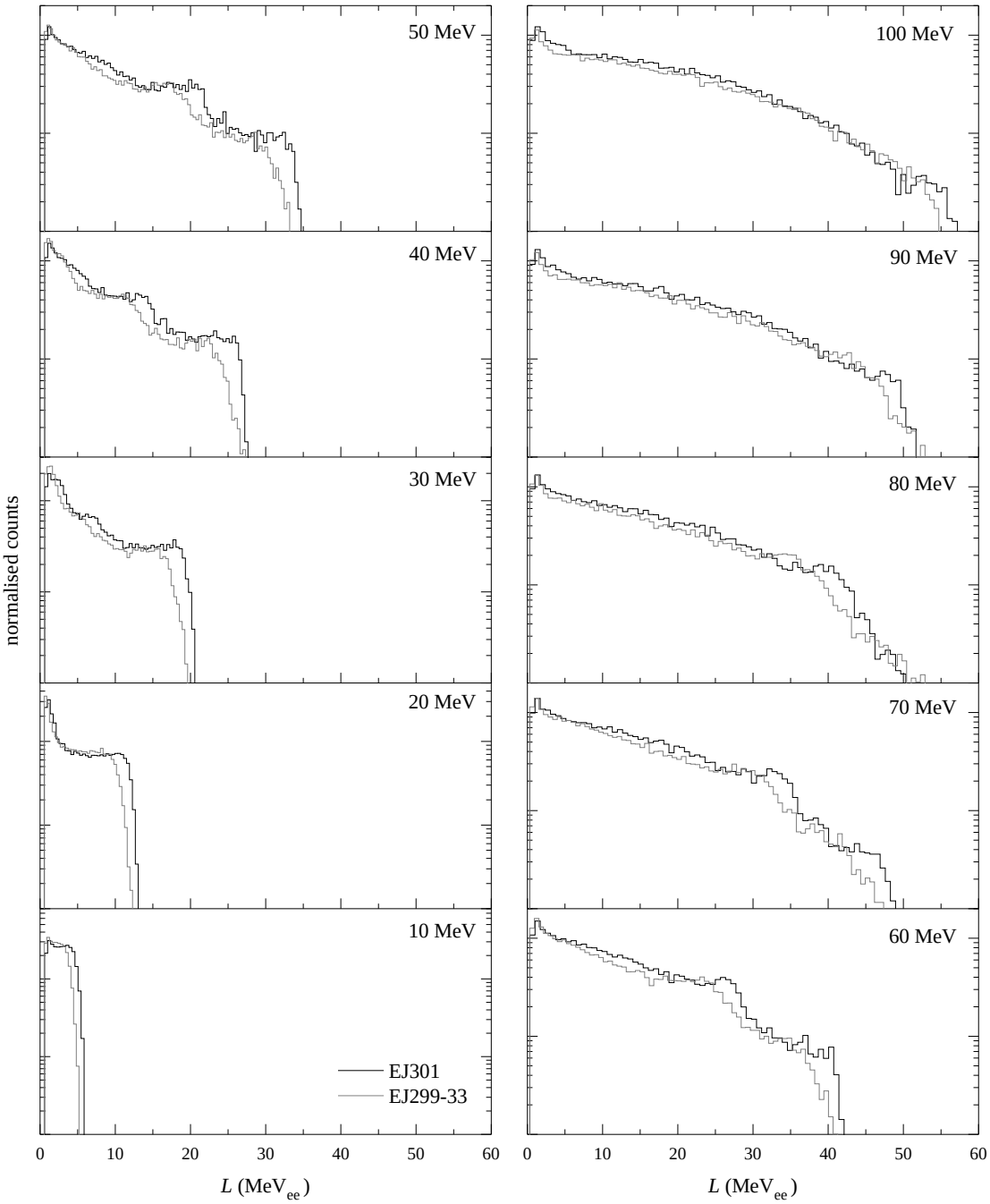

FIGURE 4.6: Light output spectra for various incident neutron energies between 10 and 100 MeV, selected by time-of-flight cuts. Gamma-ray events have been excluded by the cuts shown in Figure 4.5.

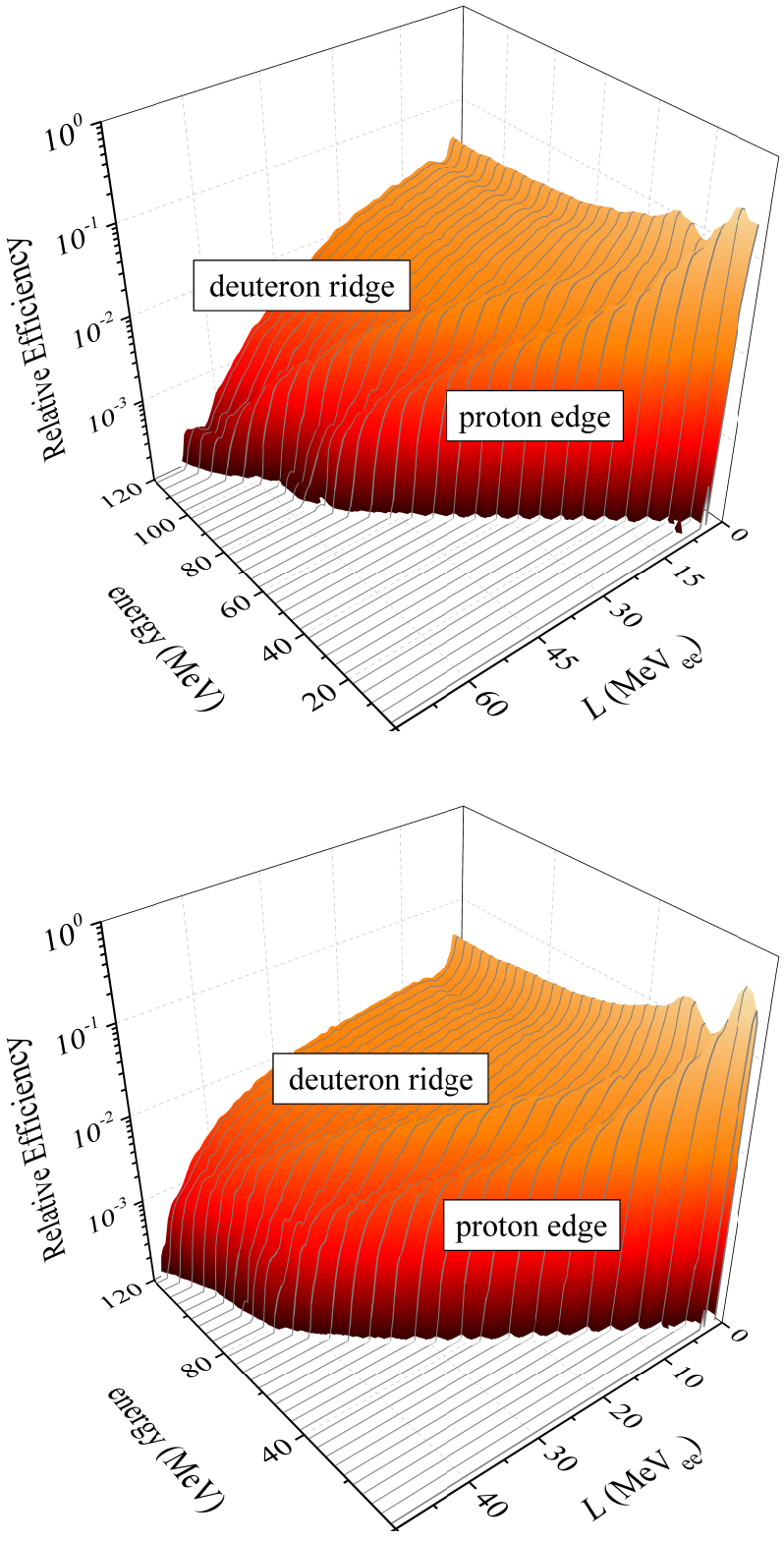

FIGURE 4.7: Response matrices for (top) EJ301 and (bottom) EJ299-33, determined from the energy spectra shown in Figure 4.3.

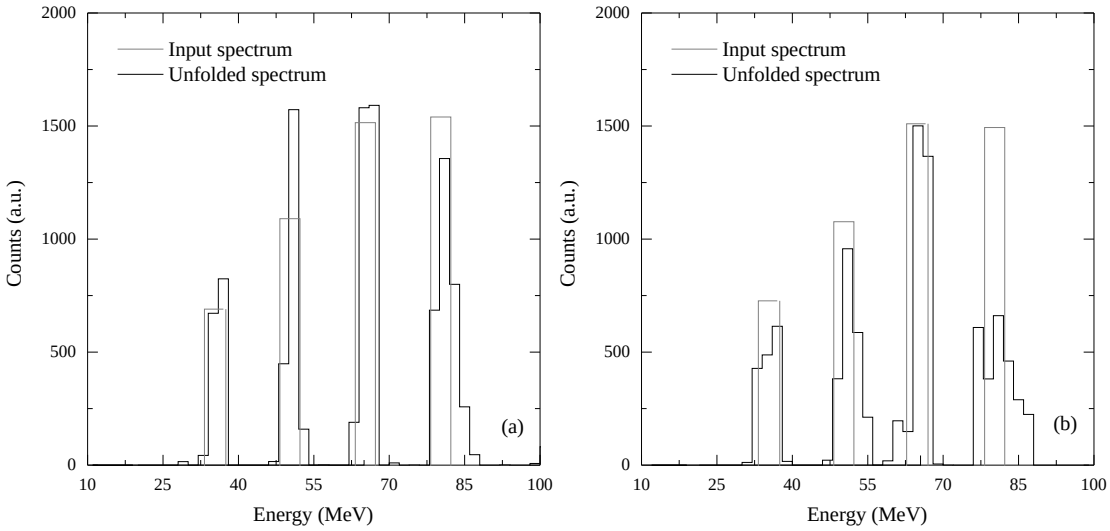

FIGURE 4.8: Unfolded neutron energy spectra for (a) EJ301 and (b) EJ299-33, using an input spectrum consisting of boxcar functions of various heights, centred at 35, 50, 65 and 80 MeV.

A response matrix for neutron energies between 10 and 100 MeV was constructed for each detector from pulse height spectra for energy ranges of width 1 MeV, centred from 10 MeV to 100 MeV, in steps of 2 MeV, and selected using time-of-flight measurements. Figure 4.7 shows counts (normalised to an integral of unity to show relative efficiency of the detector) against incident neutron energy and light output, for EJ301 and EJ299-33 detectors. The bending of the proton recoil edge visible in both plots is due to space charge saturation in the PMT. Both the proton recoil edge and the deuteron "ridge" are far more discernible in the response matrix of EJ301, due to improved pulse height resolution. Above 75 MeV, the proton recoil edge falls away, due to the large fraction of protons escaping the detector.

Pulse height spectra for the unfolding tests were created by applying time-of-flight cuts to an independent dataset, also consisting of a run from the 140 MeV proton beam. In the example shown, the test energy spectra consisted of four boxcar functions of width 4 MeV, centred at 35, 50, 65 and 80 MeV. The pulse height spectra associated with these energy spectra were unfolded using MIEKE.

Figure 4.8 shows the test energy spectra together with the unfolded energy spectra for (a) EJ301 and (b) EJ299-33. The unfolding process reproduces the position of the centre of each boxcar function and the peak is well resolved in each case. The peak

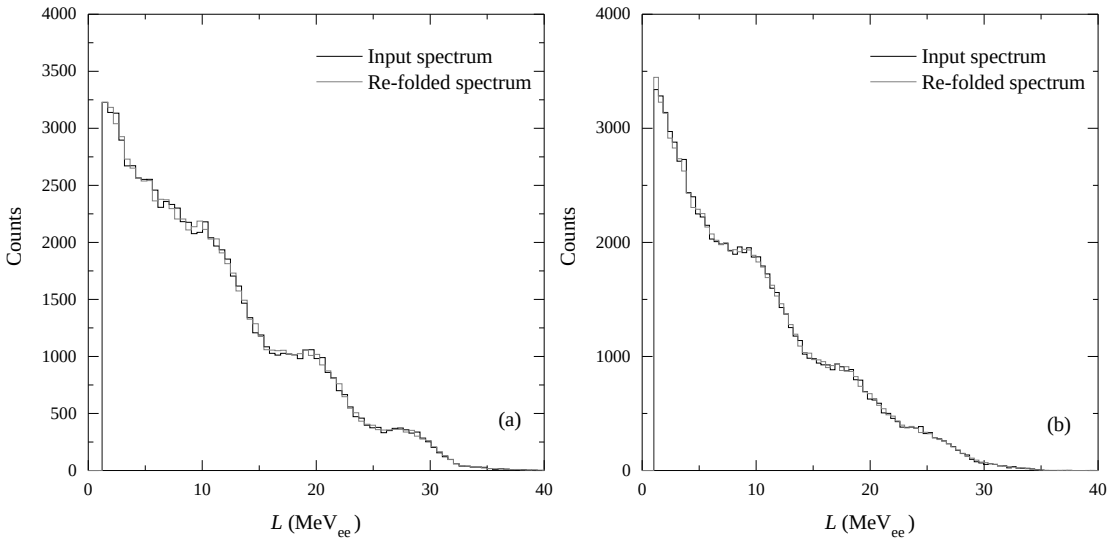

FIGURE 4.9: Re-folded light output spectra for (a) EJ301 and (b) EJ299-33, using the unfolded energy spectra shown in Fig. 4.8.

widths in the EJ299-33 spectrum are broadened in comparison to those of the EJ301 spectrum, as a consequence of the poorer pulse height resolution across the energy range.

The agreement between the unfolded spectrum and corresponding time-of-flight spectrum is better at lower neutron energy than at high energy. A large proportion of neutrons with incident energies above 70 MeV escape the detector before depositing their full energy, leading to the poorer pulse height resolution at higher energies and thus poorer statistical accuracy in the response matrix. This, in combination with the poorer pulse height resolution of EJ299-33, leads to the significant distortion of the unfolded spectrum shown in Figure 4.8 (b) in the 75-100 MeV range.

Figure 4.9 shows the input pulse height spectra together with the re-folded spectra obtained from the fits for (a) EJ301 and (b) EJ299-33. The agreement is excellent in both cases with χ^2/DOF values of 0.981 and 0.980 respectively.

4.1.3 Measurements using Am-Be source

Figure 4.10 shows distributions of events as a function of parameters L and S for events in (a) EJ301 and (b) EJ299-33, when exposed to neutrons and gamma-rays from the Am-Be source. The loci associated with recoiling electrons from Compton scattering events

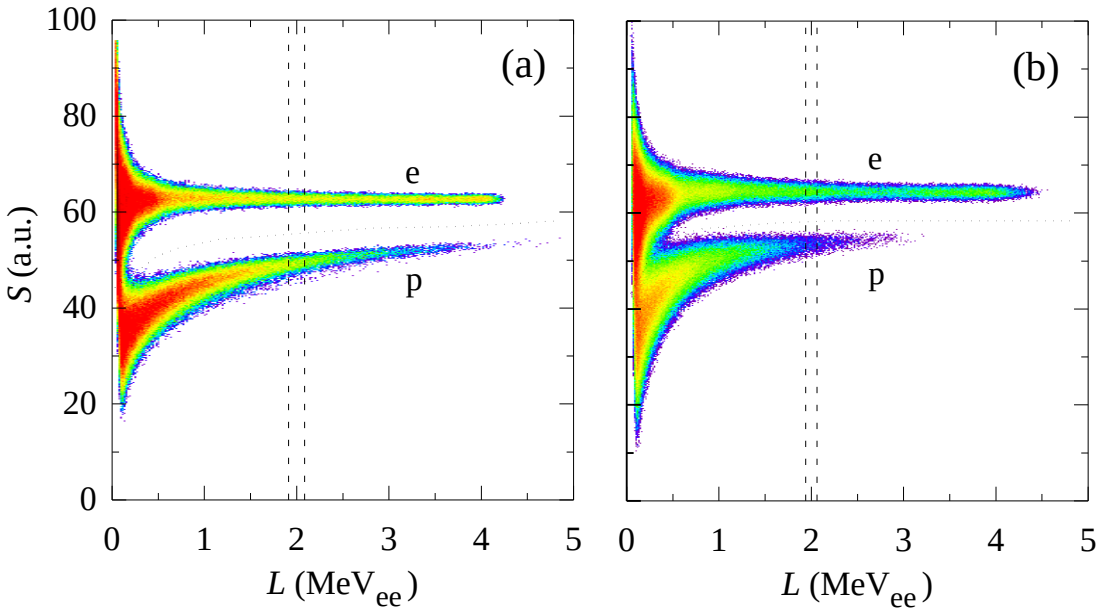

FIGURE 4.10: Counts as a function of light output parameter L and pulse shape parameter S for events in (a) EJ301 and (b) EJ299-33, when exposed to neutrons and gamma-rays from the Am-Be source. Loci associated with recoiling electrons (e) and protons (p) are indicated. The dotted lines indicate the cuts used to separate neutron and gamma-ray events and the dashed lines the cut used to select events in the range L = 1.9 to 2.1 MeV_{ee} .

and protons recoiling from n-p elastic scattering are well separated over the full range of L for EJ301, while the loci for EJ299-33 overlap at lower L.

The dotted lines show cuts to separate events associated with neutrons and gamma-rays. The projections of these selections onto the L-axis are shown in Figure 4.11. The dashed lines in Figure 4.10 indicate a cut to select events in the range L = 1.9 to 2.1 MeV_{ee} , which are projected onto the S-axis in Figure 4.12(a). The light output spectra in Figure 4.11(a) show that EJ299-33 has a noticeably reduced energy resolution when compared to EJ301. Figure 4.11(b) shows that the relative amount of light produced by protons in EJ299-33 is smaller to that of protons in EJ301, and the efficiency for neutron detection is also slightly reduced.

The short integration time t_S was chosen in order optimise the FoM, with typical values of 30 ns and 50 ns for EJ301 and EJ299-33 respectively. Figure 4.12(b) shows FoM as a function of L for the two scintillators. The FoM for EJ301 remains above 1.0 for energies above 100 keV. The plastic scintillator displays significantly inferior FoMs across the entire light output range of the experiment, with FoM dropping below

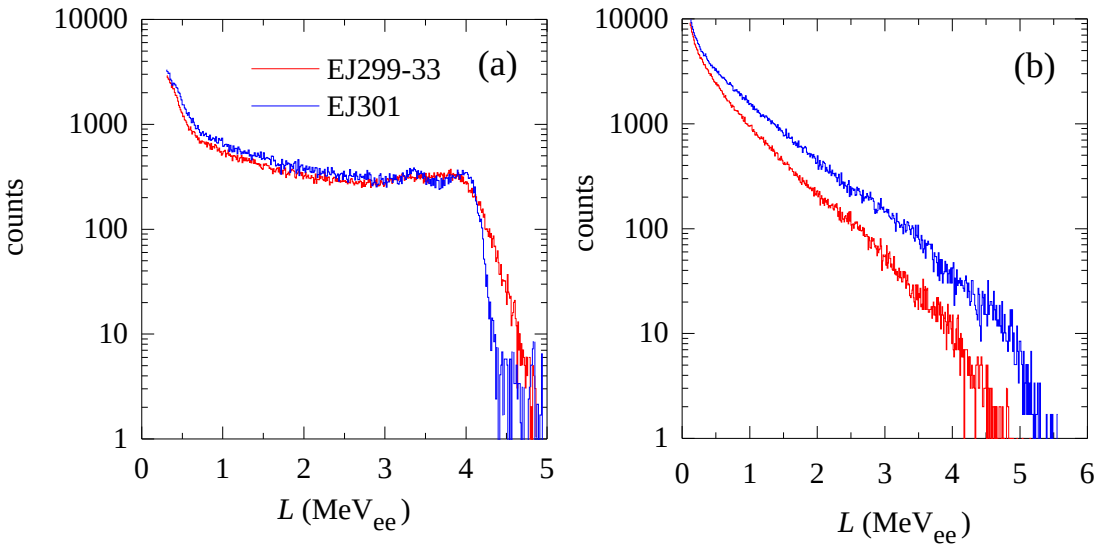

FIGURE 4.11: Light output L spectra from EJ299-33 and EJ301, for (a) gamma-rays and (b) neutrons from Am-Be, as selected by the cuts shown in Figure 4.10.

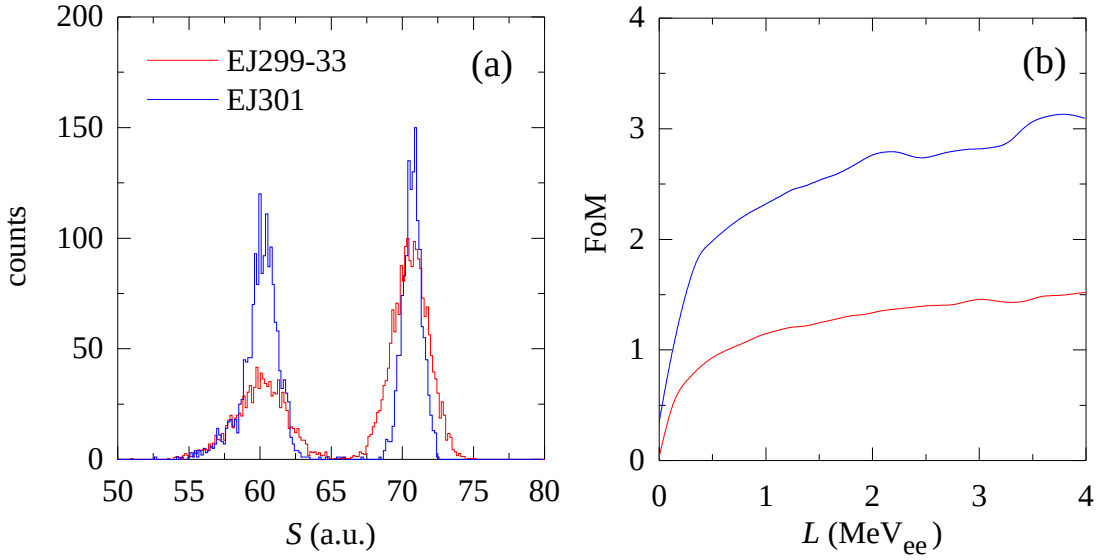

FIGURE 4.12: (a) Counts versus shape parameter S for events in the range of L = 1.9 to 2.1 MeV$_{ee}$, as selected by the cuts shown in Figure 4.10. The scale and offset of the EJ299-33 histogram have been adjusted in order to align the distributions; (b) Figure of merit versus light output parameter L for events in EJ301 and EJ299-33.

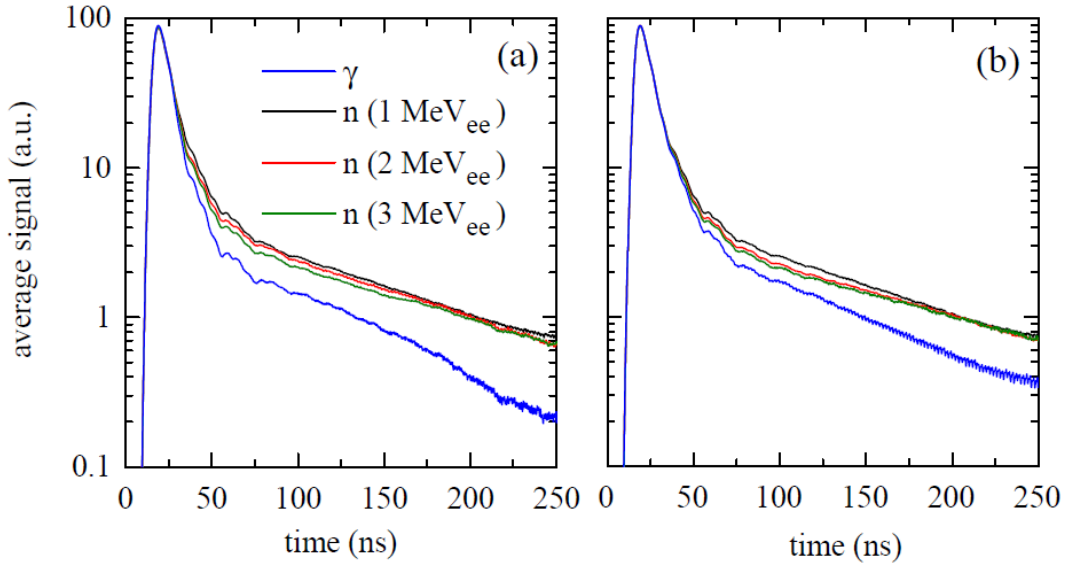

FIGURE 4.13: Average signals produced by $L = 1$ MeV$_{ee}$ gamma-rays and $L = 1$, 2 and 3 MeV$_{ee}$ neutrons in (a) EJ301 and (b) EJ299-33, normalised to the same total integral.

1.0 for energies below 600 keV. These results are in line with previous experimental measurements [34], [39].

4.2 Pulse shapes

Figure 4.13 shows average signals produced by L = 1 MeV$_{ee}$ gamma-ray events and $L = 1$, 2 and 3 MeV$_{ee}$ neutron events in PMT-based detectors with (a) EJ301 and (b) EJ-299-33 scintillators. The average signals were calculated by summing over a number of events within narrow regions of L and normalising each event by their total integrals. There is noticeable variation in the pulse shape as a function of L for neutron pulses in both detectors, due to the dependence of specific energy loss of protons on particle energy. The bumps occurring at 50 ns are the result of PMT after-pulsing. The tails of the signals in Figure 4.13 can be fitted to an exponential decay function of the form of the form

$$f(t) = Ae^{-\frac{t}{\tau_1}} + Be^{-\frac{t}{\tau_2}} + Ce^{-\frac{t}{\tau_3}}, \tag{4.1}$$

where τ_1, τ_2 and τ_3 are the time constants of fast, medium and slow decay components respectively, and A, B and C are their relative weightings. As the same underlying physical processes are responsible for scintillation from both neutron and

(a) EJ301	$\tau_1 = 4.32 \pm 0.10$ ns; $\tau_2 = 11.17 \pm 0.58$ ns; $\tau_3 = 106.5 \pm 2.5$ ns			
Variable	gamma-rays	n (L=1 MeV_{ee})	n (L=2 MeV_{ee})	n (L=3 MeV_{ee})
A	0.674	0.428	0.556	0.581
B	0.261	0.380	0.337	0.323
C	0.053	0.111	0.095	0.086
R^2	0.999	0.997	0.999	0.998
(b) EJ299-33	$\tau_1 = 4.66 \pm 0.10$ ns; $\tau_2 = 11.84 \pm 0.29$ ns; $\tau_3 = 111.0 \pm 1.7$ ns			
Variable	gamma-rays	n (L=1 MeV_{ee})	n (L=2 MeV_{ee})	n (L=3 MeV_{ee})
A	0.507	0.470	0.493	0.497
B	0.421	0.415	0.405	0.408
C	0.061	0.100	0.089	0.084
R^2	0.999	0.999	0.998	0.998

TABLE 4.1: Fitted parameters of pulse shapes for (a) EJ301 and (b) EJ299-33, for $L = 1$ MeV_{ee} gamma-rays, and $L = 1$, 2 and 3 MeV_{ee} neutrons, as well as the coefficient of determination R^2 for each fit.

gamma-rays in the detector, the time constants should be identical for both neutron and gamma-ray signals. Equation 4.1 was used to fit the tail of the average gamma-ray signals shown in Figure 4.13. The time constants determined by the fit were then used to fit the average signals from $L = 1$, 2 and 3 MeV_{ee} neutron events, in order to determine the relative weightings. The results are given in Table 4.1. In each case, the coefficient of determination R^2 is close to unity, indicating excellent agreement with the data.

The two scintillators have similar time constants, but the relative weightings differ. In particular, fit parameter B is much larger in EJ299-33. The difference between the values of fit parameter A for neutron and gamma-ray events in EJ299-33 is far smaller than the difference in EJ301, which results in the inferior PSD performance described by [17], [42].

4.3 Simulating light output response and timing of EJ299-33 in Geant4

While Section 4.1.2 describes the construction of a response matrix directly, from measurements of light output for various incident neutron energies, a response matrix may similarly be constructed through the use of a Monte Carlo simulation, at least for lower energy (<20 MeV) incident neutrons for which elastic scattering is the dominant mechanism of energy transfer. This approach has previously been demonstrated [21], [113] and is widely used for standard liquid scintillators. In order to develop a similar response matrix for EJ299-33, validation of the simulation of light output for an EJ299-33 based detector is necessary.

The Geant4 detector simulation toolkit is a modular, highly extensible and open source Monte Carlo particle transport code written in C++ [114]. It has been widely used to simulate the passage of ionising particles through liquid scinitillation detectors, such as EJ301 [115], [116] and EJ309 [117]. Alternative Monte Carlo codes, such as MCNPX-PHOTRACK [118] and SCINFUL [113] provide only limited flexibility in terms of detector geometry, light collection and materials. Geant4 provides the ability to simulate the emission of photons in arbitrarily defined scintillating materials (both in terms of geometry and composition), as well as the tracking of emitted photons in the detector, and the simulation of photodectectors, such as PMTs and SiPMs. A new feature added to version 10.0 of the Geant4 Monte-Carlo simulation toolkit is the ability to simulate the time-dependent light output of nonlinear scintillators. This feature has been previously validated for the simulation of an EJ301 liquid scintillator [119].

In this section, the experimental measurements described in Sections 4.1.3 and 4.2 are compared to the output of a Geant4 simulation of a cylindrical EJ299-33 scintillator (51 mm diameter $\times$ 51 mm), coated with a reflective paint and coupled to an idealised PMT (with a PDE of 25%). The parameters in Table 4.1 were used as input to the time-dependent light output of the simulation. Parameters related to total light output response of the scintillator to protons were taken from Lawrence et. al. [39], while general material properties, such as scintillation effeiciency, emission spectrum, density and chemical composition were taken from the EJ299-33 datasheet [14].

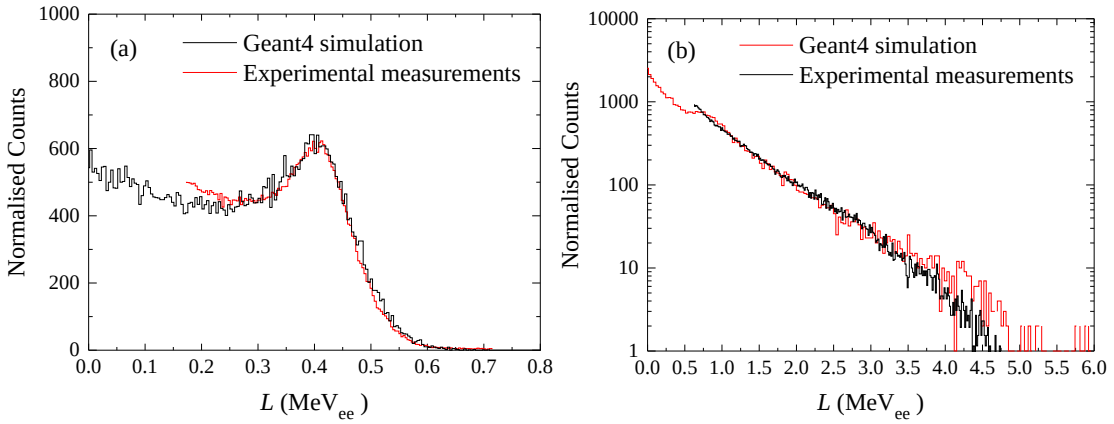

FIGURE 4.14: Simulated and measured light output spectra from (a) gamma-rays originating from a ^{137}Cs source and (b) neutrons from an Am-Be source incident on an EJ299-33 scintillator.

For each simulation step, the number of photons generated by the scintillation process due to an ionising particle is calculated by the random sampling of a Gaussian distribution, with a mean μ_{ph} and standard deviation σ_{ph} defined as [120]

$$\mu_{\mathrm{ph}} = Y \times E_{\mathrm{dep}}, \tag{4.2}$$

$$\sigma_{\mathrm{ph}} = R \times \sqrt{\mu_{\mathrm{ph}}}, \tag{4.3}$$

where Y is the scintillation yield, taken as (for electrons) 8600 photons per MeV, E_{dep} is the energy deposited by the ionising particle in the current simulation step and R is the intrinsic resolution scale of the detector. As the tracking of up to tens of thousands of individual scintillation photons for each incident ionising particle is extremely computationally intensive, a simple optimisation was employed to reduce the number of tracked photons: The PDE of the PMT was adjusted to 100% (a factor of 4 increase), while the scintillation yield was decreased by a factor of 4, resulting in the same number of detected photons and identical light output spectra, while speeding up the simulation significantly. The resolution scale R was adjusted in order to fit the simulated light output spectra to the measured spectra.

Figure 4.14 (a) shows simulated and measured light output spectra from gamma-rays produced from a ^{137}Cs calibration source placed 15 cm from the front edge of

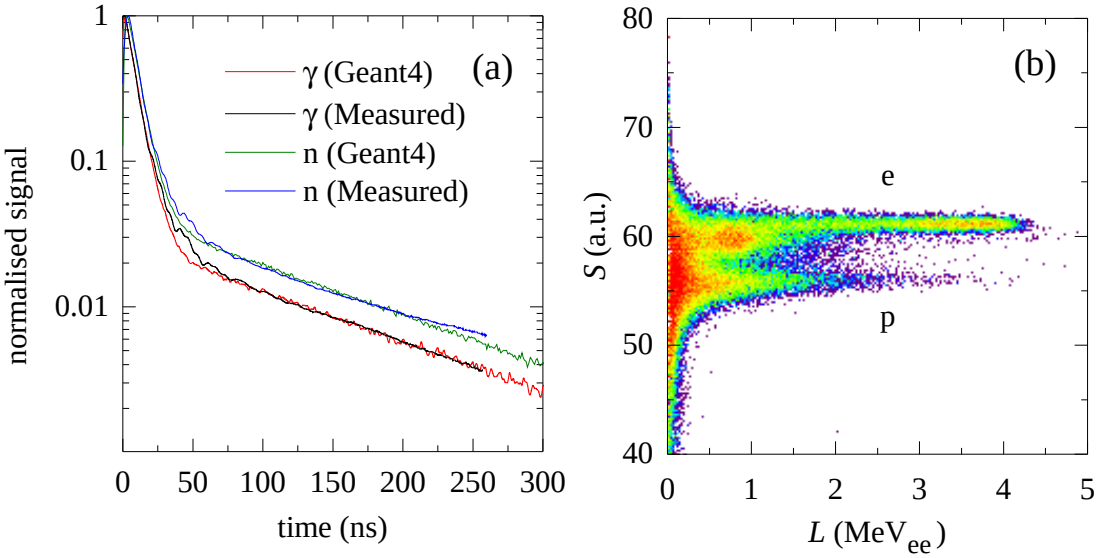

FIGURE 4.15: (a) Simulated and measured average signals produced by gamma-rays from ^{137}Cs and neutrons from Am-Be in EJ299-33. The signals have been normalised by their pulse height. (b) Counts as a function of light output parameter L and pulse shape parameter S for simulated events in EJ299-33.

the scintillator. The spectra match closely in the region of the Compton edge (478 keV), but the simulated spectrum is suppressed at lower L. This is most likely due to the presence of additional gamma-rays scattering off surrounding material in the experimental setup. Figure 4.14 (b) shows simulated and measured light output spectra from neutrons produced from an Am-Be source, placed 30 cm from the front edge of the scintillator. Similar results have been observed in Geant4 simulations of an EJ301-based detector [121].

Figure 4.15(a) compares the simulated and measured average signals produced by gamma-rays and neutrons from ^{137}Cs and Am-Be sources respectively. There is good agreement between measured and simulated signals for both gamma-ray and neutron signals. The presence of reflections in the PMT leads to the discrepancy between simulated and measured signals in Figure 4.15(a) around $t = 50$ ns. Currently, only two decay components can be simulated by the Geant4 toolkit, leading to the suppression of the simulated neutron signal above $t = 200$ ns.

The use of a simulation capable of reproducing pulse shapes allows the investigation of the effect of changes to detector geometry, wrapping or light collection mechanisms, all of which influence pulse shape discrimination capability. Figure 4.15(b)

shows the distribution of simulated events as a function of the light output parameter L, and the pulse shape parameter S, showing a clear separation between neutron and gamma-ray events at higher energies, and a similar behaviour to the measured distribution shown in Figure 4.10(b). The absence of bending of the proton locus in Fig. 4.15(b) is due to a limitation of the Geant4 toolkit, which currently does not allow for an energy-dependent weighting of the fast and slow scintillation decay components.

4.4 Discussion

The pulse height spectrum unfolding method is widely used as a method for neutron spectrometry, particularly when nanosecond-timing is not available. This chapter presented the first measurements of the response of EJ299-33 plastic scintillator to quasi-monoenergetic neutrons over the energy range 10-100 MeV. The EJ301-based detector produced results which agreed better with the time-of-flight spectrum overall, although the refolded fits were excellent for both detector types. The plastic scintillator EJ299-33 thus offers very good prospects for use as a neutron spectrometer over a wide energy range in neutron fields having any type of time structure.

While the plastic scintillator displays good PSD capability, FoM values are significantly lower than those for the liquid scintillator. This inhibits efficient separation of neutron and gamma-ray events at low energies. An investigation into the pulse shapes of the two scintillators shows that the weighting of the fast decay component of scintillation does not differ between proton and electron interactions as significantly in EJ299-33 when compared to EJ301, leading to a lower FoM. The simulation of pulse shapes using the Geant4 toolkit provides a quantitative method of predicting PSD capability, and is capable of reproducing the pulse shapes and PSD capability of the EJ299-33 scintillator. Both the hazards and inconveniences associated with liquid scintillator are removed, while pulse shape discrimination may be implemented with good quality.

Chapter 5

Development of a SiPM-based compact neutron spectrometer

Previous chapters have described measurements performed using PMT-based detectors, and have shown that PSD performance and energy resolution of EJ299-33-based detectors are significantly poorer than that of conventional EJ301-based liquid scintillator devices. However, the significant practical advantages of utilising a plastic scintillator justify the use of EJ299-33 as a scintillator in detectors that must be rugged, compact and able to operate in a wide variety of environments. A number of adjustments to detector design offer possible improvements to energy resolution and PSD performance. Firstly, variations in pulse shape have been attributed to inhomogeneities arising from the manufacturing process. These variations should be less severe in smaller scintillators, therefore a detector with a smaller scintillator size should improve PSD performance. Secondly, improving light collection by utilising multiple photomultipliers would improve PSD performance and energy resolution. SiPMs are an ideal solution, offering excellent photo-detection efficiency in a compact form factor, with low power requirements.

This chapter describes the development and testing of SiPM-based compact neutron spectrometers, designed for applications requiring low power usage, as well as a compact and rugged form factor. Prototype spectrometers were designed to be read out by a custom built FPGA-based digitizer board, capable of performing on-line charge comparison PSD and interfacing with mobile devices via a USB or Bluetooth connection. However, at the time of writing, the custom digitizer is still under development. As such, all measurements in this chapter have been performed using the

CAEN DT5730 digitizer. Similar results are expected with the custom digitizer, as both the sampling rate and bit-depth are designed to match the DT5730. Two prototype spectrometers were developed:

- A single-scintillator device, consisting of a plastic scintillator, coupled to two SiPMs, capable of pulse shape discrimination and neutron energy spectrum unfolding when paired with a suitable data acquisition system.
- A multi-scintillator device, consisting of four plastic scintillators, each coupled to two SiPMs, and arranged around a cross-shaped neutron shield. The multi-scintillator device provides direction-sensitive measurements by a comparison of the count rates between scintillators.

5.1 Single-scintillator device

5.1.1 Device description

The single-scintillator prototype consists of a square prism (6×6×50 mm^3) of EJ299-33 plastic scintillator, coupled to two SensL MicroFC-60035 SiPMs, with an active area of 6×6 mm^2, matching the cross-sectional area of the scintillator. The SiPMs were coupled to the scintillator with Dow Corning optical grease. A single layer of 3M Vikuiti Enhanced Specular Reflector (ESR) material was used as a reflective wrapping around the scintillator. ESR wrapping was found to be more efficient than diffuse wrapping, such as Tyvek or PTFE tape, due to the elongated geometry of the scintillator. A schematic of the device is shown in Figure 5.1.

The use of two SiPMs improves light collection by doubling the active area for photo-detection. Variations in pulse integrals, due to variations in the interaction position within the scintillator (as illustrated in Figure 5.2), can be mitigated by using a geometric average of the pulse integrals of each photodetector [20]:

$$Q_{\text{mean}} = \sqrt{(Q_A \times Q_B)}, \tag{5.1}$$

where Q_A and Q_B are the pulse integrals of SiPM A and B respectively. A similar process can be applied to short integrals during pulse shape discrimination. In

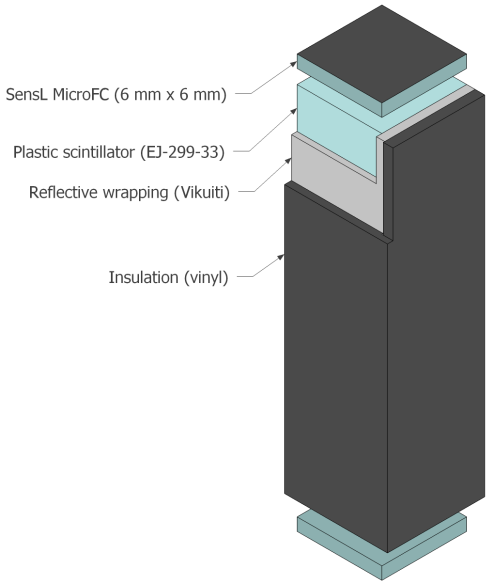

FIGURE 5.1: Schematic of the single scintillator detector, consisting of a square prism of EJ299-33 plastic scintillator, coupled to two SensL MicroFC SiPMs.

addition, co-incidence triggering between the two SiPMs can reduce the presence of noise attributed to dark pulses at low energies [122]. Figure 5.3 shows individual light output spectra, as well as that of the combined geometric mean for gamma-rays from a ^{137}Cs source. While the Compton edges of the individual light output spectra for both SiPMs are not visible, the Compton edge of the combined light output spectra is clearly resolvable. It was found that the energy resolution of the ^{137}Cs Compton edge improved from $11.9 \pm 0.2\%$ with a single SiPM setup to $7.7 \pm 0.1\%$ with a dual-SiPM setup. In addition, calculations of figure of merit for $L = 1.00 \pm 0.05$ MeV$_{\text{ee}}$ neutrons from an Am-Be source improved from 1.23 ± 0.02 to 1.67 ± 0.01. The significant improvements to energy resolution and PSD performance justify the use of a dual-SiPM setup.

5.1.2 Silicon Photomultipliers (SiPMs)

SiPM measurements described in this work were made using SensL MicroFC-60035 SiPMs [61]. These SiPMS have a 6×6 mm^2 active area, consisting of 18980 microcells, each of dimensions 35×35 μm^2. The breakdown voltage (V_{br}) is approximately 24.5 V, with a typical temperature dependence of 21.5 mV/°C. The spectral range lies between 300 nm and 800 nm, with photon detection efficiency (PDE) function peaking at 420 nm,

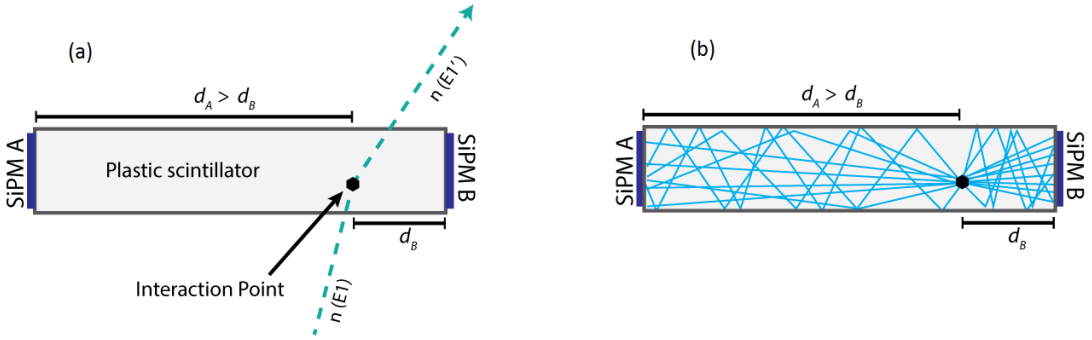

FIGURE 5.2: Neutron scattering in a plastic scintillator. (a) Interactions will occur closer to one SiPM than to the other. (b) Photons from the scattered proton are emitted approximately isotropically, with more photons hitting the closer SiPM. This leads to an increased pulse integral in SiPM B.

matching the emission peak of the EJ299-33 scintillator. Typical PDE at this wavelength is between 30% and 40%, depending on the applied bias above V_{br}, or overvoltage. The SensL C-series SiPMs have a significantly lower dark current (typically 0.62 μA at V_{br}+ 2.5 V) than the preceding B-series SiPMs [63], which has been shown to improve PSD performance [68].

In addition to standard output, SensL B- and C-series SiPMs feature a "fast" output, which is coupled to individual microcells, resulting in an output signal with rise times and pulse widths of the order of 1 ns [123]. Fast output can be used for triggering, or for applications where time resolution is critical.

SiPMs were mounted on a custom-built printed circuit board (PCB). The initial design (MK-I) was negatively biased, with AC-coupled readout of both the slow and fast outputs from the SiPMs, with the SiPM mounted in the centre of a 25×25 mm^2 board. However, a subsequent revision (MK-II) of this board switched to a positive bias with DC-coupled readout of the slow output, in order to simplify power supply requirements, and to enable accurate measurements of dark currents, in order to reliably determine breakdown voltages.

A circuit diagram of the PCB configured in AC-coupled mode is shown in Figure 5.4. SiPM solder points are indicated by points A, K and F. Fast output is passed through an RF transformer (U2), in order to improve the signal's impedance matching to 50 Ω. Standard, or "slow" output, is passed through a series capacitor (C5),

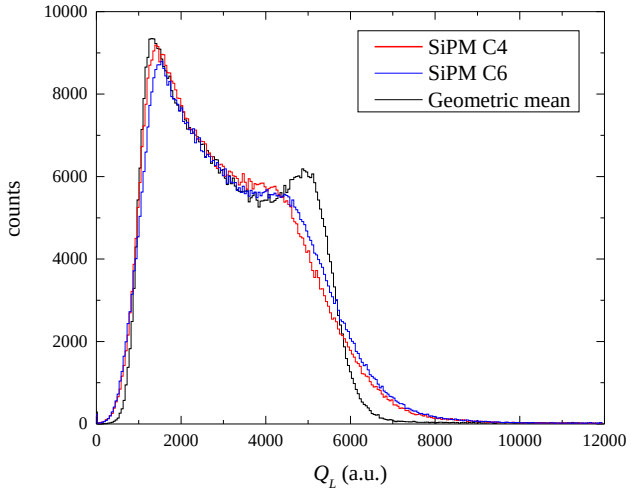

FIGURE 5.3: Counts versus long integral Q_L for gamma-ray events from a ^{137}Cs source, measured using the single-scintillator prototype. The figure shows histograms from individual SiPMs, as well as that of the geometric mean.

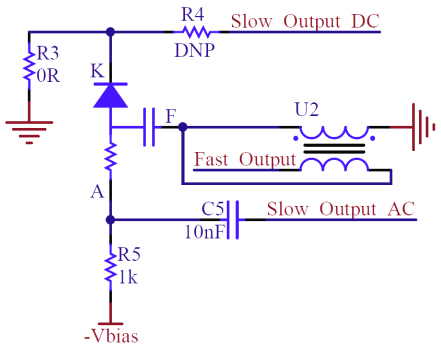

FIGURE 5.4: Schematic for MicroFB breakout board, configured in AC-coupled mode.

which removes the baseline from the output. MCX connectors were chosen in order to satisfy impedance matching and signal bandwidth requirements, and to preserve compatibility with propitiatory digitizers.

Figure 5.5 shows both revisions of the PCBs. The SiPM mounting position on the MK-II PCB was moved to the corner of the board, and the board size was decreased to 20×20 mm^2, to facilitate its use in the multi-scintillator prototype described in Section 5.2. SiPMs were supplied with a bias from a B&K 9120A bench power supply. SiPMs were operated at an over-voltage of between 2.5 V and 5.5 V.

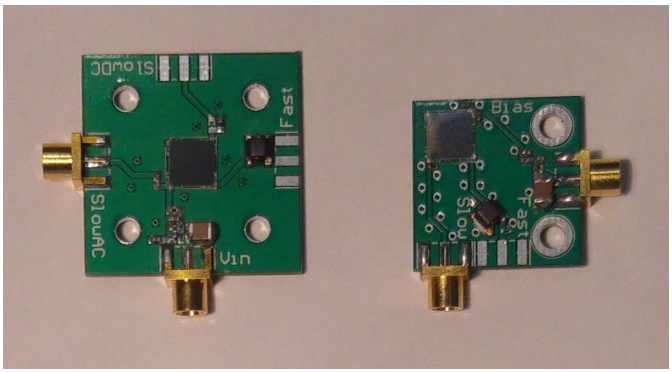

FIGURE 5.5: Printed circuit board holders for SensL MicroFC SiPM. The initial AC-coupled version (MK-I) is shown on the left, while the revised DC-coupled version (MK-II) is shown on the right.

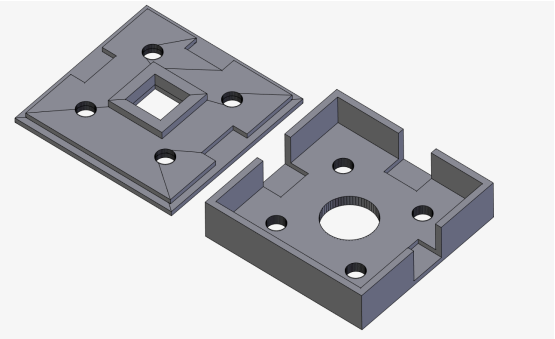

FIGURE 5.6: 3D model generated by the python script.

5.1.3 Detector housing

SiPMs were housed in 3D-printed structures. A python script was written to generate a virtual 3D model in the Blender modelling program [124]. The script was parametrised, to allow for rapid prototyping of detector geometries and housing parameters. The generated model was then printed in polylactic acid (PLA) using an Ultimaker2 3D-printer. An example of the virtual model is shown in Figure 5.6. The assembled detector was placed in a light-tight box during measurements to prevent ambient light from reaching the SiPMs. An LM35 sensor was placed inside the box to monitor the SiPM temperature.

Figure 5.7 shows the wrapped scintillator and the MK-I PCB encased in 3D-printed housing, as well as the assembled detector inside a light box.

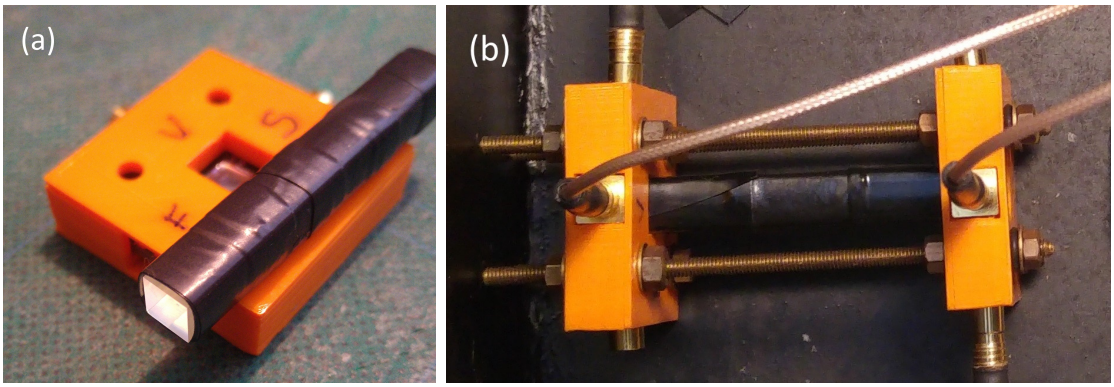

FIGURE 5.7: (a) $6 \times 6 \times 50$ mm^3 EJ299-33 scintillator wrapped in Vikuiti ESR and vinyl, shown with 3D-printed housing for the MK-I PCB. (b) Assembled single scintillator detector with 3D-printed housing.

5.1.4 Systematic tests

A total of 17 SiPM PCBs were produced and tested: 8 MK-I samples (C1 to C8), and 9 MK-II samples (D0 to D8). A number of systematic tests were performed on the SiPMs, in order to determine breakdown voltages, optimal operating voltage, as well as the number of baseline samples required for optimal PSD performance.

In order to reliably measure the breakdown voltage V_{br} for each MK-I board, as well as the dependence of V_{br} on temperature, a pulsed LED light source was constructed. An 84 MHz Arduino Due micro-controller was used to create a pulse width modulated (PWM) signal, with a pulse width of 24 ns (corresponding to two clock cycles of the micro-controller), and a duty cycle of 1%. This signal was used to drive a blue LED. The pulsed light source and the SiPM were placed in a light-tight box. The pulsed signal was used as a trigger for the SiPM readout, and the SiPM signal was integrated across a 500 ns interval, starting from the time of trigger crossing. The SiPM signal was amplified by two ZFL-1000LN low noise amplifiers [125], for a combined gain of 40 dB.

Figure 5.8 shows counts versus signal integral Q_L, for measurements taken with a bias voltage of 25.5 V, with a temperature range of between 22 °C and 23 °C and the light source approximately 30 cm from the SiPM. Peaks corresponding to the detection of a single photon per LED pulse, up to the coincident detection of 9 photons per LED pulse, are clearly visible. The left-most peak corresponds to the presence of dark pulses. While dark pulses produce signals of equivalent amplitude to those produced by the detection of single photons, they occur at random intervals, rather than shortly after the

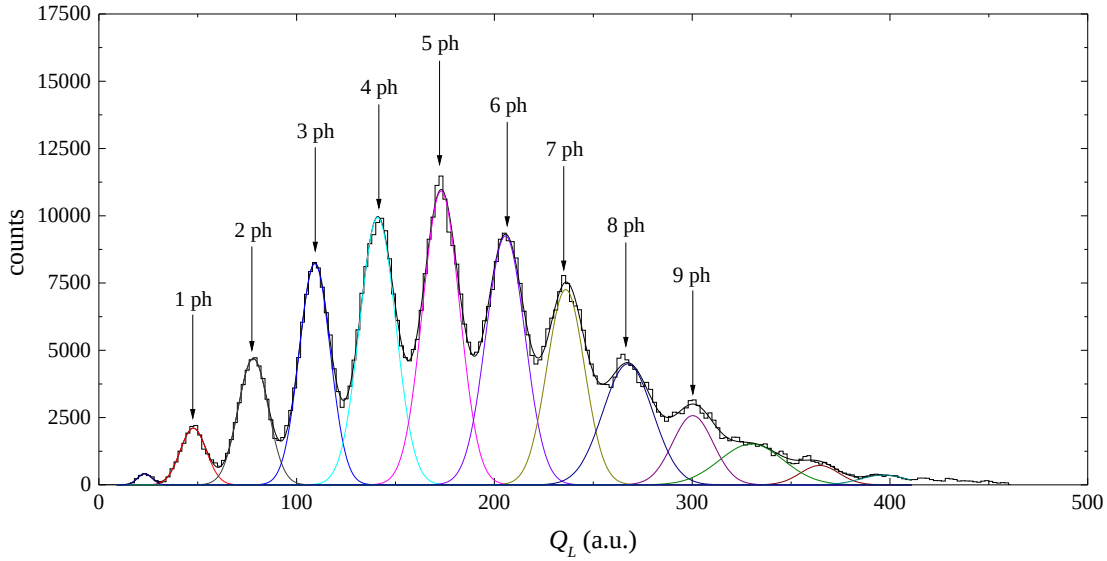

FIGURE 5.8: Counts versus signal integral Q_L for low intensity light, produced by a pulsed LED, incident on a MicroFC-60035 SiPM, biased at 25.5 V at a temperature of 22-23 °C. The Gaussian distributions due to the coincident detection of up to 9 photons per event are indicated.

LED pulse. As such, the average signal integral produced by a dark pulse within the 500 ns interval is significantly smaller than the signal integral produced by a photon originating from the pulsed LED. A similar spectrum was observed for the majority of SiPM samples tested. However, those samples that had been previously exposed to radiation for prolonged periods of time (C1 & C2) displayed significantly broader distributions.

The widths of the distributions in Figure 5.8 are due to a number of contributing factors: electronic noise in the amplifiers, variations in the gain of individual micro-cells in the photomultiplier, the presence of dark pulses and (in the case of coincident photons), variations in the arrival times of incident photons, due to the finite pulse width of the driving signal.

Figure 5.9 (a) shows the fitted mean values (Q_C) of the Gaussian distributions for each photon count shown in Figure 5.8. The slope of the linear fit can be used to determine ΔQ_{Ph}, the change in Q_C per additional coincident photon. Figure 5.9 (b) shows ΔQ_{Ph} versus applied bias voltage. As the SiPM gain is known to be proportional to overvoltage [61], the x-intercept of the linear fit of ΔQ_{Ph} versus applied bias determines V_{br}. The breakdown voltage for the sample shown in Figure 5.9 was determined to be 24.55 $\pm$ 0.03 V. Similar measurements of V_{br} at differing temperatures showed that the

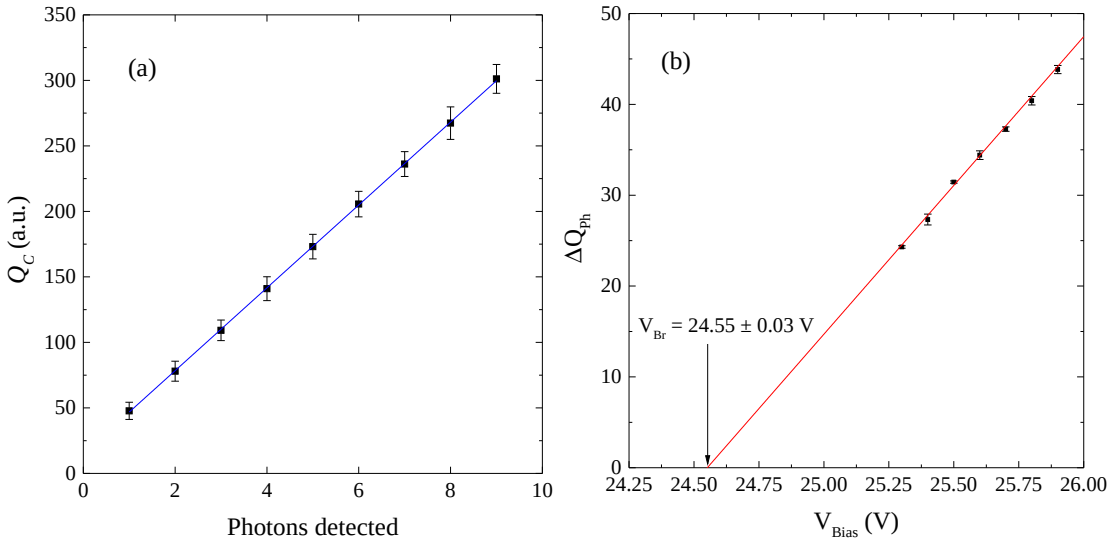

FIGURE 5.9: (a) Fitted mean value of the Gaussian distributions for each photon count, at a bias voltage of 25.5 V. The slope of the linear fit defines ΔQ_{Ph}, the change in Q_C per additional photon. (b) ΔQ_{Ph} versus applied bias voltage. The x-intercept defines the breakdown voltage V_{br}.

TABLE 5.1: SiPM breakdown voltage V_{br} for each MK-I sample, determined by the fits shown in Figure 5.9. V_{br} for samples C1 and C2 could not be determined in this manner, due to radiation damage.

Sample	V_{br}	$u(V_{\mathrm{br}})$
C1	–	–
C2	–	–
C3	24.59	0.02
C4	24.55	0.03
C5	24.61	0.02
C6	24.55	0.02
C7	24.75	0.04
C8	24.70	0.02

change in V_{br} was 20 $\pm$ 3 mV/°C. Subsequent measurements described in this work were operated at a constant over-voltage, rather than a constant applied bias voltage, taking into account the temperature dependence of V_{br}.

Figure 5.10 (a) shows a typical digitised signal for measurements taken with an overvoltage of 2.0 V, and the pulsed light source approximately 1 cm from the SiPM. The ZFL-1000LN amplifiers were not used during this measurement. Due to the large number of co-incident photons detected, the signal shape is extremely clean. Figure 5.10 (b) shows counts versus signal integral Q_L, for measurements taken with overvoltages of 1.0, 2.0, 3.0 and 4.0 V. At high light intensities, the signal integral is dependent

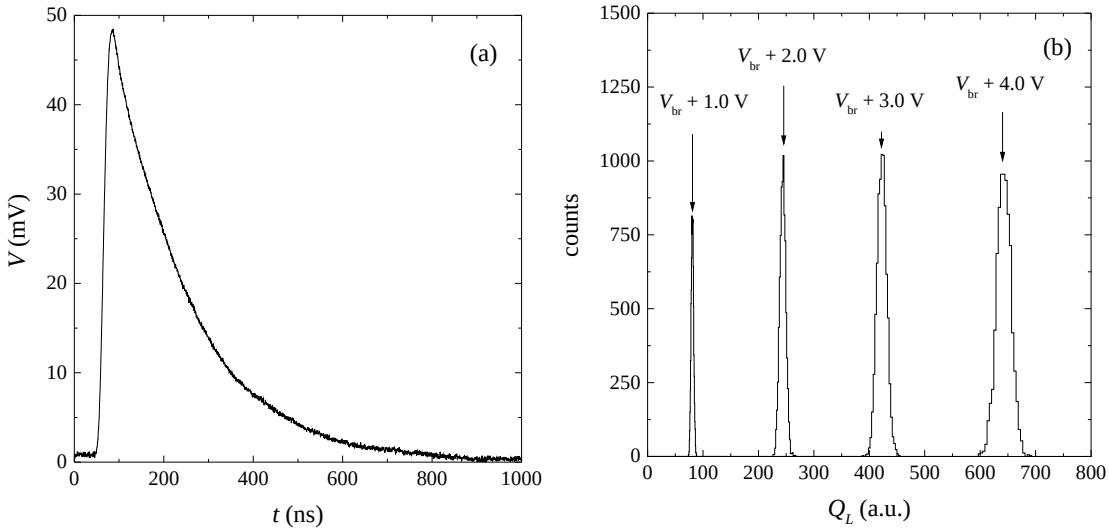

FIGURE 5.10: (a) Typical digitised signal for measurements taken with an over-voltage of 2.0 V, and the pulsed light source approximately 1 cm from the SiPM. (b) Counts versus signal integral Q_L, for over-voltages of 1.0, 2.0, 3.0 and 4.0 V.

both on the microcell gain and the PDE. While gain varies linearly with overvoltage, PDE follows an exponential relationship [61], of the form

$$\mathrm{PDE}(V_{\mathrm{over}}) = y_0 - Ae^{-V_{\mathrm{over}}/b}, \tag{5.2}$$

where y_0 is the maximum PDE, and A and b are parameters defining the exponential trend towards maximum PDE with increasing V_{over}. As Q_L is proportional to the product of the microcell gain and the number of microcells fired, the relationship between Q_L and V_{over} for a fixed number of incident photons is the product of Equation 5.2 and a linear term:

$$Q_L(V_{\mathrm{over}}) = C \times V_{\mathrm{over}} \times (y_0 - Ae^{-V_{\mathrm{over}}/b}), \tag{5.3}$$

where C is a scaling constant. Figure 5.11 (a) shows fitted mean values (Q_C) versus V_{over}, with the pulsed light source approximately 1 cm from the SiPM, along with a fit according to Equation 5.3. The fit parameters of Equation 5.3 can be used to recover (up to a constant factor) the PDE as a function of V_{over}. Figure 5.11 (b) shows PDE versus V_{over}, relative to PDE at V_{over} = 2.5 V, along with a fit of Equation 5.2.

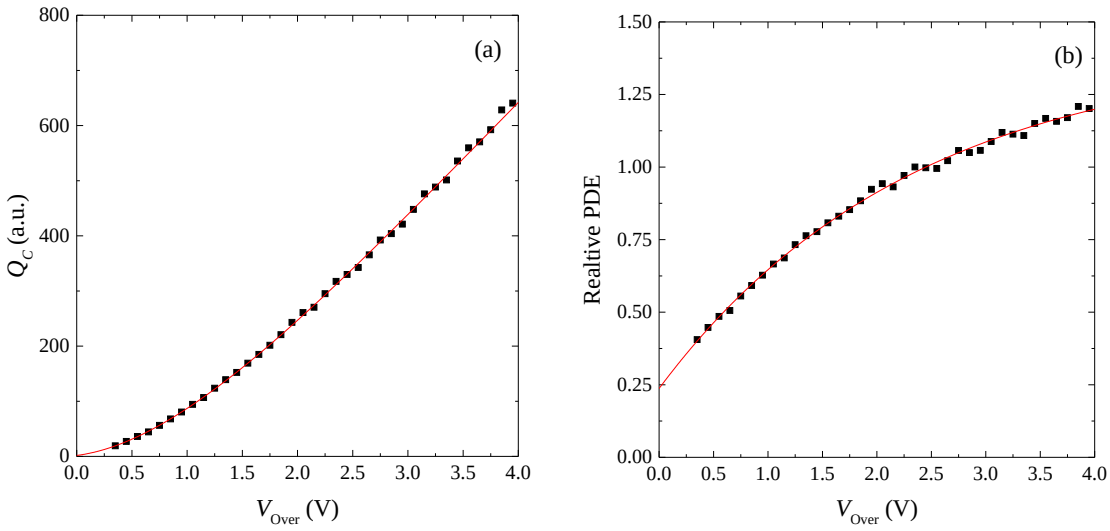

FIGURE 5.11: (a) Measured and fitted relationship between fitted mean values (Q_C) and V_{over}. (b) Measured and fitted relationship between PDE and V_{over}, relative to PDE at V_{over} = 2.5 V.

As the DC-coupled MK-II boards allowed for accurate measurements of dark current, a more expedient method of determining the breakdown voltage of each SiPM was used. It was found that, for over-voltages below 3 V, dark current in a reverse-biased SiPM increases approximately quadratically with over-voltage. Below the breakdown voltage, a linear relationship is generally observed [126], but this leakage current is orders of magnitude smaller than the dark current measured above breakdown voltage. As such, an approximate relationship between dark current and V_{bias} was taken as:

$$I(V) = \begin{cases} I_0 + I_1(V - V_{\text{br}})^2 & \text{if } V \geq V_{\text{br}} \\ I_0 & \text{if } V < V_{\text{br}} \end{cases} \tag{5.4}$$

where I_0 and I_1 are constants to be determined by fitting measured data. For each sample, the dark current was measured using a multimeter, while the bias voltage was swept from 24 V to 27 V in 10 mV steps. Figure 5.12 shows measured dark current versus bias voltage for sample D2, along with a fit to Equation 5.4. The breakdown voltage from the fit shown in Figure 5.12 was 24.415 $\pm$ 0.004 V, while the coefficient of determination was $R^2 = 0.9998$, indicating an excellent fit to the measured data.

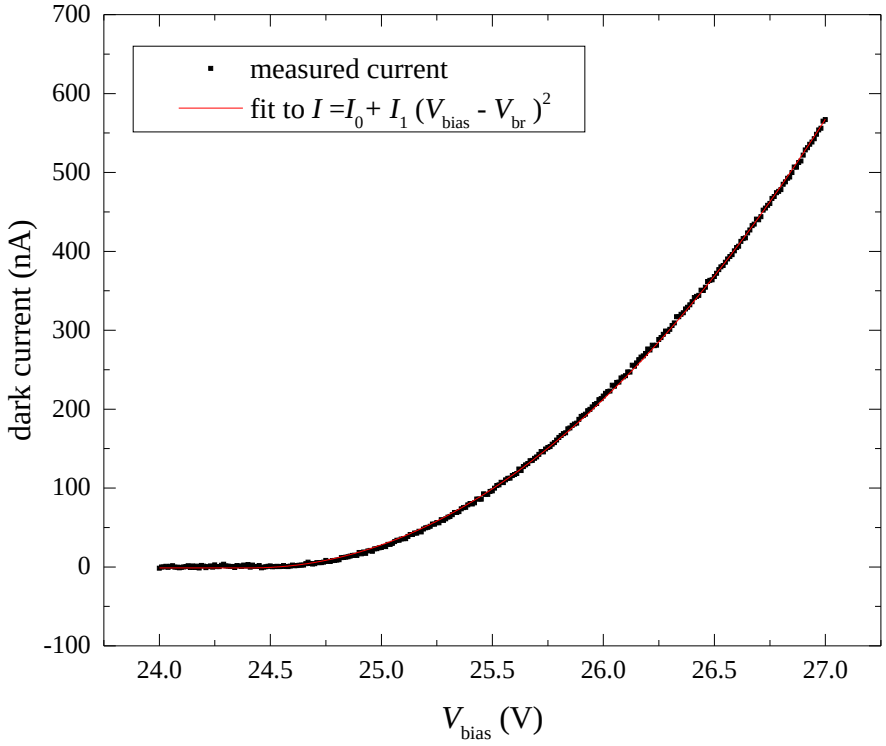

FIGURE 5.12: Dark current versus applied bias for SiPM sample D2. A piecewise fit of dark current to a quadratic function above V_{br} is shown.

Sample D3 was found to be non-functional, and sample D6 displayed erratic behaviour during measurements of dark current. The coefficient of determination was $R^2 > 0.998$ for fits to Equation 5.4 for all other samples. An alternative method was used to confirm the breakdown voltage of sample D6. The pulsed LED source was placed approximately 1 cm from the sample, and the a histogram of signal integrals was measured as a function of bias voltage. Each histogram was fitted to a Gaussian distribution, and the means were then fitted to a modified form of Equation 5.3 in order to determine the breakdown voltage:

$$Q_L(V_{\mathrm{bias}}) = C \times (V_{\mathrm{bias}} - V_{\mathrm{br}}) \times (y_0 - Ae^{-(V_{\mathrm{bias}} - V_{\mathrm{br}})/b}). \tag{5.5}$$

Figure 5.13(a) shows mean signal integrals versus bias voltage for samples D1 and D6, along with fits to Equation 5.5. Both fits had a coefficient of determination $R^2 > 0.999$, indicating excellent matching of the experimental data to the fit. As the position of the LED source was not kept constant between measurements, scaling differences are to be expected.

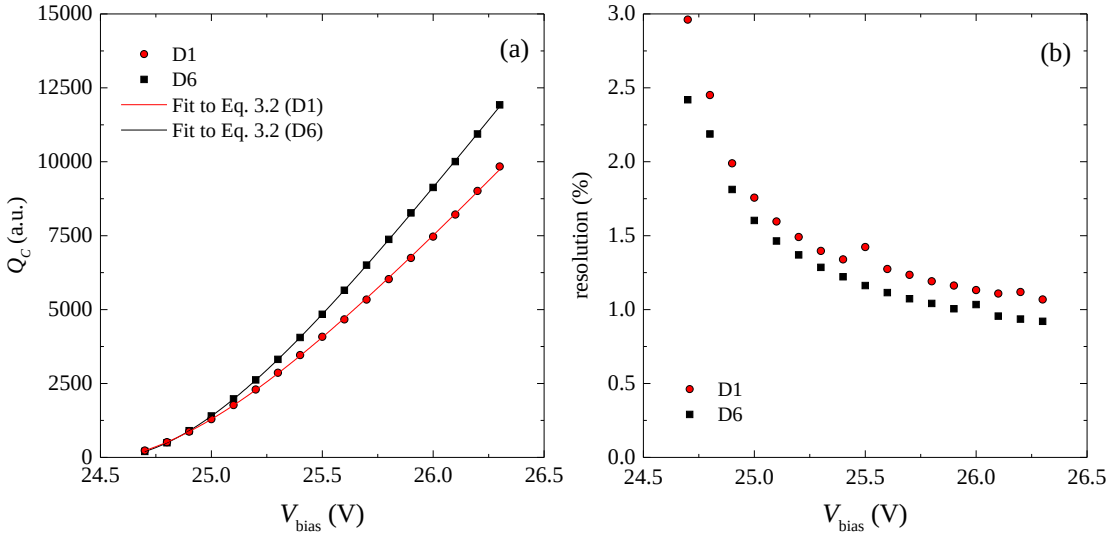

FIGURE 5.13: (a) Mean signal integral versus applied bias for two samples illuminated by a 20 ns pulsed LED. Variations in detector position are responsible for the scaling difference. (b) Resolution versus applied bias for pulsed LED measurements. The error bars in both plots are smaller than the symbols used.

The Gaussian fits were used to determine SiPM resolution (taken as the ratio between the standard deviation σ and mean μ) as a function of applied bias. As shown in Figure 5.13(b), resolution was consistently better when compared to that of sample D1, indicating that the erratic behaviour of sample D6 during dark current measurements did not affect further experimental measurements.

Table 5.2 gives SiPM breakdown voltage for each MK-II sample. The larger uncertainty in the value of V_{br} for sample D6 is due to the use of the alternative method described above.

Gamma-ray calibration of the single-scintillator detector was performed using the calibration sources described in Section 3.4.1, placed 20 cm from the scintillator, aligned with the 50 mm axis of the cuboid. As the CSDA range of 1 MeV electrons in a typical plastic scintillator is approximately 4.5 mm [107], a large fraction of Compton scattered electrons will exit the scintillator before depositing their full energy. However, this configuration significantly reduces the probability of forward-scattered electrons exiting the scintillator prematurely, thereby preserving the position of the Compton edge.

TABLE 5.2: SiPM breakdown voltage V_{br} for each MK-II sample, determined by the fits shown in Figure 5.12. V_{br} for sample D6 was determined from the fit shown in Figure 5.13 (a), as measurements of dark current were unreliable for this sample.

Sample	V_{br}	$u(V_{\mathrm{br}})$
D0	24.509	0.002
D1	24.526	0.003
D2	24.415	0.004
D3	–	–
D4	24.419	0.004
D5	24.496	0.004
D6	24.537	0.006
D7	24.510	0.003
D8	24.487	0.003

Non-linearity in SiPMs arising from the finite number of microcells [65], [127] leads to a non-linear relationship between long integral Q_L and light output L:

$$Q_L(L) = A(1 - e^{-BL}) + C, \tag{5.6}$$

where A, B and C are fitting constants. A comparison between a linear and non-linear fit for the calibration of the single-scintillator detector is shown in Figure 5.14. Deviations from a linear relationship are negligible for setups where the number of photons incident on the SiPM is small in comparison to the number of SiPM microcells.

As over-voltage increases, both SiPM gain and PDE increase, increasing pulse height. However, dark current increases with over-voltage, introducing a significant amount of noise at higher over-voltages. In order to determine the effect of SiPM over-voltage on detector energy resolution, pulse integral spectra from 664 keV gamma-rays from a ^{137}Cs source were acquired at SiPM over-voltages between 2.5 V and 5.5 V in steps of 0.5 V. Energy resolutions were determined by differentiating pulse integral spectra, and fitting the differentiated spectra to Gaussian functions, as described in Section 3.4.1. Figure 5.15 shows the pulse integral spectrum and differentiated spectrum for measurements with V_{over} = 3.0 V.

Figure 5.16(a) shows the position of the Compton edge versus V_{over}, along with a fit to Equation 5.3. Figure 5.16(b) shows energy resolution of the Compton edge (478 keV) versus V_{over}. The figure suggests an optimal operating voltage of $V_{\mathrm{over}} < 4.0$ V,

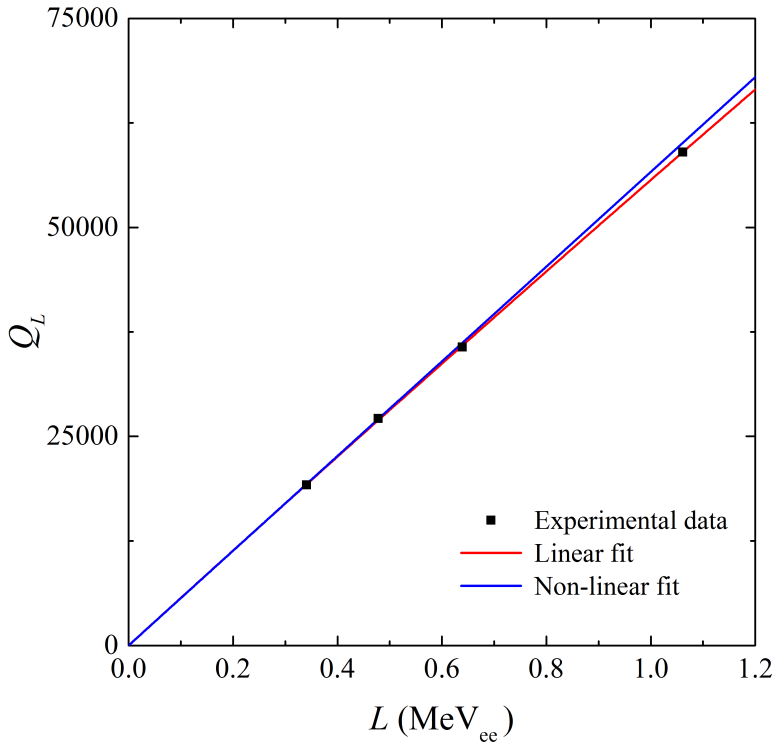

FIGURE 5.14: Linear and non-linear calibration fits for SiPM-based detector, using gamma-ray calibration sources.

above which a significant deterioration in energy resolution occurs, due to the increase in frequency and amplitude of dark counts.

As dark counts, cross-talk and after-pulsing in the SiPM can alter pulse shape, the effect of SiPM over-voltage on PSD performance was investigated. Pulses from neutrons and gamma-rays from an Am-Be source were acquired at SiPM over-voltages between 2.5 V and 5.5 V. Events in the light output range of $L = 1.00 \pm 0.05$ MeV$_{ee}$ were selected, and a histogram of counts versus pulse shape parameter S was produced. This histogram was fitted to a double Gaussian function, in order to determine the figure of merit, according to Equation 2.6.

Figure 5.17 (a) shows counts versus S for $L = 1.00 \pm 0.05$ MeV$_{ee}$ neutron and gamma-ray events from an Am-Be source, with SiPMs running at V_{over} = 2.5 V, along with a double Gaussian fit ($R^2 = 0.994$). Figure 5.17 (b) shows calculated figures of merit versus V_{over} for $L = 1.00 \pm 0.05$ MeV$_{ee}$ events, as determined from the Gaussian fits. FoM drops off above 3.5 V. This suggests that, taking into account the both energy resolution and PSD performance, SiPMs should be operated at approximately V_{over} = 3.5 V for optimal results.

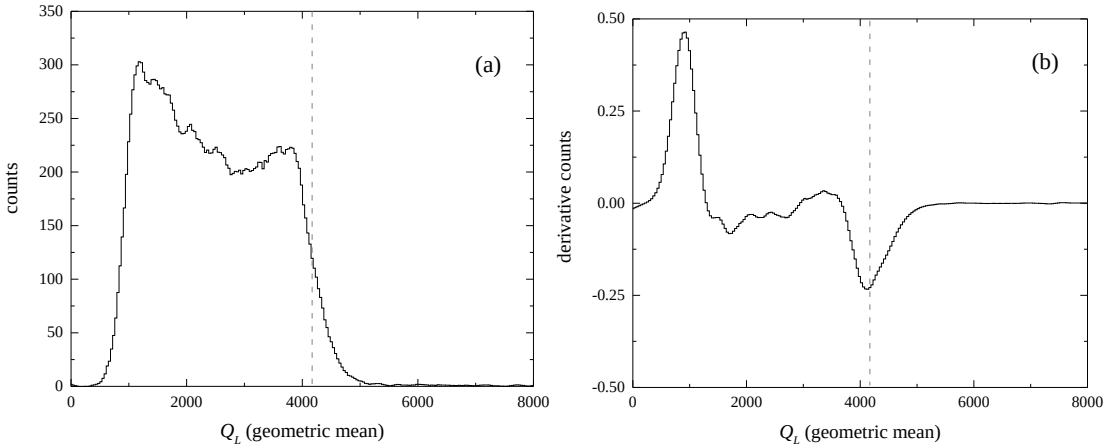

FIGURE 5.15: (a) Counts versus Q_L for measurements of 664 keV gamma-rays from a ^{137}Cs source, with each SiPM running at V_{over} = 3.0 V. The value of Q_L was taken as the geometric mean of Q_L for each SiPM. (b) Derivative of histogram shown in (a), in order to determine the position of the Compton edge, indicated by the dashed line.

The accurate determination of the signal baseline is critical to performing efficient PSD. Errors in the baseline estimate will propagate to both the long and short integrals, and thus to the pulse shape parameter S. Improving the accuracy of baseline estimates can therefore lead to an improvement in PSD performance.

One method for improving baseline accuracy is to increase the number of samples N_b across which the baseline is calculated. However, increasing the number of samples included in each event will increase bandwidth requirements on readout electronics, as well as increasing the dead time of the digitizer and increasing the probability of pulse pile up. It is therefore important to determine how PSD performance varies with N_b.

Pulses from neutrons and gamma-rays from an Am-Be source were acquired at a SiPM over-voltage of 2.5 V. Events in the light output range of $L = 1.00 \pm 0.05$ MeV$_{\text{ee}}$ were selected, and a histogram of counts versus pulse shape parameter S was produced for various values of N_b between 75 and 1300 samples. These histograms were used to determine FoM in the $L = 1.00 \pm 0.05$ MeV$_{\text{ee}}$ range. Figure 5.18 shows FoM as a function N_b. As FoM was expected to increase asymptotically towards some optimal FoM with increasing N_b, FoM was fitted to an exponential decay function of the form

$$\text{FoM}(N_b) = F_0 - A\exp(-N_b/N_1), \tag{5.7}$$

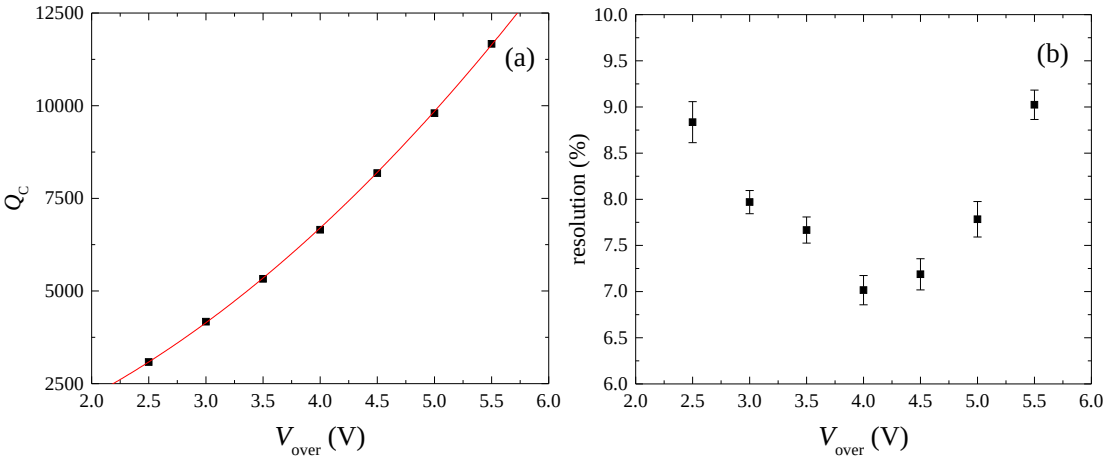

FIGURE 5.16: (a) Position of Compton edge Q_C versus SiPM over-voltage V_{over}, shown with fit to Equation 5.3. Error bars are not shown, as they are smaller than the symbols. (b) Resolution of the Compton edge versus SiPM over-voltage.

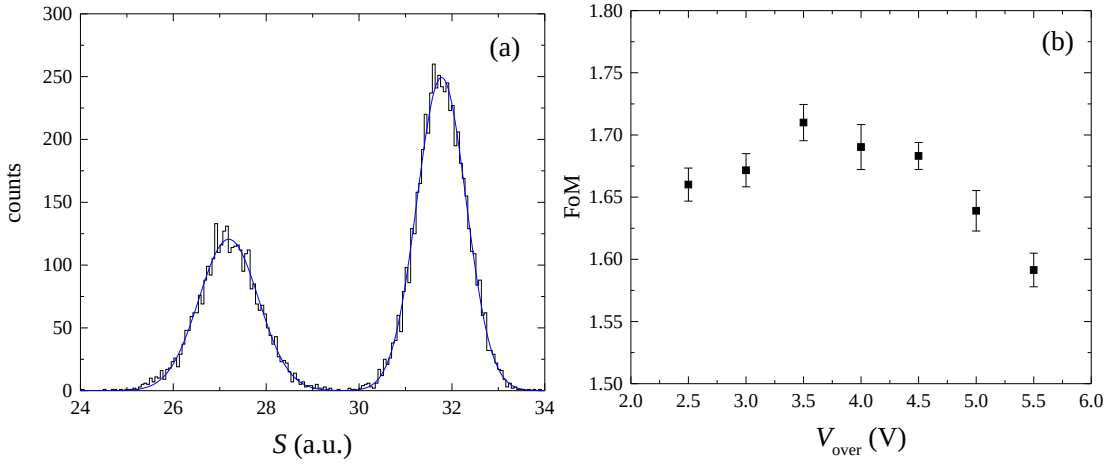

FIGURE 5.17: (a) Counts versus pulse shape parameter S for $L = 1.00 \pm 0.05$ MeV_{ee} events from an Am-Be source, with SiPMs running at V_{over} = 2.5 V. The data has been fitted to a double Gaussian function. The FoM in the figure is 1.66 ± 0.01, determined from the fit. (b) FoM versus SiPM over-voltage for 1.00 ± 0.05 MeV_{ee} neutron events from an Am-Be source.

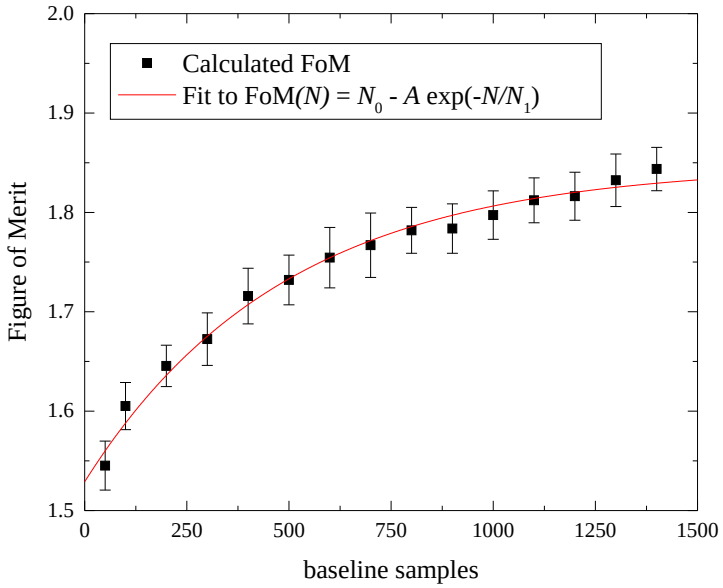

FIGURE 5.18: Figure of merit versus number of baseline samples N for 1.00 $\pm$ 0.05 MeV_{ee} neutron events from an Am-Be source, with SiPMs running at V_{over} = 2.5 V. The data has been fitted to an exponential decay function.

where F_0 is the optimal FoM as $N_b \to \infty$, while A and N_1 are exponential fit parameters. From the fit in Figure 5.18, $F_0 = 1.85 \pm 0.01$. The fit indicates that increasing N_b from 500 samples to 1000 samples would improve FoM by 4.0%, while a further increase of N_b to 1500 samples would result in an improvement of just 1.4%. It was therefore decided that $N_b = 1000$ would be sufficient in subsequent measurements. Assuming an integration time of $t_L = 1.5$ μs for SiPM-based devices, this means a minimum of 1750 samples are required for each event, resulting in a 3.5 μs dead time when using a 500 MSPS digitizer such as the DT5730.

PSD performance of the single-scintillator detector was compared to the PMT-based cylindrical EJ299-33 detector utilised in Chapter 4. Figure 5.19 shows distributions of events as a function of parameters L and S for two runs with the Am-Be source. While the two loci are more clearly separated in the plot for the SiPM-based detector, the gamma-ray locus is noticably thinner, particularly in the region of the 4.2 MeV_{ee} Compton edge. This arises due to the limited volume of the SiPM-based detector: The CSDA range of 4 MeV electrons in a typical plastic scintillator is approximately 20 mm [107]. Any Compton-scattered electrons in this energy range that are not precisely aligned with the 50 mm axis of the scintillator will almost certainly escape the thinner

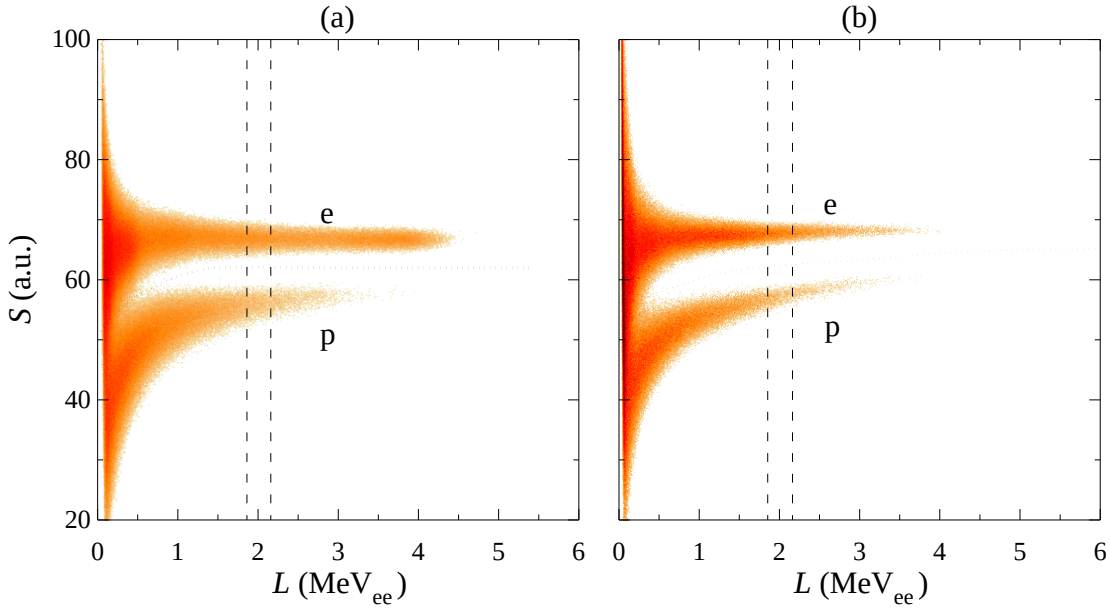

FIGURE 5.19: Counts as a function of light output parameter L and pulse shape parameter S for events induced by neutrons and gamma-rays from an Am-Be source in (a) an EJ299-33 scintillator coupled to a PMT and (b) the single-scintillator SiPM detector. Loci associated with recoiling protons (p) and electrons (e) are identified. The dotted lines indicate the cuts used to separate neutron and gamma-ray events and the dashed lines the cuts used to select events in the range $L = 1.9 - 2.1$ $\mathrm{MeV_{ee}}$.

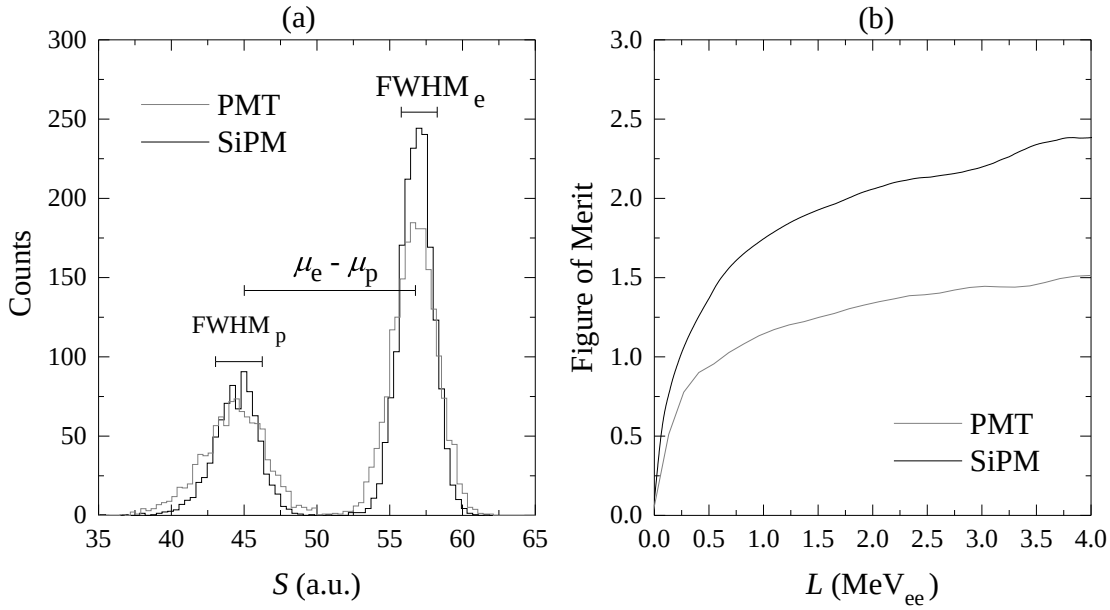

FIGURE 5.20: (a) Counts versus shape parameter S for events in the range of $L = 1.9 - 2.1$ $\mathrm{MeV_{ee}}$ from runs with the Am–Be source, for the PMT-based EJ299-33 detector and the single-scintillator SiPM detector. (b) Figure of merit versus L for the same detectors.

detector (with a cross-sectional area of 6×6 mm^2) before depositing their full energy. As the electron does not display a Bragg peak, the pulse shape produced by these escaping electrons does not differ from those that deposit their full energy in the detector, unlike escaping protons, as discussed in Section 3.4.4.

The dashed lines in Figure 5.19 indicate the cut used to select events in the range $L = 1.9$ to 2.1 MeV$_{ee}$, which are projected onto the S-axis in Figure 5.20(a). The FoM values for the distributions shown in Figure 5.19 are displayed in Figure 5.20(b). Short integration time t_S was chosen in order optimize the FoM, with a value of 35 ns for the PMT-based detector, and 75 ns for the SiPM-based detector. The FoM is considerably higher for the SiPM-based detector across the light output range, with a FoM of 1.0 at 0.25 MeV$_{ee}$. When comparing Figure 5.20(b) to Figure 4.12(b), one sees that, despite the poorer PSD performance of EJ299-33 described in Chapter 4, the FoM of the SiPM-based detector approaches that of the PMT-based EJ301 liquid scintillator detector.

A comparison between signals and pulse integrals measured with a conventional PMT and a MicroFC-60035, both coupled to an EJ299-33 plastic scintillator, is shown in Figure 5.21. While the rise times are comparable, the decay time of the SiPM is significantly longer, due to the microcell recovery time.

5.1.5 Simulations and energy spectrum unfolding

A simulation of the scintillator, together with light collection in the two SiPMs, was constructed using the GEANT4 Monte-Carlo package [128]. Light output relationships for electrons and protons were adapted from [39] and [18], while energy resolution parameters were chosen to fit measured spectra. The simulation included a correction for the effect of saturation in the SiPMs, due to the finite number of pixels. Figure 5.22(a) shows a comparison between the measured and simulated spectra of a ^{137}Cs gamma-ray calibration source. The discrepancy at lower pulse height is associated with gamma-rays scattered off surrounding materials before entering the detector, an effect not incorporated in the simulation. A neutron response matrix was created by simulating the response of the detector to monoenergetic neutrons up to 15 MeV, in steps of 0.2 MeV. An illustrative sample of simulated line-shapes is shown in Figure 5.22(b).

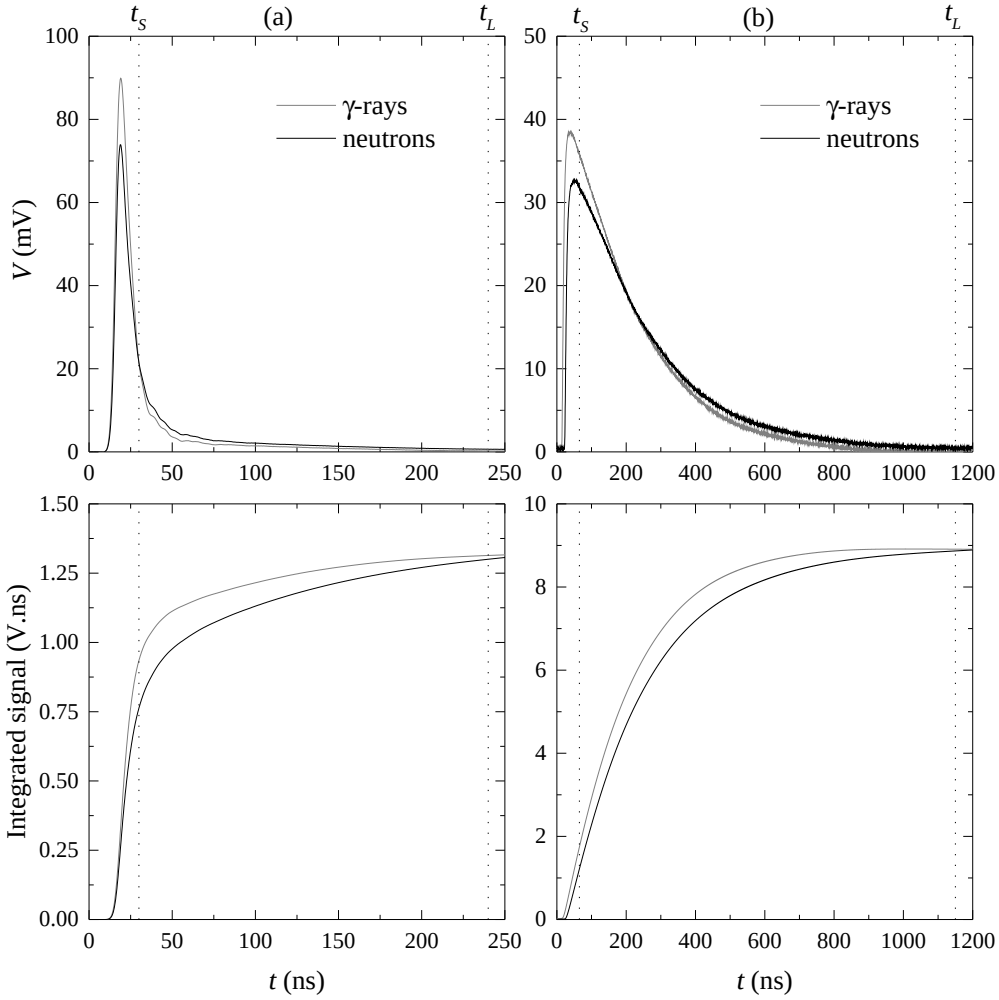

FIGURE 5.21: Digitized pulses (above) and pulse integrals (below) for events arising from neutron and gamma-ray interactions in the EJ299-33 scintillators coupled to (a) a PMT and (b) a MicroFC-60035 SiPM. Typical integration times t_S and t_L are indicated.

In order to evaluate the capability of the detector as a neutron spectrometer, spectrum unfolding was performed using the HEPRO package [21], [111], as described in Section 4.1.2. An Am-Be neutron source was utilised, and the measured light output spectrum was unfolded using the simulated response matrix. The unfolded energy spectrum is compared with the reference spectrum [96] in Figure 5.23(a). The unfolded spectrum matches the reference spectrum very well, with deviations below 3 MeV most likely due to the interaction of the detector with neutrons scattered off surrounding material, or due to imperfect PSD performance. Figure 5.23(b) shows the measured and re-folded light output spectra. The two spectra are in excellent agreement across the relevant light output range, with a coefficient of determination of $R^2 = 0.998$.

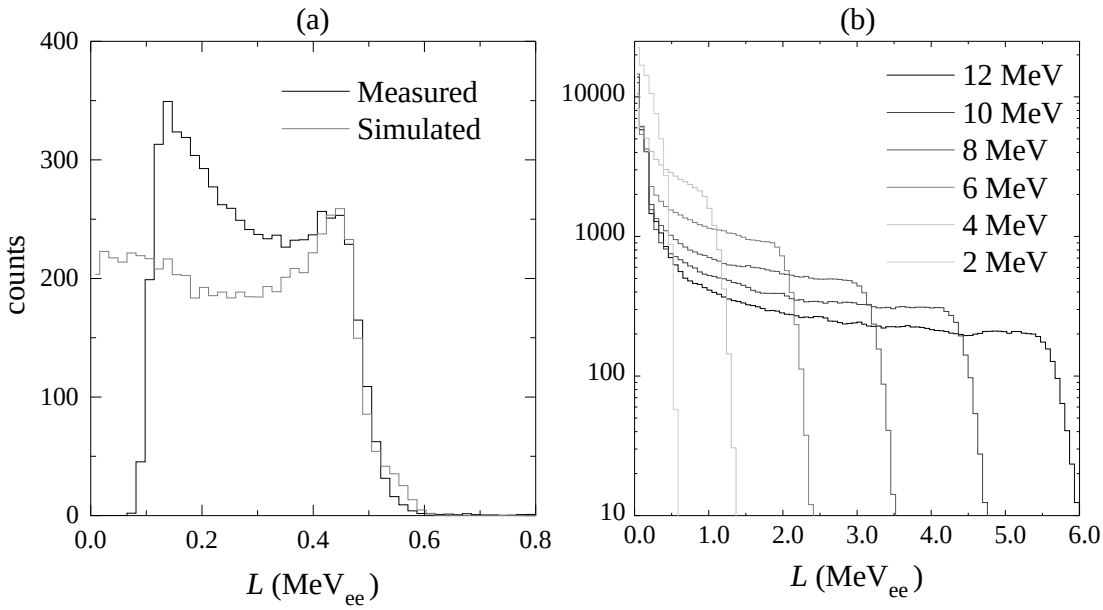

FIGURE 5.22: (a) Light output spectrum for 662 keV gamma-rays emitted from a ^{137}Cs source placed 30 cm from the detector, compared with simulated light output spectrum from Geant4. (b) Simulated light output spectra for mono-energetic neutrons between 2 and 12 MeV.

Unfolding measurements were also performed using the D-T neutron generator, which produces neutrons with characteristic energies of 14.1 MeV and 2.5 MeV, from D-T and D-D reactions respectively. The detector was placed in the polyethylene cave described in Section 3.4.3, 50 cm from the D-T generator. Measurements were taking with and without the placement of a 10 cm thick block of polyethylene between the generator and the detector. Figure 5.24(a) shows the unfolded energy spectra for the unshielded and shielded measurements. Peaks due to the detection of 2.5 MeV and 14.1 MeV neutrons can be clearly seen. However, there is a significant continuum below 14 MeV, due to scattering off the surrounding geometry. The polyethylene block suppresses a very small fraction of 14.1 MeV neutrons, while suppressing a larger fraction of 2.5 MeV neutrons. Figure 5.24(b) shows the measured and re-folded light output spectra for unshielded measurements. The two spectra are in excellent agreement across the relevant light output range, with a coefficient of determination of $R^2 = 0.996$.

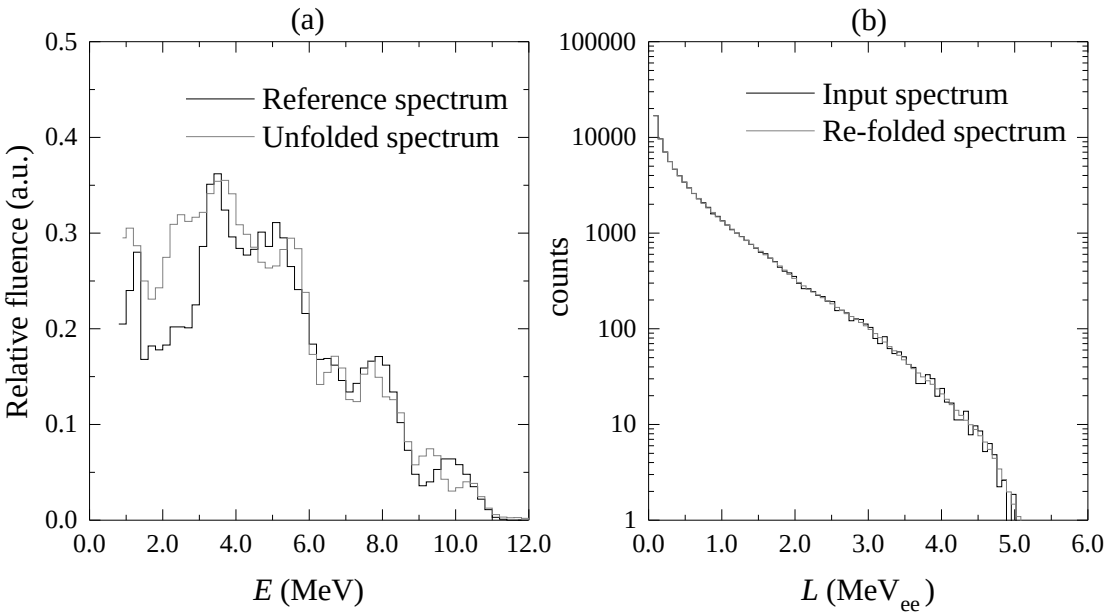

FIGURE 5.23: (a) Unfolded neutron energy spectrum for neutrons from an Am-Be source placed 50 cm from the detector, compared to the reference spectrum [96]. (b) Re-folded light output spectrum, compared to the measured light output spectrum for neutrons from an Am-Be source.

5.2 Direction-sensitive multi-scintillator device

5.2.1 Device description

A multi-scintillator device was developed as an extension to the prototype described in Section 5.1. The device consists of four square prisms of EJ299-33 plastic scintillator ($6\times6\times50$ mm^3), each coupled to two SensL MicroFC SiPMs, mounted on MK-II PCBs. A high-density (0.95 g/cm^3) polyethylene (HDPE) filler in the shape of an extruded cross lies between the four scintillators. A schematic of the device is shown in Figure 5.25(a). A 3D-printed detector housing was constructed to hold the PCBs and scintillators in place. A digital rendering of the detector housing is shown in Figure 5.25(b). Figure 5.26 shows the PCBs in the detector housing, as well as the assembled detector with a single scintillator installed. Initial designs used filler dimensions of 11.5 mm (cross thickness), 44 mm (cross width), 50 mm (extrusion length) and a distance of 28 mm between SiPMs. However, an exploration of alternative geometries through a Geant4-based simulation (see Section 5.2.2) lead to a revised filler thickness of 19 mm.

The SiPMs were powered by a custom-built power supply, capable of supplying

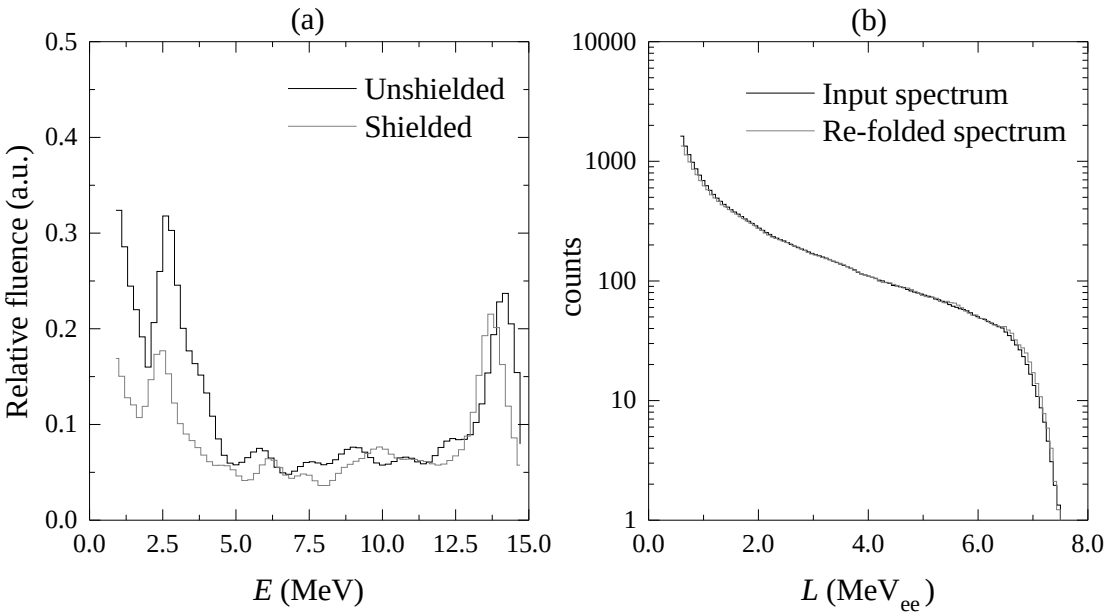

FIGURE 5.24: (a) Unfolded neutron energy spectrum for neutrons from the D-T neutron generator placed 50 cm from the detector, compared to the unfolded spectrum when shielded by 10 cm of polyethylene. (b) Re-folded light output spectrum, compared to the measured light output spectrum for neutrons from the D-T neutron generator.

8 independent bias voltages between 24 V and 32 V, adjustable through the use of an on-board Arduino microcontroller. The power supply includes an LM35-based temperature sensor, and bias voltages are automatically adjusted based on temperature, in order to maintain a constant over-voltage. The use of a power supply capable of independent bias voltages mitigates the effect of variation in breakdown voltage across the 8 SiPMs. The power supply is shown in Figure 5.27.

The multi-scintillator device has two modes of operation:

- **Spectroscopic orientation:** when the direction of incident neutrons lies roughly parallel to the lengthwise axis of the scintillators, it is capable of providing spectroscopic information through the unfolding of light output spectra, in an identical manner to the single-scintillator device.

- **Direction-sensitive orientation:** when the direction of incident neutrons lies in the plane perpendicular to the lengthwise axis of the scintillators, it is capable of estimating the direction of incoming radiation for a single source, based on a comparison between the counts observed in the four scintillators.

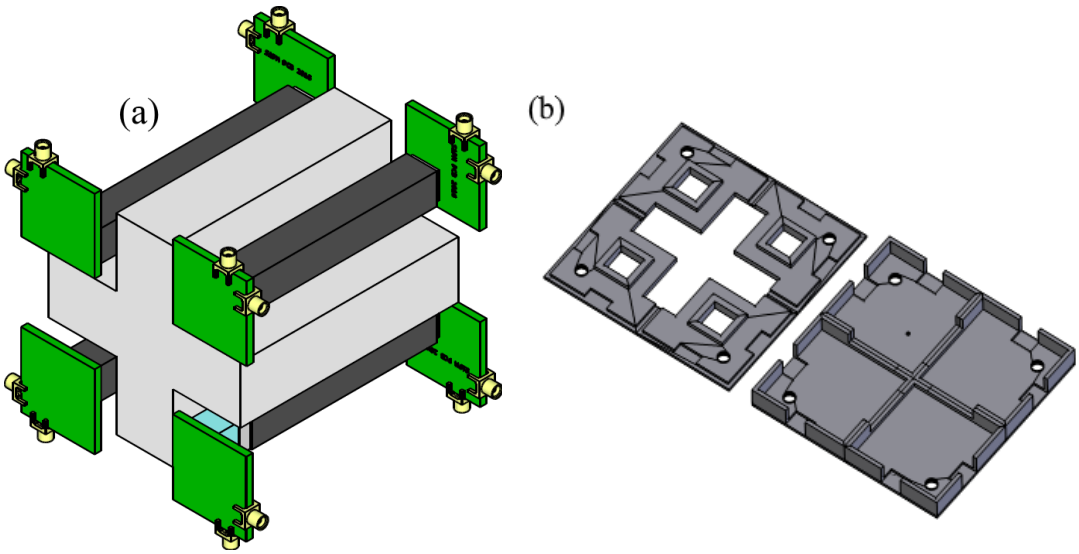

FIGURE 5.25: (left) Schematic of multi-scintillator device, with two PCB-mounted SensL MicroFC SiPMs coupled to each scintillator. The HDPE filler in the diagram has dimensions of 11.5 mm (thickness), 44 mm (width) and 50 mm (length). (b) Digital Rendering of detector housing, designed to keep the scintillators, SiPMs and HDPE filler held in place.

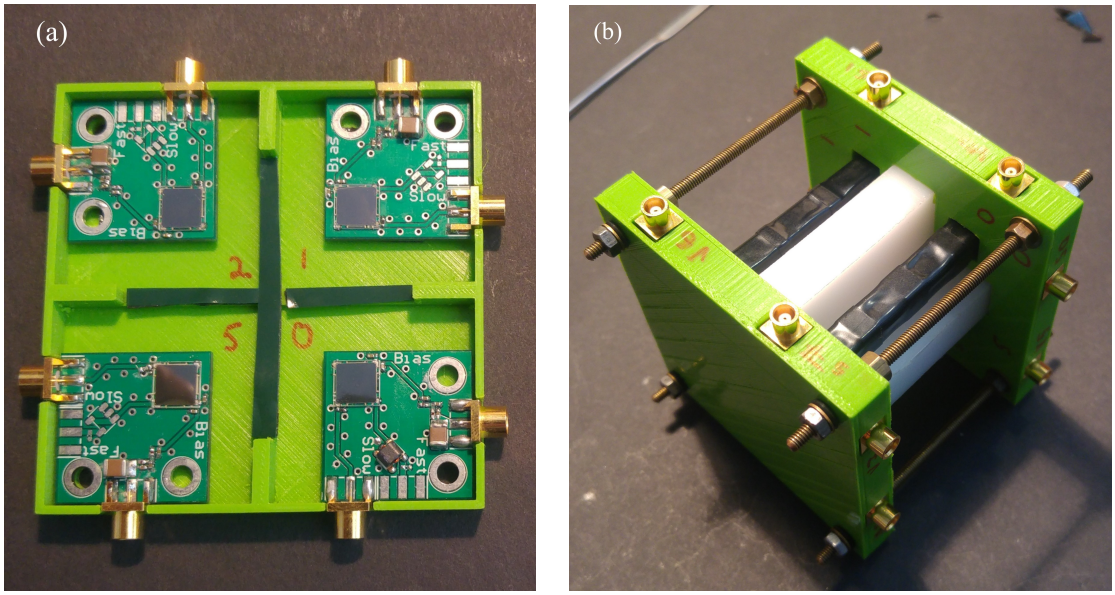

FIGURE 5.26: (a) PCBs placed in 3D-printed detector housing. (b) Assembled detector.

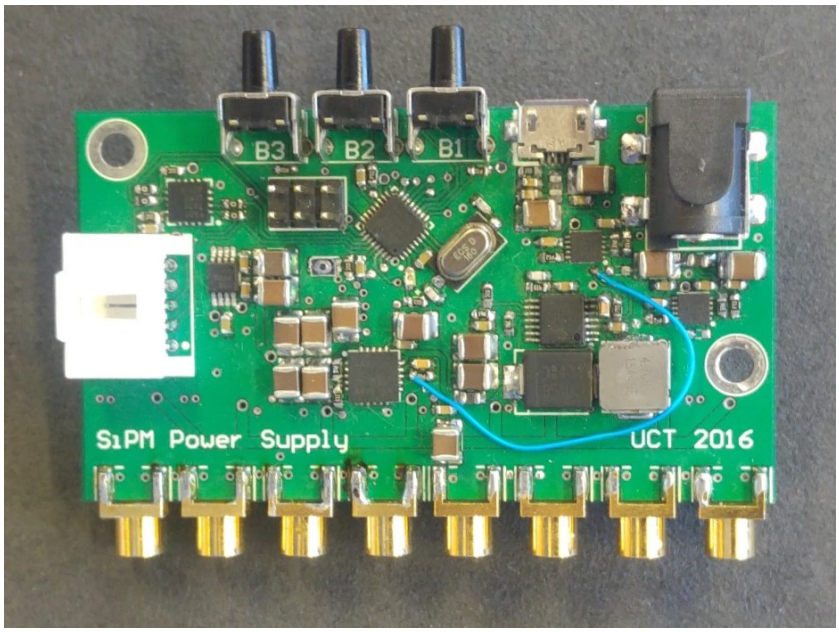

FIGURE 5.27: 8 channel custom-built power supply used for the multi-scintillator detector.

Figure 5.28(a) shows a schematic of the device in direction-sensitive orientation. The four scintillator cells are referred to by their position relative to the HDPE filler: left-top (LT), right-top (RT), left-bottom (LB) and right-bottom (RB). The angle θ represents the angle between incident neutrons and the vertical axis. In the diagram, the neutrons are assumed to be shaped as a beam, with a direction parallel to the blue arrow, and a beam area larger than the cross-sectional area of the device. This assumption is valid for sufficiently distant isotropic sources.

For an incident angle of $\theta = 0°$ (shown in Figure 5.28(b)), the number of neutrons incident on scintillator cells LT and RT will be approximately equal. A fraction of these neutrons will be scattered in the scintillators, while the majority will continue into the HDPE filler. A fraction of these remaining neutrons will be scattered in the HDPE filler, with the remaining neutrons passing through to cells LB and RB. The bottom cells are therefore partially shielded from incident neutrons by the HDPE filler and the top cells, resulting in lower count rates compared to those of the top cells.

For an incident angle of $\theta = 45°$ (shown in Figure 5.28(c)), the count rate in cell RT will be highest, while the count rate in cell LB will be lowest, due to shielding from the HDPE filler and the LT cell. Count rates in cells LT and RB will be approximately equal, and slightly lower than that of cell RT, due to slight shielding from the HDPE filler.

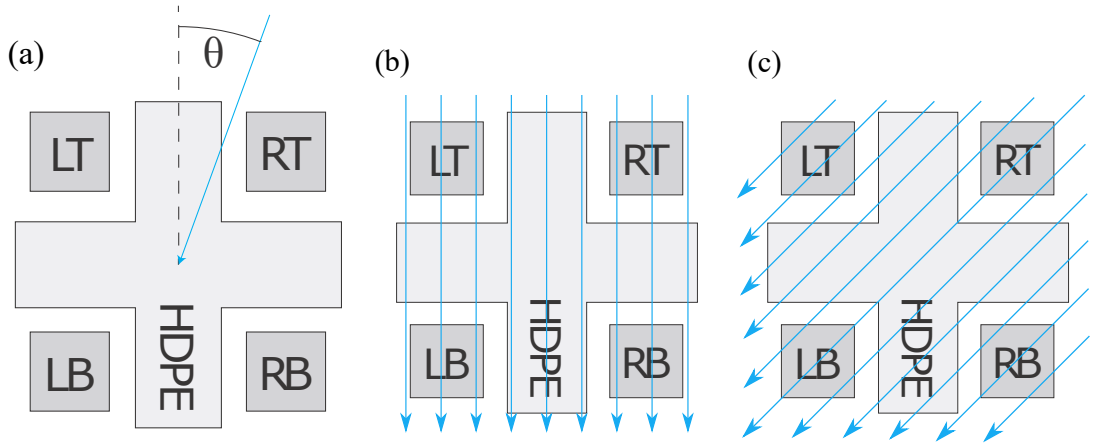

FIGURE 5.28: (a) Schematic of device in direction-sensitive orientation. The angle between the incident neutron beam direction and the vertical axis is shown as θ. Beams of neutrons incident on the multi-scintillator detector at incident angles of $\theta = 0°$ and $\theta = 45°$ are shown in (b) and (c) respectively.

In spectroscopic orientation, the count rates in each cell will be approximately equal, as no shielding occurs.

An estimate of the direction of the source can be calculated by determining the reconstructed position $\vec{r}_{\text{rec}}$ of the source, from an average of the counts in each cell, weighted by the normalised positions of each cell:

$$\vec{r}_{\text{rec}} = \frac{LT\langle -1,1\rangle + RT\langle 1,1\rangle + LB\langle -1,-1\rangle + RB\langle 1,-1\rangle}{\sqrt{2}(LT + RT + LB + RB)}, \tag{5.8}$$

where LT, RT, LB and RB are the counts recorded in the respective scintillator cells. From the reconstructed position, the incident angle can then be estimated as

$$\theta_{\text{rec}} = -\text{atan2}(x_{\text{rec}}, y_{\text{rec}}), \tag{5.9}$$

where x_{rec} and y_{rec} are the x and y components of $\vec{r}_{\text{rec}}$ respectively.

5.2.2 Directional simulations

In order to determine the behaviour of the device in direction-sensitive orientation, the GEANT4-based simulation described in Section 5.1.5 was extended to support multiple scintillator cells. A digital rendering of the geometry constructed in the simulation is shown in Figure 5.29.

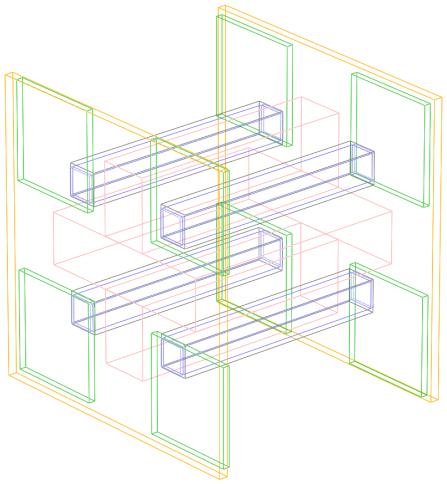

FIGURE 5.29: Geometry used in Geant4 simulation, showing scintillators, wrapping, SiPMs, PCBs and housing.

TABLE 5.3: Counts of each scintillator above 0.1 MeV_{ee} , relative to the total counts for all scintillators, for simulated neutrons emitted isotropically by an Am-Be source 50 cm from the detector. The source was placed in front of the detector (spectroscopic configuration), above the detector (θ = 0°) and at a diagonal (θ = 45°).

	Relative counts (%)		
Cell	Spectroscopic	$\theta = 0°$	$\theta = 45°$
LT	25.0 ± 0.1	29.2 ± 0.1	26.9 ± 0.1
RT	25.1 ± 0.1	29.1 ± 0.1	28.3 ± 0.2
LB	24.9 ± 0.1	20.9 ± 0.1	18.1 ± 0.1
RB	25.0 ± 0.1	20.8 ± 0.1	26.7 ± 0.1

Figure 5.30 shows simulated counts versus light output L, for neutrons emitted isotropically by an Am-Be source placed 50 cm from the centre of the detector. In spectroscopic orientation, shown in Figure 5.30(a), the spectra are approximately equal across the light output range. In directional orientations, shown for θ = 0° and θ = 45° in Figure 5.30(b) and (c) respectively, significant differences in the individual light output spectra are visible, particularly at lower light output. In order to reliably compare simulated results with experimental measurements, a cut of $L > 0.1$ MeV_{ee} was used in subsequent calculations. 40 million neutron events were generated for each simulation setup, resulting in approximately 50 000 detected events above 0.1 MeV_{ee} per cell.

Differences between spectra are more readily visible if the counts are summed

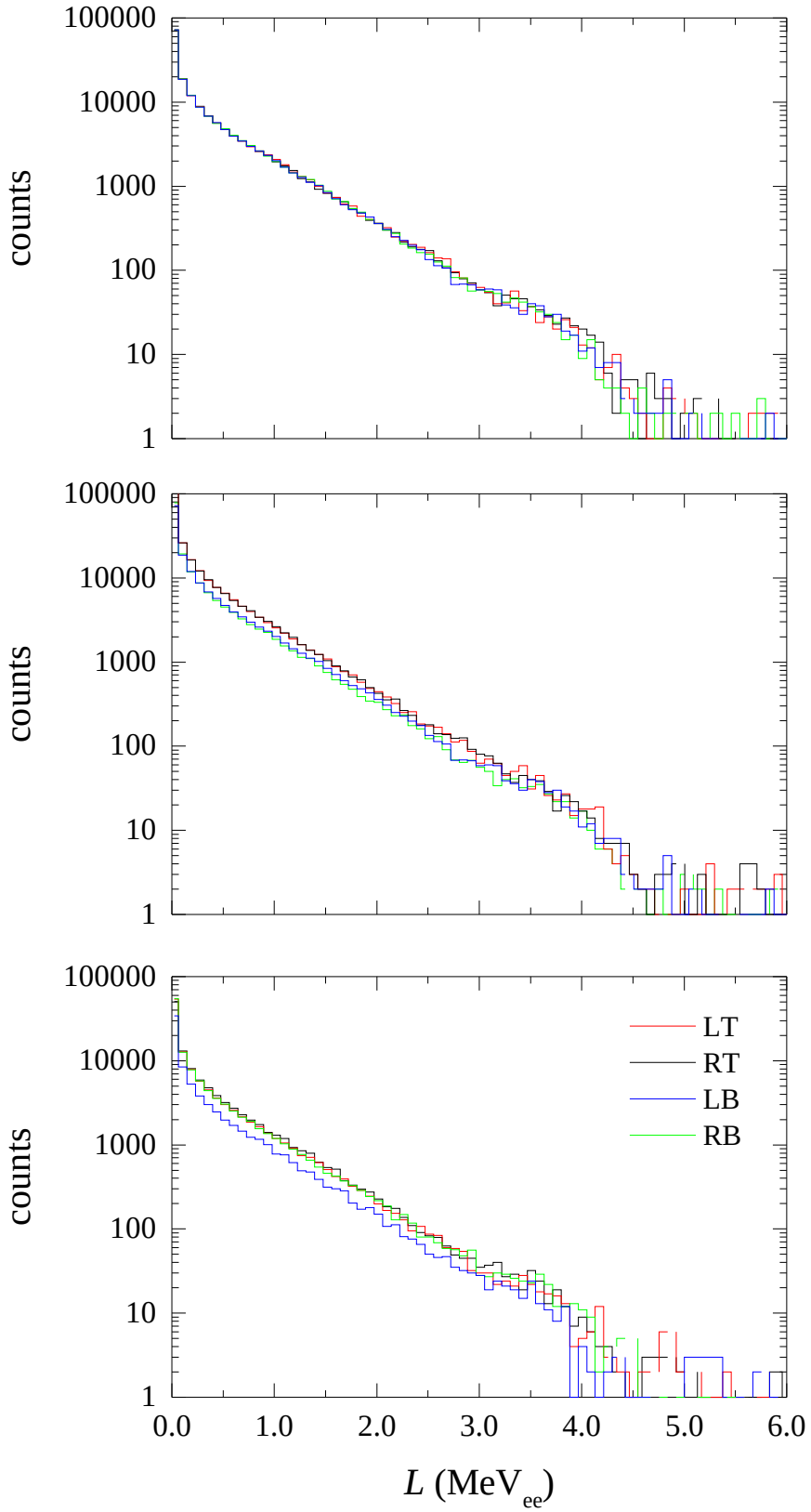

FIGURE 5.30: Simulated light out spectra of each scintillator for neutrons emitted isotropically by an Am-Be source 50 cm from the detector. The source was placed (a) in front of the detector (spectroscopic orientation), (b) above the detector ($\theta = 0°$) and (c) at a diagonal ($\theta = 45°$).

across a wide light output range. Table 5.31 shows relative counts above 0.1 MeV_{ee} for each scintillator cell (calculated as the total counts for each cell divided by the total counts for all cells) for spectroscopic orientation, θ = 0° and θ = 45°.

Figure 5.31 shows relative counts above 0.1 MeV_{ee} for each scintillator cell versus detector angle θ, using (a) the default HPDE filler geometry (thickness and width of 11.5 mm and 44 mm respectively), (b) a 60 mm filler width and (c) a 19 mm filler thickness. The oscillatory behaviour seen in Figure 5.31(a) and (b) arises from the presence of an air gap between the scintillators and the HDPE filler. Reducing this gap, as shown in Figure 5.31(c), results in a significant reduction in the amplitude of these oscillations.

Figure 5.32 shows reconstructed x and y coordinates, according to Equation 5.8, for neutrons emitted isotropically by an Am-Be source 50 cm from the detector for each geometry tested, for the range θ = 0°(top) to θ = 180°(bottom). In order for the direction to be reliably reconstructed, the reconstructed coordinates should ideally follow a circular path, shown in Figure 5.32 as the dashed line. Both the default geometry and the wider geometry show significant deviations from a circular path, due to the air gap described above. The $t = 19$ mm geometry closely follows a circular path of $x_{\text{rec}}^2 + y_{\text{rec}}^2 = 0.15$.

Figure 5.33(a) shows reconstructed angle (θ_{rec}) versus detector angle θ, for neutrons emitted isotropically by an Am-Be source 50 cm from the detector for both the default geometry and the wider geometry ($w = 60$ mm). The oscillatory behaviour seen in Figures 5.31 and 5.32 gives rise to oscillations in the reconstructed angles in the $\theta = 25°$ and $\theta = 65°$ region for both geometries. In addition, θ_{rec} is roughly constant in the $\theta < 10°$ region. These issues prevent the construction of an inverse function to determine θ from θ_{rec}, which is critical to the accurate estimation of direction for experimental data.

Figure 5.33(b) shows reconstructed angle (θ_{rec}) versus detector angle θ, for the default geometry and the thicker geometry ($t = 19$ mm). The thicker geometry closely follows the line of $\theta_{\text{rec}} = \theta$, and $\theta_{\text{rec}}(\theta)$ is a one-to-one function, and therefore invertible, allowing the construction of an inverse function to determine θ from θ_{rec}. The thicker geometry is therefore highly preferable to the default geometry in terms of direction sensitivity.

Figure 5.34 shows reconstructed angle (θ_{rec}) versus detector angle θ, for the thicker

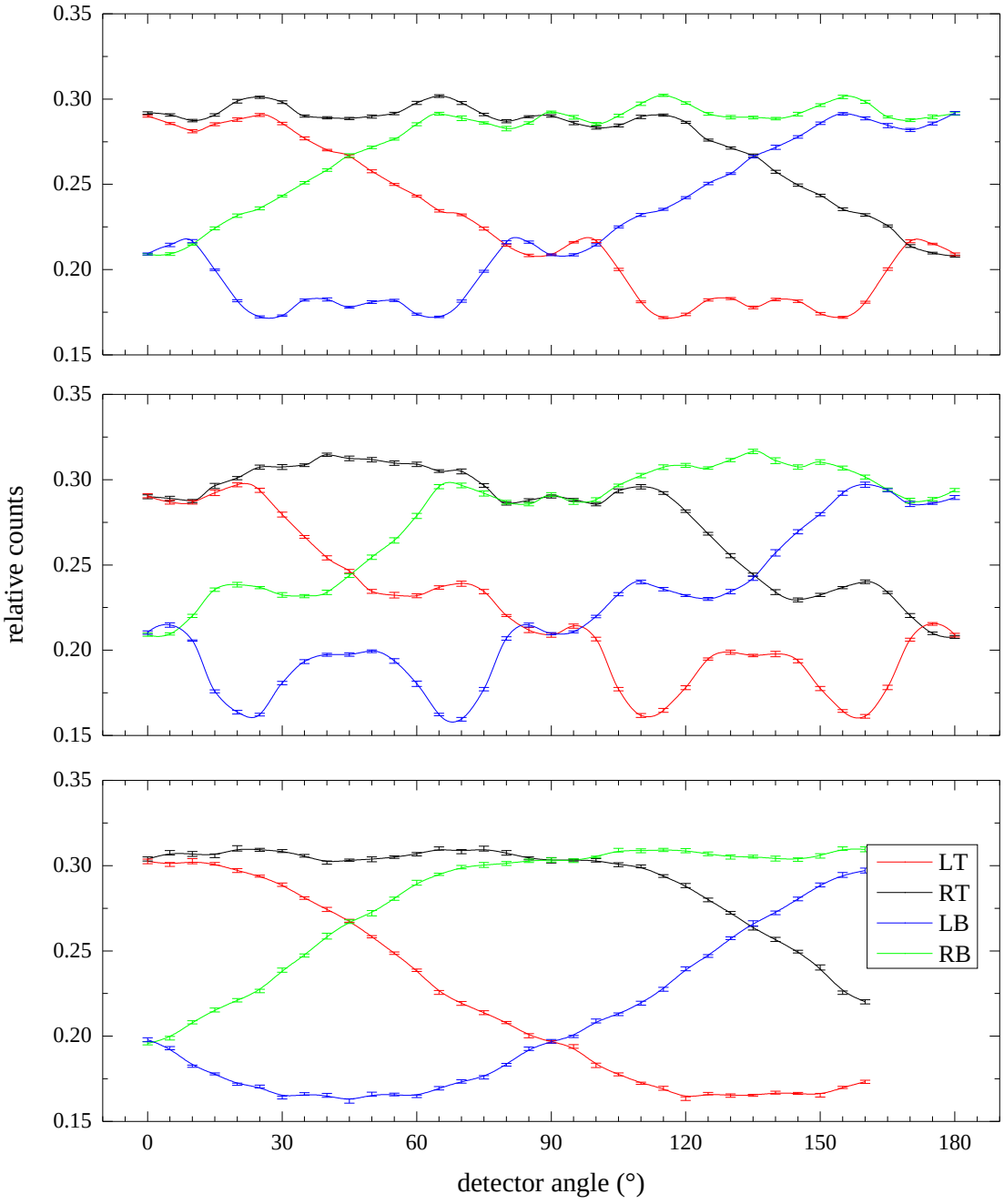

FIGURE 5.31: Relative counts above 0.1 MeV_{ee} versus detector angle (θ) for neutrons emitted isotropically by an Am-Be source 50 cm from the detector, using (a) the default HPDE filler geometry (thickness and width of 11.5 mm and 44 mm respectively), (b) 11.5 mm thickness and 60 mm width and (c) 19 mm thickness and 44 mm width.

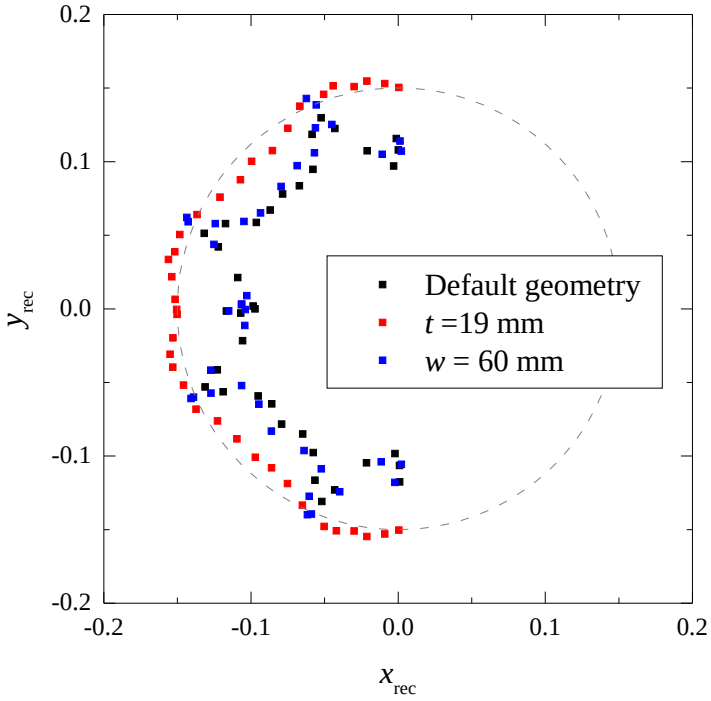

FIGURE 5.32: Reconstructed x and y coordinates for neutrons emitted isotropically by an Am-Be source 50 cm from the detector, shown for each geometry tested, for the range $\theta = 0°$(top) to $\theta = 180°$(bottom). Error bars are not shown, as they are smaller than the symbols. The dashed line shows the circle of $x_{\text{rec}}^2 + y_{\text{rec}}^2 = 0.15$.

geometry, for neutrons emitted from both an isotropic Am-Be source 50 cm from the detector, and a beam source, mimicking an isotropic source infinitely far from the detector. No significant difference arises as a result of the change in source, confirming that the angular reconstruction is independent of source distance.

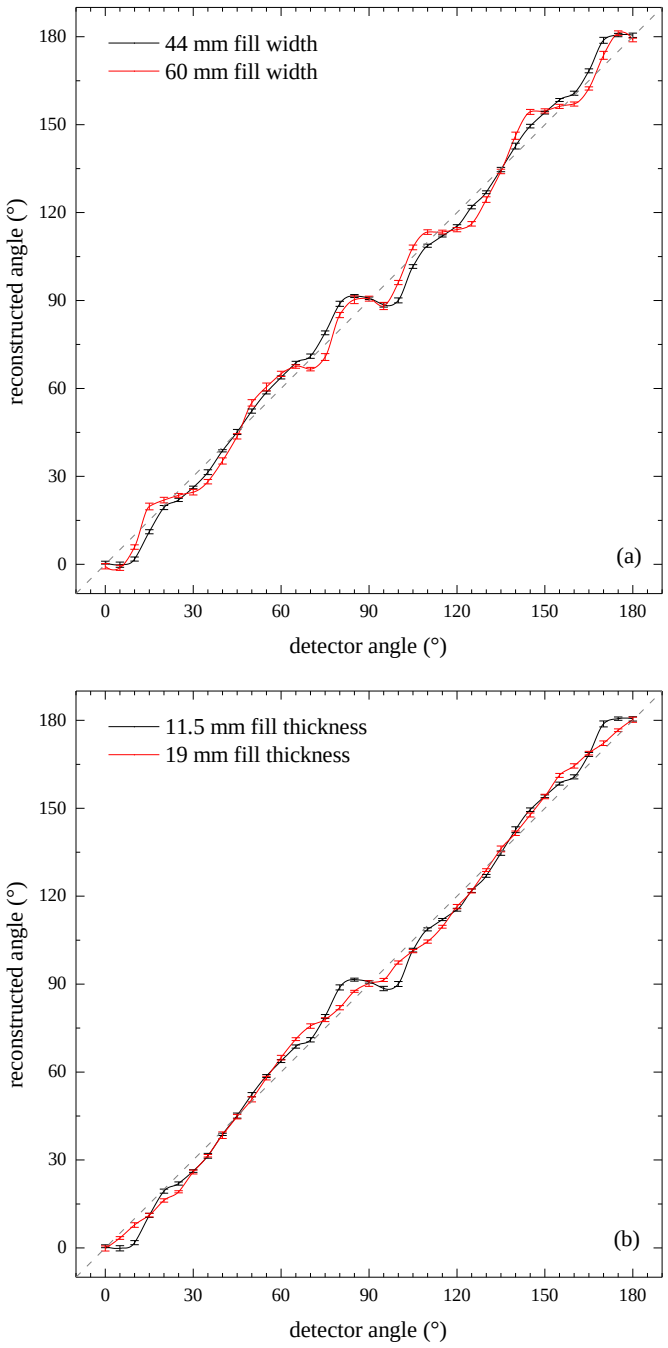

FIGURE 5.33: Reconstructed angle (θ_{rec}), for neutrons emitted isotropically by an Am-Be source 50 cm from the detector, showing a comparison between (a) the default geometry and a wider HDPE filler, and (b) the default geometry and a thicker HDPE filler. The dashed lines show $\theta_{\mathrm{rec}} = \theta$.

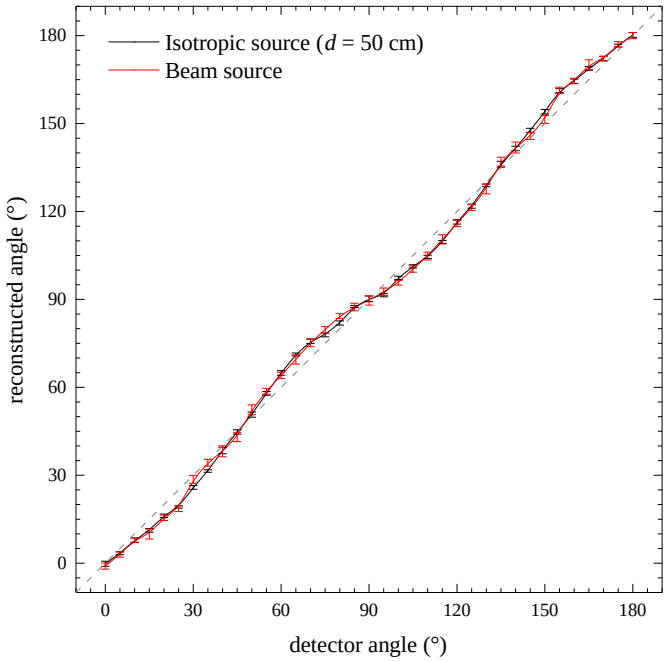

FIGURE 5.34: Reconstructed angle (θ_{rec}), for neutrons from an isotropic Am-Be source 50 cm from the detector, and an Am-Be beam source using the thicker HDPE filler geometry (thickness and width of 19 mm and 44 mm respectively). The dashed line shows $\theta_{\mathrm{rec}} = \theta$.

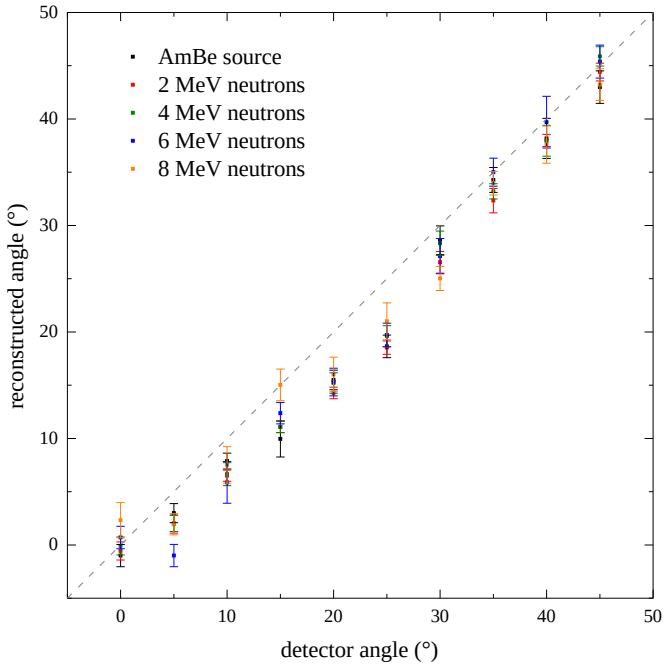

FIGURE 5.35: Reconstructed angle (θ_{rec}), for neutrons from an Am-Be beam source and mono-energetic neutron beam sources (E_n = 2.0, 4.0, 6.0, 8.0 and 10.0 MeV) using the thicker HDPE filler geometry (thickness and width of 19 mm and 44 mm respectively). The dashed line shows $\theta_{\mathrm{rec}} = \theta$.

TABLE 5.4: Counts of each scintillator above 0.25 MeV_{ee} , relative to the total counts for all scintillators, for measured neutrons emitted isotropically by an Am-Be source 50 cm from the detector. The source was placed in front of the detector (spectroscopic configuration), above the detector (θ = 0°), and at a diagonal (θ = 45°).

	Relative counts (%)		
Cell	Spectroscopic	$\theta = 0°$	$\theta = 45°$
LT	24.7 ± 0.3	29.2 ± 0.4	26.3 ± 0.3
RT	24.7 ± 0.4	29.4 ± 0.4	28.8 ± 0.4
LB	25.6 ± 0.3	20.9 ± 0.3	18.3 ± 0.3
RB	25.0 ± 0.3	20.6 ± 0.4	26.7 ± 0.3

5.3 Experimental measurements

In order to verify the simulated results, experimental measurements were taken using an Am-Be, using the default geometry. Due to the presence of a large number of gamma-rays emitted from the Am-Be source, PSD was employed to discard events arising from gamma-ray interactions. As shown in Figure 5.20, the SiPM-based detector has a FoM in the region of 1.0 at 0.25 MeV_{ee} . Events with light output below 0.25 MeV_{ee} were discarded.

Figure 5.36 shows measured counts versus light output L, for neutrons emitted isotropically by an Am-Be source placed 50 cm from the centre of the detector. In spectroscopic orientation, shown in Figure 5.36(a), the spectra are approximately equal across the light output range. In directional orientations, shown for θ = 0° and θ = 45° in Figure 5.36(b) and (c) respectively, significant differences in the individual light output spectra are visible, particularly at lower light output. This behaviour closely matches the simulated results, shown in Figure 5.30.

Table 5.4 shows relative counts above 0.25 MeV_{ee} for each scintillator cell (calculated as the total counts for each cell divided by the total counts for all cells) for spectroscopic orientation, θ = 0° and θ = 45°. Some variation between the cells is observed in the spectroscopic configuration, possibly due to variations in each scintillator's efficiency, or due to imperfect PSD. These variations are consistent in the θ = 0° and θ = 45° orientations. The results of Table 5.4 closely match the simulated relative counts, as shown in Table 5.3.

In addition to measurements performed with an Am-Be source, light output spectra

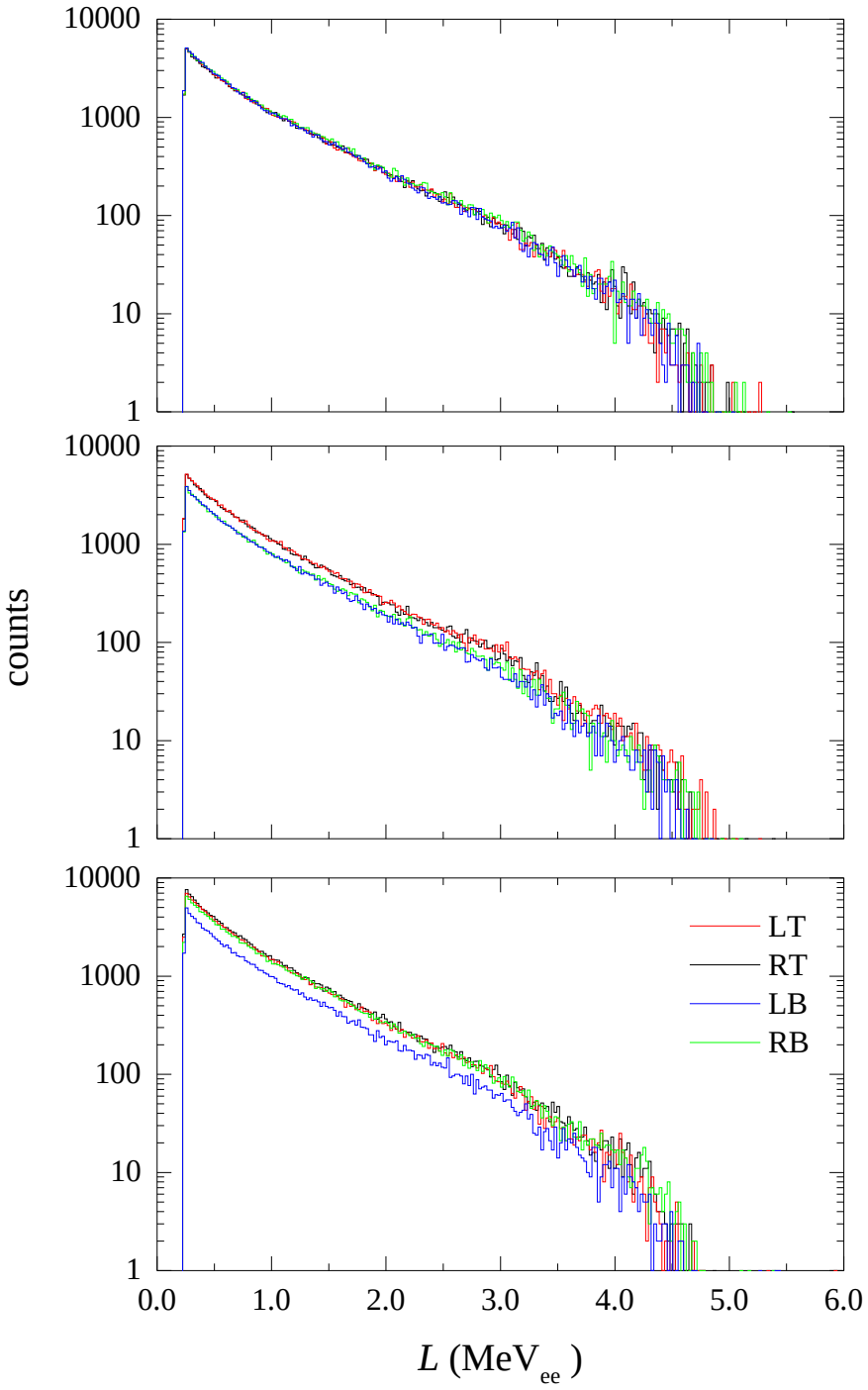

FIGURE 5.36: Measured light out spectra of each scintillator for neutrons emitted isotropically by an Am-Be source 50 cm from the detector. The source was placed (a) in front of the detector (spectroscopic orientation), (b) above the detector ($\theta = 0°$), and (c) at a diagonal ($\theta = 45°$).

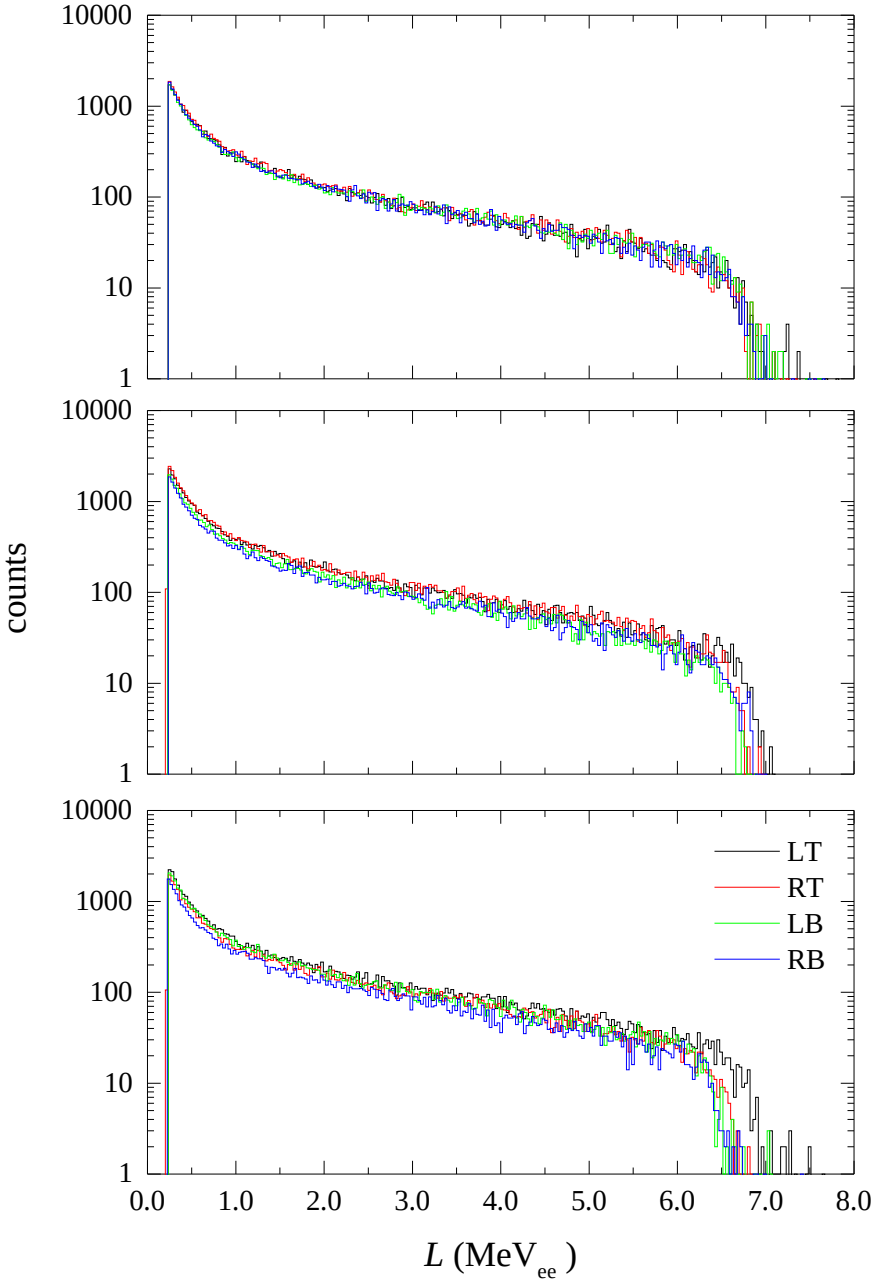

FIGURE 5.37: Measured light out spectra of each scintillator for neutrons emitted isotropically by the D-T neutron generator, placed 50 cm from the detector. The source was placed (a) in front of the detector (spectroscopic orientation), (b) above the detector ($\theta = 0°$) and (c) at a diagonal ($\theta = 45°$).

were measured for 14.1 MeV neutrons emitted from the D-T neutron generator. Figure 5.37 shows measured counts versus light output L, for neutrons emitted isotropically by the D-T neutron generator placed 50 cm from the centre of the detector, in both spectroscopic configuration and for $\theta = 0°$ and $\theta = 45°$ orientations. Differences between spectra are much smaller than those shown in Figure 5.36, due to the higher neutron energy.

5.4 Discussion

A compact neutron detector, consisting of two SiPMs coupled to a plastic scintillator, demonstrates significant improvements in PSD performance to a conventional PMT-based scintillator detector. The ability of the single-scintillator prototype to act as a neutron energy spectrometer was demonstrated by unfolding energy spectra from an Am-Be source, as well as a D-T neutron generator, with and without polyethylene shielding. For both sources, the unfolded spectrum closely matched the expected spectrum.

The extension of the prototype to a multi-scintillator detector adds a number of possible applications. The ability to determine source direction to within approximately 5°, regardless of source distance, is a particularly novel feature, especially when paired with a mobile DAQ.

Chapter 6

Conclusion

6.1 Summary

A software-based digital DAQ was developed, with support for a number of commercial high speed digitizers, such as the CAEN Vx1761 and DT5730. The DAQ includes an embedded JavaScript interpreter to allow for flexible signal processing and analysis. Various digital pulse processing algorithms were implemented and compared. First results of digital PSD at energies of up to 100 MeV were presented, and it was found that a carefully optimised implementation of the digital charge comparison algorithm was sufficient across a wide energy range. Neutron energy spectra calculated from time of flight measurements using the digital DAQ agreed previous measurements using analogue electronics to within 5%. The digital DAQ will be adapted to suit metrology requirements at iThemba LABS, and future experiments will make use of the digital DAQ rather than the existing analogue setup.

The response of EJ299-33 plastic scintillator was measured for neutrons over a wide energy range, and these measurements were used to determine a detector response matrix. The use of EJ299-33 for neutron spectrometry was demonstrated by unfolding light output spectra over the 10-100 MeV energy range. When compared to the standard EJ301 liquid scintillator, the EJ299-33 plastic scintillator produced poorer unfolding results, due to inferior light output resolution. The EJ299-33 detector displayed good PSD capability across a wide energy range, albeit inferior to that of the EJ301 detector. A Geant4-based Monte-Carlo simulation of the pulse shapes produced by EJ299-33 scintillator has been developed, in order to investigate the effect of wrapping and geometry on light collection and PSD capability.

A compact neutron detector was constructed, consisting of two SensL MicroFC-60035 SiPMs coupled to a $6 \times 6 \times 50$ mm^3 EJ299-33 plastic scintillator. Significant improvements to PSD capability were observed, when compared to a PMT-based detector. Its use as a spectrometer was demonstrated by unfolding energy spectra from an Am-Be source, as well as a D-T neutron generator, using a Monte-Carlo generated response matrix. A multi-scintillator detector was constructed, consisting of four $6 \times 6 \times 50$ mm^3 EJ299-33 scintillators, each coupled to two SiPMs, and an HDPE shield. The detector is designed to operate in two orientations, with spectroscopic orientation providing light output measurements that can be unfolded to determine incident neutron energy spectra, while other orientations provide directional information, by comparing count rates between scintillator cells. The ability to determine source direction to within approximately 5° was demonstrated using an Am-Be source.

6.2 Limitations and future work

While a functional proof-of-principle compact neutron spectrometer was developed, there are currently a number of factors limiting its application, and development is ongoing. A spectrometer capable of providing directional information for neutrons up to approximately 10 MeV has a number of applications in radiation safety and monitoring. However, for directional measurements at higher energies, further investigation is required.

The current approach of generating a response matrix through Monte-Carlo simulations is not extendible to energies above 20 MeV, due to limited inelastic neutron interaction cross-section data at higher energies. Instead, measurements of the prototype spectrometers' response to high energy neutrons will be performed at the iThemba LABS facility. An elongated scintillator design, with dimensions $6 \times 6 \times 150$ mm^3, will be tested at energies up to 100 MeV.

Measurements of directional sensitivity will also be performed at higher energies. However, the CSDA range of 100 MeV protons in plastic scintillator is approximately 8 cm, limiting the applicability of the approach described in Section 5.2.2. An alternative approach, based on comparing pulse heights and timing between scintillators, will be

tested. As high energy protons produced in the scintillator will likely travel through the HDPE shield and into neighbouring scintillators, many events will consist of pulses recorded in multiple scintillators.

The current prototype spectrometer makes use of EJ299-33 scintillator. Recently, a new revision of plastic scintillator, EJ-299-33A, has been developed, showing improved homogeneity. Additional tests on the improvements to PSD performance and unfolding capability of detectors based on the newer scintillator will be performed.

Currently implemented calibration techniques require a number of standard gamma-ray sources, and measurements of breakdown voltages across a wide temperature range. The use of a pulsed LED source built into the prototype detector for automatic calibration and continuous stabilisation is currently being investigated. A small pulsed LED can be placed adjacent to each scintillator, underneath the reflective wrapping, and varying the pulse width allows for careful calibration over a range of light intensities. This is particularly important for SiPM measurements, due to the effect of saturation for high light intensities.

A compact and battery-powered FPGA-based 8 channel digitizer is in development. Digital pulse processing algorithms are being implemented on the FPGA to allow for on-line analysis. The prototype detectors will be tested with the custom-built digitizer in the coming months. The digitizer is being designed to interface via a Bluetooth or USB serial connection with smart devices such as Android tablets and a hand-held Raspberry Pi device, to allow for mobile data capture and analysis.

Appendix A

QtDAQ software

QtDAQ is an open-source digital data acquisition (DAQ) software package, written in C++, utilising the Qt5 framework. QtDAQ is designed to handle the readout and analysis of digitised signals from several digitizers, as well as temperature monitoring and detector voltage control through communication with a microcontroller. Digitised signals can be saved to disk in unprocessed form and read back in QtDAQ for off-line analysis. Features:

- Support for a number of commercial digitizers
- Multi-threaded acquisition and analysis
- Embedded Google V8 JavaScript engine for custom analysis routines
- Compressed output using LZO or ZLib

Source code for the QtDAQ software can be found here: https://bitbucket.org/veggiesaurus/qtdaq

A compiled version for Windows 8+, linked to Qt5.7, can be found here: https://bitbucket.org/veggiesaurus/qtdaq-release

```
function getEnergyFromTimeOfFlight(neutronTimeOfFlight,
        gammaTimeOfFlight, dist)
{
    var c=0.299792458;
    var m0c2=939.565378;
    var tof=(gammaTimeOfFlight-neutronTimeOfFlight);
    if (tof<0)
        return -1;
    var beta=dist/(c*tof+dist);
    return m0c2*(1/Math.sqrt(1-beta*beta)-1);
}


chStats[1].custom2 = getEnergyFromTimeOfFlight(chStats[1].timeOfFlight,
        gammaTime, 6.00);
```

FIGURE A.1: Code snippet for calculating energy from time of flight for pulsed beam measurements (Post-event code).

```
var eventCounter=0;

setCustomParameterName(1, "DeltaCFD");
setCustomParameterName(2, "PSD(Partner)");
setCustomParameterName(3, "GeometricMean");
setCustomParameterName(4, "PSD(Geometric)");
setCustomParameterName(5, "ArithmeticMean");
```

FIGURE A.2: Code snippet for calculating total light output and pulse shape parameter from individual SiPMs for all four scintillators (Init code).

Figure A.1 shows a code snippet for calculating neutron energy from time of flight measurements for pulsed beam measurements at iThemba LABS.

Figures A.2 and A.3 show code snippets for calculating total light output parameter L and pulse shape parameter S (using the charge comparison algorithm) from individual channels for all four scintillators of the prototype detectors.

The source code repository for QtDAQ includes support for the Visual Studio 2015 IDE. In order to compile from source, a number of libraries must first be installed. Details can be found on the QtDAQ repository.

```
eventCounter++;
//shorthand notation
var L0 = chStats[0].longGateIntegral;
var L1 = chStats[1].longGateIntegral;
var L2 = chStats[2].longGateIntegral;
var L3 = chStats[3].longGateIntegral;
var L4 = chStats[4].longGateIntegral;
var L5 = chStats[5].longGateIntegral;
var L6 = chStats[6].longGateIntegral;
var L7 = chStats[7].longGateIntegral;
var S0 = chStats[0].shortGateIntegral;
var S1 = chStats[1].shortGateIntegral;
var S2 = chStats[2].shortGateIntegral;
var S3 = chStats[3].shortGateIntegral;
var S4 = chStats[4].shortGateIntegral;
var S5 = chStats[5].shortGateIntegral;
var S6 = chStats[6].shortGateIntegral;
var S7 = chStats[7].shortGateIntegral;

var trigThreshold=8;
var doCoincidenceCut=false;
//trigger cuts
if (doCoincidenceCut &&(chStats[0].baseline-chStats[0].minValue<trigThreshold ||
 chStats[7].baseline-chStats[7].minValue<trigThreshold))
{
        L0 = 0; S0 = 0; L7 = 0; S7 = 0;
}

if (doCoincidenceCut &&(chStats[5].baseline-chStats[5].minValue<trigThreshold ||
 chStats[3].baseline-chStats[3].minValue<trigThreshold))
{
        L5 = 0; S5 = 0; L3 = 0; S3 = 0;
}

if (doCoincidenceCut &&(chStats[1].baseline-chStats[1].minValue<trigThreshold ||
 chStats[6].baseline-chStats[6].minValue<trigThreshold))
{
        L1 = 0; S1 = 0; L6 = 0; S6 = 0;
}

if (doCoincidenceCut &&(chStats[2].baseline-chStats[2].minValue<trigThreshold ||
 chStats[4].baseline-chStats[4].minValue<trigThreshold))
{
        L2 = 0; S2 = 0; L4 = 0; S4 = 0;
}

//PSD and Light output (Geom)
// LT: D0 & D7 -> Ch0 and Ch7
chStats[0].custom1 = chStats[0].timeOfCFDCrossing-chStats[7].timeOfCFDCrossing;
chStats[0].custom3 = Math.sqrt(L0*L7);
chStats[0].custom4 = 100*Math.sqrt(S0*S7)/Math.sqrt(L0*L7);
chStats[0].custom5 = 0.5*(L0+L7);
chStats[0].custom2 = 100*S7/L7;
chStats[7].custom1 = -chStats[0].custom1;
chStats[7].custom3 = chStats[0].custom3;
chStats[7].custom4 = chStats[0].custom4;
chStats[7].custom5 = chStats[0].custom5;
chStats[7].custom2 = 100*S0/L0;
// RT: D5 & D8 -> Ch5 and Ch3
chStats[5].custom1 = chStats[5].timeOfCFDCrossing-chStats[3].timeOfCFDCrossing;
chStats[5].custom3 = Math.sqrt(L5*L3);
chStats[5].custom4 = 100*Math.sqrt(S5*S3)/Math.sqrt(L5*L3);
chStats[5].custom5 = 0.5*(L5+L3);
chStats[3].custom1 = -chStats[5].custom1;
chStats[3].custom3 = chStats[5].custom3;
chStats[3].custom4 = chStats[5].custom4;
chStats[3].custom5 = chStats[5].custom5;
// LB: D1 & D6 -> Ch1 and Ch6
chStats[1].custom1 = chStats[1].timeOfCFDCrossing-chStats[6].timeOfCFDCrossing;
chStats[1].custom3 = Math.sqrt(L1*L6);
chStats[1].custom4 = 100*Math.sqrt(S1*S6)/Math.sqrt(L1*L6);
chStats[1].custom5 = 0.5*(L1+L6);
chStats[6].custom1 = -chStats[1].custom1;
chStats[6].custom3 = chStats[1].custom3;
chStats[6].custom4 = chStats[1].custom4;
chStats[6].custom5 = chStats[1].custom5;
// RB: D2 & D4 -> Ch2 and Ch4
chStats[2].custom1 = chStats[2].timeOfCFDCrossing-chStats[4].timeOfCFDCrossing;
chStats[2].custom3 = Math.sqrt(L2*L4);
chStats[2].custom4 = 100*Math.sqrt(S2*S4)/Math.sqrt(L2*L4);
chStats[2].custom5 = 0.5*(L2+L4);
chStats[4].custom1 = -chStats[2].custom1;
chStats[4].custom3 = chStats[2].custom3;
chStats[4].custom4 = chStats[2].custom4;
chStats[4].custom5 = chStats[2].custom5;
```

FIGURE A.3: Code snippet for calculating total light output and pulse shape parameter from individual SiPMs for all four scintillators (Post-event code).

Bibliography

[1] M. Takada, K. Yajima, H. Yasuda, T. Sato, and T. Nakamura, "Measurement of Atmospheric Neutron and Photon Energy Spectra at Aviation Altitudes using a Phoswich-Type Neutron Detector", *J. Nucl. Sci. Technol.*, vol. 47, no. 10, pp. 932–944, 2010.

[2] C. G. Clayton, *Nuclear geophysics: Selected papers on applications of nuclear techniques in minerals exploration, mining and process control*. Elsevier, 2013.

[3] P. K. Sarkar, "Neutron dosimetry in the particle accelerator environment", in *Radiat. Meas.*, vol. 45, 2010, pp. 1476–1483.

[4] A. Buffler, "Contraband detection with fast neutrons", *Radiat. Phys. Chem.*, vol. 71, no. 3-4, pp. 853–861, 2004.

[5] C. C. Lawrence, M. Febbraro, M. Flaska, S. A. Pozzi, and F. D. Becchetti, "Warhead verification as inverse problem: Applications of neutron spectrum unfolding from organic-scintillator measurements", *J. Appl. Phys.*, vol. 120, no. 6, p. 064 501, 2016.

[6] P. K. Grieder, *Cosmic Rays at Earth*. 2001, pp. 893–974.

[7] P. Goldhagen, J. M. Clem, and J. W. Wilson, "The energy spectrum of cosmic-ray induced neutrons measured on an airplane over a wide range of altitude and latitude", *Radiat. Prot. Dosimetry*, vol. 110, no. 1-4, pp. 387–392, 2004.

[8] G. Reitz, "Radiation Environment in the Stratosphere", *Radiat. Prot. Dosimetry*, vol. 48, no. 1, pp. 5–20, 1993.

[9] M. S. Gordon, P. Goldhagen, K. P. Rodbell, T. H. Zabel, H. H. K. Tang, J. M. Clem, and P. Bailey, "Measurement of the flux and energy spectrum of cosmic-ray induced neutrons on the ground", in *IEEE Trans. Nucl. Sci.*, vol. 51, IEEE, 2004, pp. 3427–3434.

[10] J. B. Birks, "Scintillations from Organic Crystals: Specific Fluorescence and Relative Response to Different Radiations", en, *Proc. Phys. Soc. Sect. A*, vol. 64, no. 10, pp. 874–877, 1951.

[11] G. T. Wright, "Scintillation Decay Times of Organic Crystals", *Proc. Phys. Soc. Sect. B*, vol. 69, no. 3, pp. 358–372, 1956.

[12] F. Brooks, "Development of organic scintillators", *Nucl. Instruments Methods*, vol. 162, no. 1-3, pp. 477–505, 1979.

[13] N. Zaitseva, B. L. Rupert, I. PaweŁczak, A. Glenn, H. P. Martinez, L. Carman, M. Faust, N. Cherepy, and S. Payne, "Plastic scintillators with efficient neutron/gamma pulse shape discrimination", *Nucl. Instrum. Methods Phys. Res. A*, vol. 668, pp. 88–93, 2012.

[14] Eljen, *EJ-299-33 Data Sheet*, 2013.

[15] D. A. Kellogg, "Cross sections for products of 90-Mev neutrons on carbon", *Phys. Rev.*, vol. 90, no. 2, pp. 224–232, 1953.

[16] A. Comrie, A Buffler, F. Smit, and H. Wörtche, "Digital neutron/gamma discrimination with an organic scintillator at energies between 1 MeV and 100 MeV", *Nucl. Instrum. Methods Phys. Res. A*, vol. 772, pp. 43–49, 2015.

[17] ——, "Tests of pulse shape discrimination with EJ299-33 plastic scintillator for use in portable spectroscopy", *Technol. Instrum. Part. Phys.*, pp. 2–6, 2014.

[18] A Buffler, A. C. Comrie, F. D. Smit, and H. J. Wortche, "Neutron Spectrometry with EJ299-33 Plastic Scintillator for E = 10 - 100 MeV", *IEEE Trans. Nucl. Sci.*, vol. 62, no. 3, pp. 1422–1428, 2015.

[19] A Buffler, A. C. Comrie, F. D. Smit, and H. J. Wörtche, "A new compact neutron/gamma-ray scintillation detector", *International Journal of Modern Physics: Conference Series*, 2015.

[20] G. F. Knoll, *Radiation detection and measurement*. John Wiley & Sons, 2010.

[21] H. Klein and S. Neumann, "Neutron and photon spectrometry with liquid scintillation detectors in mixed fields", *Nucl. Instrum. Methods Phys. Res. A*, vol. 476, no. 1-2, pp. 132–142, 2002.

[22] J. B. Birks, *The theory and practice of scintillation counting: International series of monographs in electronics and instrumentation*. Elsevier, 2013, vol. 27.

[23] W. R. Leo, *Techniques for nuclear and particle physics experiments: A how-to approach*. Springer Science & Business Media, 2012.

[24] M. Matzke, "Unfolding procedures", *Radiat. Prot. Dosimetry*, vol. 107, no. 1-3, pp. 155–174, 2003.

[25] F. D. Brooks, R. W. Pringle, and B. L. Funt, "Pulse Shape Discrimination in a Plastic Scintillator", *IRE Trans. Nucl. Sci.*, vol. 7, no. 2-3, pp. 35–38, 1960.

[26] C. Brient, C. Nelson, and R. Young, "Pulse shape analyzer for fast neutron-gamma ray discrimination", *Nucl. Instruments Methods*, vol. 98, no. 2, pp. 329–333, 1972.

[27] I. R. E. Transactions and O. N. Nuclear, "The Decay Times of Organic Scintillators and Their Application to the Discrimination Between Particles of Differing Specific Ionization *", *IRE Trans. Nucl. Sci.*, vol. 124, no. 3, pp. 122–123, 1958.

[28] G. H. V. Bertrand, M. Hamel, S. Normand, and F. Sguerra, "Pulse shape discrimination between (fast or thermal) neutrons and gamma rays with plastic scintillators: State of the art", *Nucl. Instrum. Methods Phys. Res. A*, vol. 776, pp. 114–128, 2015.

[29] R. A. Winyard, J. E. Lutkin, and G. W. McBeth, "Pulse shape discrimination in inorganic and organic scintillators", *Nucl. Instruments Methods*, vol. 95, no. 1, pp. 141–153, 1971.

[30] N. Zaitseva, A. Glenn, L. Carman, R. Hatarik, S. Hamel, M. Faust, B. Schabes, N. Cherepy, and S. Payne, "Pulse shape discrimination in impure and mixed single-crystal organic scintillators", *IEEE Trans. Nucl. Sci.*, vol. 58, no. 6 PART 2, pp. 3411–3420, 2011.

[31] P. N. Zhmurin, V. N. Lebedev, V. D. Titskaya, A. F. Adadurov, D. A. Elyseev, and V. N. Pereymak, "Polystyrene-based scintillator with pulse-shape discrimination capability", *Nucl. Instrum. Methods Phys. Res. A*, vol. 761, pp. 92–98, 2014.

[32] S. Nyibule, E. Henry, W. Schröder, J. Tõke, L. Acosta, L. Auditore, G. Cardella, E. De Filippo, L. Francalanza, S. Gìani, T. Minniti, E. Morgana, E. Pagano, S. Pirrone, G. Politi, L. Quattrocchi, F. Rizzo, P. Russotto, a. Trifirò, and M. Trimarchi, "Radioluminescent characteristics of the EJ 299-33 plastic scintillator", *Nucl. Instrum. Methods Phys. Res. A*, vol. 728, pp. 36–39, 2013.

[33] P. Blanc, M. Hamel, C. Dehé-Pittance, L. Rocha, R. B. Pansu, and S. Normand, "Neutron/gamma pulse shape discrimination in plastic scintillators: Preparation and characterization of various compositions", *Nucl. Instrum. Methods Phys. Res. A*, vol. 750, pp. 1–11, 2014.

[34] S. Pozzi, M. Bourne, and S. Clarke, "Pulse shape discrimination in the plastic scintillator EJ-299-33", *Nucl. Instrum. Methods Phys. Res. A*, vol. 723, pp. 19–23, 2013.

[35] D. Cester, G. Nebbia, L. Stevanato, F. Pino, and G. Viesti, "Experimental tests of the new plastic scintillator with pulse shape discrimination capabilities EJ-299-33", *Nucl. Instrum. Methods Phys. Res. A*, vol. 735, pp. 202–206, 2014.

[36] J Iwanowska-Hanke, M Moszynski, L Swiderski, P Sibczynski, T Szczesniak, T Krakowski, and P Schotanus, "Comparative study of large samples plastic scintillators and EJ309 liquid with pulse shape discrimination (PSD) capabilities", *J. Instrum.*, vol. 9, no. 06, P06014–P06014, 2014.

[37] Eljen, *EJ-299-33A Data Sheet*, 2015.

[38] J. Hartman, A. Barzilov, E. Peters, and S. Yates, "Measurements of response functions of EJ-299-33A plastic scintillator for fast neutrons", *Nucl. Instrum. Methods Phys. Res. A*, pp. 1–7, 2015.

[39] C. C. Lawrence, M. Febbraro, T. N. Massey, M. Flaska, F. Becchetti, and S. a. Pozzi, "Neutron response characterization for an EJ299-33 plastic scintillation detector", *Nucl. Instrum. Methods Phys. Res. A*, vol. 759, pp. 16–22, 2014.

[40] S Nyibule, J Tõke, E Henry, W. Schröder, L Acosta, L Auditore, G Cardella, E De Filippo, L Francalanza, and S Gianì, "Birks' scaling of the particle light output functions for the EJ 299-33 plastic scintillator", *Nucl. Instrum. Methods Phys. Res. A*, vol. 768, pp. 141–145, 2014.

[41] R. S. Woolf, A. L. Hutcheson, C. Gwon, B. F. Phlips, and E. A. Wulf, "Comparing the response of PSD-capable plastic scintillator to standard liquid scintillator", *Nucl. Instrum. Methods Phys. Res. A*, vol. 784, pp. 80–87, 2015.

[42] D. Cester, M. Lunardon, G. Nebbia, L. Stevanato, G. Viesti, S. Petrucci, and C. Tintori, "Pulse shape discrimination with fast digitizers", *Nucl. Instrum. Methods Phys. Res. A*, vol. 748, pp. 33–38, 2014.

[43] N. P. Hawkes and G. C. Taylor, "Analysis of the pulse shape mechanism in a plastic scintillator with efficient neutron/gamma pulse shape discrimination", *Nucl. Instrum. Methods Phys. Res. A*, vol. 729, pp. 522–526, 2013.

[44] T. Szczesniak, M. Moszynski, A. Syntfeld-Kazuch, Swiderski, D. Wolski, M. Grodzicka, G. Pausch, J. R. Stein, F. Kniest, M. R. Kusner, P. Schotanus, and C. Hurlbut, "Light pulse shapes in liquid scintillators originating from gamma-rays and neutrons", *IEEE Trans. Nucl. Sci.*, vol. 57, no. 6 PART 2, pp. 3846–3852, 2010.

[45] N. V. Kornilov, V. A. Khriatchkov, M. Dunaev, A. B. Kagalenko, N. N. Semenova, V. G. Demenkov, and A. J. M. Plompen, "Neutron spectroscopy with fast waveform digitizer", *Nucl. Instrum. Methods Phys. Res. A*, vol. 497, no. 2-3, pp. 467–478, 2003.

[46] B. Esposito, L. Fortuna, and A. Rizzo, "Neural neutron/gamma discrimination in organic scintillators for fusion applications", in *IEEE Int. Conf. Neural Networks - Conf. Proc.*, vol. 4, 2004, pp. 2931–2936.

[47] V. Jordanov and G. Knoll, "Digital pulse-shape analyzer based on fast sampling of an integrated charge pulse", *Proc. 1994 IEEE Nucl. Sci. Symp. - NSS'94*, vol. 1, no. 4, pp. 683–687, 1994.

[48] Y. Kaschuck and B. Esposito, "Neutron/gamma-ray digital pulse shape discrimination with organic scintillators", *Nucl. Instrum. Methods Phys. Res. A*, vol. 551, no. 2-3, pp. 420–428, 2005.

[49] M. Nakhostin and P. M. Walker, "Application of digital zero-crossing technique for neutron-gamma discrimination in liquid organic scintillation detectors", *Nucl. Instrum. Methods Phys. Res. A*, vol. 621, no. 1-3, pp. 498–501, 2010.

[50] P. A. Söderström, J. Nyberg, and R. Wolters, "Digital pulse-shape discrimination of fast neutrons and gamma-rays", *Nucl. Instrum. Methods Phys. Res. A*, vol. 594, no. 1, pp. 79–89, 2008.

[51] D. I. Shippen, M. J. Joyce, and M. D. Aspinall, "A wavelet packet transform inspired method of neutron-gamma discrimination", *IEEE Trans. Nucl. Sci.*, vol. 57, no. 5 PART 2, pp. 2617–2624, 2010.

[52] B. D'Mellow, M. Aspinall, R. Mackin, M. Joyce, and a.J. Peyton, "Digital discrimination of neutrons and gamma-rays in liquid scintillators using pulse gradient analysis", *Nucl. Instrum. Methods Phys. Res. A*, vol. 578, no. 1, pp. 191–197, 2007.

[53] G. Liu, M. J. Joyce, X. Ma, and M. D. Aspinall, "A digital method for the discrimination of neutrons and gamma-rays with organic scintillation detectors using frequency gradient analysis", *IEEE Trans. Nucl. Sci.*, vol. 57, no. 3 PART 3, pp. 1682–1691, 2010.

[54] R. Preston, J. E. Eberhardt, R. Bencardino, and J. Tickner, "Software-Based Digital Pulse Processing for Silicon Photomultiplier Radiation Detectors", *IEEE Nucl. Sci. Symp. Med. Imaging Conf. Rec.*, no. 11, pp. 462–467, 2012.

[55] E Gatti and F. D. Martini, "A new linear method of discrimination between elementary particles in scintillation counters", in *Nuclear Electronics II. Proceedings of the Conference on Nuclear Electronics. V. II*, 1962.

[56] N. P. Hawkes, K. A. A. Gamage, and G. C. Taylor, "Digital approaches to field neutron spectrometry", *Radiat. Meas.*, vol. 45, no. 10, pp. 1305–1308, 2010.

[57] K. Gamage, M. Joyce, and N. Hawkes, "A comparison of four different digital algorithms for pulse-shape discrimination in fast scintillators", *Nucl. Instrum. Methods Phys. Res. A*, vol. 642, no. 1, pp. 78–83, 2011.

[58] P. Buzhan, B. Dolgoshein, L. Filatov, A. Ilyin, V. Kantzerov, V. Kaplin, A. Karakash, F. Kayumov, S. Klemin, E. Popova, and S. Smirnov, "Silicon photomultiplier and its possible applications", *Nucl. Instrum. Methods Phys. Res. A*, vol. 504, no. 1-3, pp. 48–52, 2003.

[59] SensL, "An Introduction to the Silicon Photomultiplier", Tech. Rep., 2011, pp. 1–8.

[60] K. Yamamoto, K. Yamamura, K. Sato, T. Ota, H. Suzuki, and S. Ohsuka, "Development of Multi-Pixel Photon Counter (MPPC)", *2006 IEEE Nucl. Sci. Symp. Conf. Rec.*, vol. 2, pp. 1094–1097, 2006.

[61] SensL, *C-Series Silicon Photomultipliers Datasheet*, 2014.

[62] C. Piemonte, "A new Silicon Photomultiplier structure for blue light detection", *Nucl. Instrum. Methods Phys. Res. A*, vol. 568, no. 1, pp. 224–232, 2006.

[63] SensL, *B-Series Silicon Photomultipliers Datasheet*, 2013.

[64] A. L. Lacaita, F. Zappa, S. Bigliardi, and M. Manfredi, "On the bremsstrahlung origin of hot-carrier-induced photons in silicon devices", *IEEE Transactions on electron devices*, vol. 40, no. 3, pp. 577–582, 1993.

[65] D. Renker, "Geiger-mode avalanche photodiodes, history, properties and problems", *Nucl. Instrum. Methods Phys. Res. A*, vol. 567, pp. 48–56, 2006.

[66] M. Danilov, "Scintillator tile hadron calorimeter with novel SiPM readout", *Nucl. Instrum. Methods Phys. Res. A*, vol. 581, no. 1-2 SPEC. ISS. Pp. 451–456, 2007. arXiv: 0704.3514.

[67] M. L. Ruch, C. B. Sivels, S. A. Czyz, M. Flaska, and S. A. Pozzi, "Comparison between silicon photomultipliers and photomultiplier tubes for pulse shape discrimination with stilbene", in *2014 IEEE Nucl. Sci. Symp. Med. Imaging Conf.*, IEEE, 2014, pp. 1–3.

[68] M. L. Ruch, M. Flaska, and S. a. Pozzi, "Pulse shape discrimination performance of stilbene coupled to low-noise silicon photomultipliers", *Nucl. Instrum. Methods Phys. Res. A*, vol. 793, pp. 1–5, 2015.

[69] R. M. Preston, J. E. Eberhardt, and J. R. Tickner, "Neutron generator burst timing measured using a pulse shape discrimination plastic scintillator with silicon photomultiplier readout", *J. Instrum.*, vol. 8, no. 12, P12005–P12005, 2013.

[70] R. M. Preston, J. E. Eberhardt, and J. R. Tickner, "Neutron-Gamma Pulse Shape Discrimination Using Organic Scintillators With Silicon Photomultiplier Readout", *IEEE Trans. Nucl. Sci.*, vol. 61, no. 4, pp. 2410–2418, 2014.

[71] C. Liao and H. Yang, "Pulse shape discrimination using EJ-299-33 plastic scintillator coupled with a Silicon Photomultiplier array", *Nucl. Instrum. Methods Phys. Res. A*, pp. 1–8, 2015.

[72] K. E. Mesick, L. C. Stonehill, J. T. Morrell, and D. D. S. Coupland, "Performance of Several Solid State Photomultipliers with CLYC Scintillator", in *2015 IEEE Nucl. Sci. Symp.*, 2015, N3B2–3. arXiv: 1512.01155.

[73] A. C. Comrie. (2015). QtDAQ git repository, [Online]. Available: https://bitbucket.org/veggiesaurus/qtdaq.

[74] Qt Foundation. (2015). Qt 5.5 Open source, [Online]. Available: http://www.qt.io.

[75] CAEN. (2015). CAENDigitizer library, [Online]. Available: http://caen.it/jsp/Template2/CaenProd.jsp?parent=38{\&}idmod=717.

[76] S. Ritt, "Design and performance of the 6 GHz waveform digitizing chip DRS4", in *2008 IEEE Nucl. Sci. Symp. Conf. Rec.*, 2008, pp. 1512–1515.

[77] N. W. Group, P Deutsch, A. Enterprises, and J.-l. Gailly, "ZLIB Compressed Data Format Specifation version 3.3", *Distribution*, pp. 1–10, 1996.

[78] M. Adler and J.-l. Gailly. (2014). Zlib Compression Library, [Online]. Available: http://www.zlib.net/.

[79] M Oberhumer. (2015). LZO real-time data compression library, [Online]. Available: http://www.oberhumer.com/opensource/lzo.

[80] Google. (2015). V8 JavaScript engine, [Online]. Available: https://developers.google.com/v8.

[81] Texas Instruments. (2015). LM35 precision centigrade temperature sensors, [Online]. Available: http://www.ti.com/lit/ds/symlink/lm35.pdf.

[82] CAEN, "VX1761 User manual", Tech. Rep., 2012.

[83] ——, "DT5730 User manual", Tech. Rep., 2014.

[84] F. D. Brooks, A. Buffler, M. S. Allie, M. S. Herbert, M. R. Nchodu, D. T. L. Jones, F. D. Smit, R. Nolte, and V. Dangendorf, "A compact high-energy neutron spectrometer", *Radiat. Prot. Dosimetry*, vol. 126, no. 1-4, pp. 218–222, 2007. arXiv: 0703211 [physics].

[85] F. D. Brooks, M. S. Allie, a. Buffler, V. Dangendorf, M. S. Herbert, S. a. Makupula, R. Nolte, and F. D. Smit, "Measurement of neutron fluence spectra up to 150 MeV using a stacked scintillator neutron spectrometer", *Radiat. Prot. Dosimetry*, vol. 110, pp. 151–155, 2004.

[86] M. Mosconi, E. Musonza, A. Buffler, R. Nolte, S. Röttger, and F. Smit, "Characterisation of the high-energy neutron beam at iThemba LABS", *Radiat. Meas.*, vol. 45, no. 10, pp. 1342–1345, 2010.

[87] H. Peng, P. D. Olcott, A. M. K. Foudray, and C. S. Levin, "Evaluation of free-running ADCs for high resolution PET data acquisition", in *2007 IEEE Nucl. Sci. Symp. Conf. Rec.*, vol. 5, IEEE, 2007, pp. 3328–3331.

[88] A. Enqvist, C. C. Lawrence, B. M. Wieger, S. A. Pozzi, and T. N. Massey, "Neutron light output response and resolution functions in EJ-309 liquid scintillation detectors", *Nucl. Instrum. Methods Phys. Res. A*, vol. 715, pp. 79–86, 2013.

[89] G Dietze, "Energy calibration of NE-213 scintillation counters by gamma-rays", *IEEE Trans. Nucl. Sci.*, vol. 26, no. 1, pp. 398–402, 1979.

[90] G. Dietze and H. Klein, "Gamma-calibration of NE 213 scintillation counters", *Nucl. Instrum. Methods Phys. Res.*, vol. 193, no. 3, pp. 549–556, 1982.

[91] N. Kudomi, "Energy calibration of plastic scintillators for low energy electrons by using Compton scatterings of gamma rays", *Nucl. Instrum. Methods Phys. Res. A*, vol. 430, no. 1, pp. 96–99, 1999.

[92] D. Smith, R. Polk, and T. Miller, "Measurement of the response of several organic scintillators to electrons, protons and deuterons", *Nucl. Instruments Methods*, vol. 64, no. 2, pp. 157–166, 1968.

[93] R. Craun and D. Smith, "Analysis of response data for several organic scintillators", *Nucl. Instruments Methods*, vol. 80, no. 2, pp. 239–244, 1970.

[94] K. Flynn, L. Glendenin, E. Steinberg, and P. Wright, "Pulse height-energy relations for electrons and alpha particles in a liquid scintillator", *Nucl. Instruments Methods*, vol. 27, no. 1, pp. 13–17, 1964.

[95] J. Strain and G. Leddicotte, "the Preparation, Properties, and Uses of Americium-241, Alpha-, Gamma-, and Neutron Sources", Oak Ridge National Laboratory (ORNL), Oak Ridge, TN (United States), Tech. Rep., 1962.

[96] J. Bohm, W. Alberts, K. Swinth, C. Soares, J. McDonald, I. Thompson, and H. Kramer, "ISO Recommended Reference Radiations for the Calibration and Proficiency Testing of Dosemeters and Dose Rate Meters used in Radiation Protection", *Radiat. Prot. Dosimetry*, vol. 86, no. 2, pp. 87–105, 1999.

[97] A. Buffler and J. Tickner, "Detecting contraband using neutrons: Challenges and future directions", *Radiat. Meas.*, vol. 45, no. 10, pp. 1186–1192, 2010.

[98] G Vourvopoulos, "Pulsed fast/thermal neutron analysis: a technique for explosives detection", *Talanta*, vol. 54, no. 3, pp. 459–468, 2001.

[99] V. Bom, M. Ali, and C. van Eijk, "Land mine detection with neutron back scattering imaging using a neutron generator", *IEEE Trans. Nucl. Sci.*, vol. 53, no. 1, pp. 356–360, 2006.

[100] J. E. Eberhardt, S Rainey, R. J. Stevens, B. D. Sowerby, and J. R. Tickner, "Fast neutron radiography scanner for the detection of contraband in air cargo containers.", *Appl. Radiat. Isot.*, vol. 63, no. 2, pp. 179–88, 2005.

[101] Y. Bogolubov, S. Korotkov, L. Korytko, V. Morukov, V. Nazarov, Y. Polkanov, and T. Khasaev, "Method and system based on pulsed neutron generator for fissile material detection in luggage", *Nucl. Instrum. Methods Phys. Res. B*, vol. 213, pp. 439–444, 2004.

[102] E. D. Williams, K Boddy, I Harvey, and J. K. Haywood, "Calibration and evaluation of a system for total body in vivo activation analysis using 14 MeV neutrons", en, *Phys. Med. Biol.*, vol. 23, no. 3, pp. 405–415, 1978.

[103] S. Cohn, C. Dombrowski, and R. Fairchild, "In-Vivo neutron activation analysis of calcium in man", *Int. J. Appl. Radiat. Isot.*, vol. 21, no. 3, pp. 127–134, 1970.

[104] Thermo Fisher Scientific, "Thermo Scientific MP 320", Tech. Rep., 2007.

[105] R. Nolte, M. S. Allie, R. Bottger, F. D. Brooks, a. Buffler, V. Dangendorf, H. Friedrich, S. Guldbakke, H. Klein, J. P. Meulders, D. Schlegel, H. Schuhmacher, and F. D. Smit, "Quasi-monoenergetic neutron reference fields in the energy range from thermal to 200 MeV", *Radiat. Prot. Dosimetry*, vol. 110, no. 1-4, pp. 97–102, 2004.

[106] H. Harano and R. Nolte, "Quasi-monoenergetic high-energy neutron standards above 20 MeV", en, *Metrologia*, vol. 48, no. 6, S292–S303, 2011.

[107] M. J. Berger, J. Coursey, M. Zucker, and J Chang, *Stopping-power and range tables for electrons, protons, and helium ions*. NIST Physics Laboratory, 1998.

[108] Y. Uwamino, K. Shin, M. Fujii, and T. Nakamura, "Light output and response function of an NE-213 scintillator to neutrons up to 100 MeV", *Nucl. Instruments Methods Phys. Res.*, vol. 204, no. 1, pp. 179–189, 1982.

[109] N. Nakao, T. Kurosawa, T. Nakamura, and Y. Uwamino, "Absolute measurements of the response function of an NE213 organic liquid scintillator for the neutron energy range up to 206 MeV", *Nucl. Instrum. Methods Phys. Res. A*, vol. 463, no. 1-2, pp. 275–287, 2001.

[110] M Matzke and K Weise, "Neutron spectrum unfolding by the Monte Carlo method", *Nucl. Instrum. Methods Phys. Res.*, vol. 234, pp. 324–330, 1985.

[111] M Matzke, *Unfolding of pulse height spectra: the HEPRO program system*, Array, 1994.

[112] M. Matzke, "Propagation of uncertainties in unfolding procedures", *Nucl. Instrum. Methods Phys. Res. A*, vol. 476, no. 1-2, pp. 230–241, 2002.

[113] J. Dickens, "SCINFUL: A Monte Carlo based computer program to determine a scintillator full energy response to neutron detection for E between 0. 1 and 80 MeV: Program development and comparisons of program predictions with experimental data", English, Oak Ridge National Laboratory (ORNL), Oak Ridge, TN (United States), Tech. Rep., 1988.

[114] S. Agostinelli, J. Allison, K. Amako, J. Apostolakis, H. Araujo, P. Arce, and M. Asai, "Geant4—a simulation toolkit", *Nucl. Instrum. Methods Phys. Res. A*, vol. 506, no. 3, pp. 250–303, 2003.

[115] N. Patronis, M. Kokkoris, D. Giantsoudi, G. Perdikakis, C. Papadopoulos, and R. Vlastou, "Aspects of GEANT4 Monte-Carlo calculations of the BC501A neutron detector", *Nucl. Instrum. Methods Phys. Res. A*, vol. 578, no. 1, pp. 351–355, 2007.

[116] K. Banerjee, T. Ghosh, S. Kundu, T. Rana, C. Bhattacharya, J. Meena, G. Mukherjee, P. Mali, D. Gupta, S. Mukhopadhyay, D. Pandit, S. Banerjee, S. Bhattacharya, T. Bandyopadhyay, and S. Chatterjee, "Variation of neutron detection characteristics with dimension of BC501A neutron detector", *Nucl. Instrum. Methods Phys. Res. A*, vol. 608, no. 3, pp. 440–446, 2009.

[117] S. Naeem, S. Clarke, and S. Pozzi, "Validation of Geant4 and MCNPX-PoliMi simulations of fast neutron detection with the EJ-309 liquid scintillator", *Nucl. Instrum. Methods Phys. Res. A*, vol. 714, pp. 98–104, 2013.

[118] M. Tajik, N. Ghal-Eh, G. Etaati, and H. Afarideh, "Modeling NE213 scintillator response to neutrons using an MCNPX-PHOTRACK hybrid code", *Nucl. Instrum. Methods Phys. Res. A*, vol. 704, pp. 104–110, 2013.

[119] Z. S. Hartwig and P. Gumplinger, "Simulating response functions and pulse shape discrimination for organic scintillation detectors with Geant4", *Nucl. Instrum. Methods Phys. Res. A*, vol. 737, pp. 155–162, 2014.

[120] Geant4 Collaboration. (2015). Geant4 source code, [Online]. Available: http://geant4.cern.ch/support/source/geant4/source/processes/electromagnetic/xrays/src/G4Scintillation.cc.

[121] Hartwig Z. S. and Gumplinger P., "Simulating the optical physics of nonlinear scintillation detectors with Geant4", *Nucl. Instrum. Methods Phys. Res. A*, vol. ??, pp. 1–12, 2013.

[122] R. Bencardino, J. E. Eberhardt, and R. Preston, "Anti-coincidence rejection of SiPM dark pulses for improved detection of low energy radiation", in *Nucl. Instrum. Methods Phys. Res. A*, vol. 619, 2010, pp. 497–500.

[123] SensL, "B-Series Silicon Photomultipliers User manual", pp. 1–15, 2013.

[124] Blender Online Community, *Blender - a 3d modelling and rendering package*, Blender Foundation, Blender Institute, Amsterdam, 2016.

[125] Minicircuits. (2015). ZFL-1000NL low noise amplifier, [Online]. Available: http://www.minicircuits.com/pdfs/ZFL-1000LN+.pdf.

[126] R. Pagano, S. Lombardo, S. Libertino, G. Valvo, G. Condorelli, B. Carbone, D. N. Sanfilippo, and G. Fallica, "Understanding dark current in pixels of silicon Photomultipliers", in *2010 Proc. Eur. Solid State Device Res. Conf. ESSDERC 2010*, 2010, pp. 265–268.

[127] M. Grodzicka, M. Moszynski, T. Szczesniak, M. Szawlowski, D. Wolski, and K. Lesniewski, "Effective dead time of APD cells of SiPM", *2011 IEEE Nucl. Sci. Symp. Conf. Rec.*, no. October 2015, pp. 553–562, 2011.

[128] Geant4 Collaboration, "Geant4 User's Guide for Application Developers", ... *GEANT4 web page [1] Version geant4*, 2012.